A Broadband Noise Prediction Framework for Propellers

Jelmer Repke Peter Ottens

TU Delft

A Broadband Noise Prediction Framework for Propellers

by

Jelmer Repke Peter Ottens

to obtain the degree of Master of Science
at the Delft University of Technology,
to be defended publicly on 9 March 2026

Student Number :	5307600
Project Duration:	01-05-2025 - 09-03-2026
Faculty:	Faculty of Aerospace Engineering, Delft University of Technology

Thesis Committee

Chair:	Dr. Ir. R. Vos
Supervisors:	Prof. Dr. Ir. M. Snellen
	Dr. Ir. F. Yunus
External examiner:	Ir. S. Nolet (NLR - Royal Netherlands Aerospace Centre)
	Dr. Ir. S.J. Heblij (NLR - Royal Netherlands Aerospace Centre)

An electronic version of this thesis is available at `http://repository.tudelft.nl/`.

Cover Page: background generated by ChatGPT, 21 January 2026, OpenAI, https://chat.openai.com.

Preface

This thesis completes my Master's degree in Aerospace Engineering at Delft University of Technology. It is the last step in a journey that has been both rewarding and challenging.

I want to thank my academic supervisors, Furkat Yunus and Mirjam Snellen. Their guidance, advice, and enthusiasm shaped this project and helped me develop as a researcher. Also, I am grateful to my supervisors at the Royal Netherlands Aerospace Centre (NLR), Stijn Nolet and Sander Heblij, for their support and insight. Furthermore, I want to thank the whole AOSE department at NLR for welcoming me and creating an environment where I could learn and enjoy my work.

I am especially grateful to my mother, father, sister, and girlfriend for always encouraging me and believing in me during my thesis and throughout the past five and a half years of my studies. My family and friends have always supported me and kept me motivated.

I truly could not have completed this thesis without the incredible support of everyone mentioned above, and I am very grateful to each of them. I look forward to carrying what I have learned at Delft University of Technology into the next chapter of my life.

Jelmer Repke Peter Ottens
Delft, February 2026

Abstract

Recently, rising interest in Urban Air Mobility (UAM) and the need for more sustainable, quieter propulsion systems have led to a stronger focus on electric propulsion. In electrically powered aircraft and emerging UAM concepts, where combustion and exhaust noise are absent, propeller-generated aerodynamic noise becomes the primary contributor to the overall acoustic footprint. Propeller noise consists of a tonal component (which is related to periodic steady and unsteady blade loading) and a broadband component (which can be related to turbulent inflow and turbulent flow developed on the blade surface). This thesis develops a broadband noise prediction framework used to assess and compare different broadband noise models in terms of their accuracy, physical consistency, and applicability across varying operating conditions. The framework is validated using experimental data from scaled hover tests and full-scale flyover measurements.

Classical broadband noise prediction models, such as the Brooks, Pope, and Marcolini (BPM) model [1], often require boundary layer parameters as input. More recent models, on the other hand, such as the Gill and Lee (GL) model [2], predict broadband noise from rotor performance parameters using a data-driven formulation. This development represents a significant simplification in required input and computational effort for broadband noise prediction of propellers. However, a systematic comparison of its accuracy against classical models across diverse flight conditions (in particular in forward flight) has not been established in the literature. The broadband noise prediction framework developed in this thesis enables the comparison between the classical BPM model and the data-driven Gill and Lee model. Both broadband noise models were verified against literature reference results. For identical input conditions, the implemented models reproduce published spectra with good accuracy. This confirmed their correct numerical implementation. A blade element momentum theory (BEMT) solver was integrated into the framework to provide the required aerodynamic input for the models. Furthermore, the required boundary layer parameters for the BPM model can be obtained from (already in the model incorporated) empirical formulas or by extracting them from XFOIL. Finally, atmospheric absorption and Doppler effects were included to improve the model prediction accuracy.

Validation of the framework shows that both broadband noise models exhibit satisfactory agreement with experimental measurements of a scaled propeller under hover conditions. In hover, the Gill and Lee model demonstrates favourable agreement with measured noise spectra. Differences in the use of empirical and XFOIL boundary layer parameters in the BPM model were shown to affect predicted noise levels and spectral peak locations.

Validation and application of the broadband noise framework to flyover and take-off measurements of a fully electric single-propeller aircraft reveal clear differences between the models. The BPM model consistently shows reasonable agreement with measured spectrograms across level flight and take-off cases. Only a slight underestimation of broadband noise levels is observed. In contrast, the Gill and Lee model significantly overpredicts broadband noise. It exhibits physically inconsistent directivity and distance scaling behaviour, including an almost complete absence of sound pressure level decay with increasing observer distance. Moreover, the predicted spectrogram shape remains nearly identical across different flight conditions (hover, level flight, and take-off).

This study concludes that the Gill and Lee model, while offering advantages in terms of required input and its formulation based on rotor performance, is currently limited to hover conditions. The observed discrepancies of the Gill and Lee model in forward flight can be attributed to several factors. Namely, the model was primarily developed using hover experiments, with only one validation in forward flight. This experimental validation presented by Gill and Lee for forward flight also corresponds to a significantly smaller propeller than the one investigated in this thesis. Although further research is required, this suggests that propeller size or tip speed effects may play an important role in the applicability of the Gill and Lee model. The BPM model provides more reliable broadband noise predictions in forward flight. However, the strong performance of the Gill and Lee model in hover

emphasises the promise of data-driven and performance-based approaches for urban air mobility applications.

Recommendations for future work include integrating the broadband noise framework with tonal noise models. Alternatively, the broadband and tonal components could be separated in experimental data. This would allow for a better assessment of either the total acoustic signature or only its broadband component. Also, the broadband noise models should be compared from a perceptual perspective. This helps interpret the observed differences, such as the difference between improved sound pressure level magnitude with BPM and XFOIL boundary layer parameters and improved spectral peak prediction with empirically obtained boundary layer parameters. Further investigation is required to identify the operational limits of the Gill and Lee model. This includes investigating potential dependencies on propeller size and tip speed. Finally, a new data-driven broadband noise model that explicitly incorporates flight condition parameters is proposed to support reliable noise prediction for electric propeller-driven aircraft across all operational conditions.

Contents

List of Figures

List of Tables

Nomenclature

Abbreviations

Abbreviation	Definition
ANOPP	Aircraft Noise Prediction Program
ASNIFM	ANOPP2 Self-Noise Internal Functional Module
BARC	Broadband Acoustic Rotor Codes
BEMT	Blade Element Momentum Theory
BET	Blade Element Theory
BL	Boundary Layer
BPF	Blade Passage Frequency
BPM	Brooks, Pope, and Marcolini
BWI	Blade-Wake Interaction
CFD	Computational Fluid Dynamics
CS	Coordinate System
dBA	A-weighted Decibels
DES	Detached Eddy Simulations
DI	Directivity Index
DFT	Discrete Fourier Transform
DNN	Deep Neural Network
DNS	Direct Nummerical Simulation
DNW	Duits-Nederlandse Windtunnel
DSP	Digital Signal Processing
EAL	Equivalent A-weighted Sound Level
eVTOL	Electric Vertical Take-Off and Landing
FT	Fourier Transform
FO	Flyover
FRPM	Fast Random Particle Mesh
FW-H	Ffowcs Williams–Hawkings
GEP	Gene Expression Programming
GL	Gill and Lee
IDFT	Inverse Discrete Fourier Transform
IFT	Inverse Fourier Transform
ILES	Implicit LES
LBL-VS	Laminar Boundary Layer - Vortex Shedding
LBM	Lattice Boltzmann Method
LES	Large Eddy Simulations
ML	Machine Learning
NLR	Nederlands Lucht- en Ruimtevaart Centrum
OASPL	Overall A-weighted Sound Pressure Level
PSD	Power Spectral Density
PWL	Power Watt Level
RANS	Reynolds-Averaged Navier-Stokes
RMS	Root-Mean-Square
RPM	Rounds Per Minute
RPS	Rounds Per Second
SEL	Sound Exposure Level
SGS	Sub-Grid Scale
SPL	Sound Pressure Level

Abbreviation	Definition
S-TES	Separation - Trailing Edge Stall
TBL-TE	Turbulent Boundary Layer - Trailing Edge
TEB-VS	Trailing Edge Bluntness - Vortex Shedding
TELE-Noise	Trailing Edge and Leading Edge - Noise
TI-LE	Turbulent Inflow - Leading Edge
TNO	The Netherlands Organisation for Applied Scientific Research
TO	Take-Off
TVF	Tip Vortex Formation
UAM	Urban Air Mobility
UCD-QuietFly	University of California Davis QuietFly
URANS	Unsteady RANS
VLES	Very-Large Eddy Simulations
WPS	Wall-Pressure Spectrum

Symbols

Symbol	Definition	Unit
A	Amplitude or BPM spectral shape function	[m] or [-]
A'	Modified spectral shape function in stall	[-]
a	Axial induction factor	[-]
a'	Tangential induction factor	[-]
$A_{\min}, A_{\max}$	Lower/upper envelopes for BPM shape function A	[-]
A_R	Spectral interpolation coefficient (BPM)	[-]
a_0	Reynolds-dependent reference spectral parameter	[-]
B	BPM shape function for separation noise	[-]
$B_{\min}, B_{\max}$	Lower/upper envelopes for BPM shape function B	[-]
B_R	Spectral interpolation coefficient (BPM)	[-]
b	Auxiliary spectral variable (separation noise)	[-]
b_0	Reference spectral parameter for separation	[-]
b_c	Normalised blade local chord length	[-]
c	Chord length or speed of sound	[m] or [m/s]
c_1	Distance from leading edge to pitch axis	[m]
c_2	Trailing edge offset ($c - c_1$)	[m]
C_P	Power coefficient	[-]
C_Q	Torque coefficient	[-]
C_T	Thrust coefficient	[-]
D	Propeller diameter	[m]
D'	Elemental drag force	[N/m]
$\bar{D}_h$	High-frequency directivity function	[-]
$\bar{D}_\ell$	Low-frequency directivity function	[-]
ΔK_1	Correction to spectral amplitude K_1	[-]
f	Frequency	[Hz]
f_L, f_U	Lower/upper frequency	[Hz]
f_N	Centre frequency	[Hz]
$f_0 \ldots f_8$	Fitted GEP coefficients (GL)	[-]
H	Trailing edge bluntness	[mm]
h	Altitude	[m]
h_m	Microphone height	[m]
J	Advance ratio	[-]
K_1, K_2	BPM amplitude functions	[-]
L'	Elemental lift force	[N/m]
L	Span/element length	[m]
L_A	Overall A-weighted SPL	[dBA]

Symbol	Definition	Unit
L_{AE}	Sound exposure level	[dBA]
$L_{Aeq,T}$	Equivalent A-weighted SPL over time T	[dBA]
$L_{A,max}$	Maximum A-weighted SPL	[dBA]
L_{DEN}	Day–evening–night level	[dBA]
M	Mach number	[-]
M_t	Tip Mach number	[-]
n	Rotational speed	[rev/s]
N	Number of samples	[-]
N_B	Number of blades	[-]
P	Power	[W]
p'	Acoustic pressure fluctuation	[Pa]
p_e	Effective sound pressure	[Pa]
p_{e0}	Reference sound pressure	[Pa]
Q	Torque	[Nm]
r	Radial position or distance	[m]
r_{obs}	Observer distance (BPM)	[m]
R	Propeller radius or gas constant	[m] or [J/kg K]
Re_c	Chord Reynolds number	[-]
Re_{δ^*}	Displacement thickness Reynolds number	[-]
S_ω	Normalized spectral shape function	[-]
s_0	Observer distance (GL)	[m]
S_{pp}	Far-field sound frequency spectrum	[-]
S_t	Strouhal number (GL)	[-]
V	Local velocity	[m/s]
V_{ax}	Axial velocity	[m/s]
V_{rot}	Rotational velocity	[m/s]
V_{eff}	Effective velocity	[m/s]
V_t	Tip velocity	[m/s]
W, W_0	Acoustic power and reference value	[W]
x	x-coordinate	[m]
y	y-coordinate	[m]
z	z-coordinate	[m]
α	Angle of attack or absorption coefficient	[°] or [dB/m]
α_*	Angle of attack (BPM)	[°]
α_{tip}	Tip angle of attack (BPM)	[°]
α_{disk}	Propeller disk angle	[°]
β	Blade pitch angle	[°]
γ	Specific heat ratio or BPM stall-width parameter	[-]
Δ	Spectral scaling parameter (GL)	[-]
δ	Boundary layer thickness	[m]
δ^*	Boundary layer displacement thickness	[m]
δ_p^*, δ_s^*	Pressure/suction side displacement thickness	[m]
Θ, Φ	BPM directivity angles	[rad] or [°]
θ_0	Observer elevation angle (GL)	[°]
λ	Wavelength	[m]
σ	Blade solidity or standard deviation	[-]
ψ_{TE}	Trailing edge angle	[°]
Ω	Rotational speed	[rad/s] or [rps]
ω	Angular frequency or win rate	[rad/s] or [-]

1

Introduction

Aviation is widely recognised as a major contributor to environmental impacts, including greenhouse gas emissions and noise pollution. Concern over these problems is still growing among the public, especially in densely populated areas near large airports [3]. One well-known example is Schiphol Airport in the Netherlands. Schiphol, the community and policymakers are constantly engaged in discussions on reducing aircraft noise and environmental impact [4].

In response to societal pressure and stricter regulations, the aerospace industry is actively developing technologies to achieve quieter, cleaner flight [5]. Notable innovations include electric propulsion and hydrogen-based solutions. Although these electrically propelled aircraft eliminate or reduce combustion and exhaust noise, propeller-generated aerodynamic noise remains a dominant contributor to the overall acoustic signature [6]. To mitigate the noise impact, models capable of accurately predicting propeller-driven noise under realistic operating conditions are required.

In addition to these environmental factors, aviation is undergoing a change due to the rise of Urban Air Mobility (UAM). Innovations such as electric vertical take-off and landing (eVTOL) vehicles have attracted significant attention. Companies such as Joby Aviation [7] and Archer Aviation [8] are developing passenger-sized vehicles intended for regional travel. These vehicles primarily use propeller or rotor propulsion systems and are expected to operate near urban populations, where noise exposure is highly relevant.

Despite the widespread use of propellers in emerging UAM vehicles and electrically propelled aircraft, predicting propeller noise remains challenging [9]. Propeller noise consists of two main components: tonal noise and broadband noise. Tonal noise originates from the periodic displacement of air by the rotating blade sections and (un)steady blade loading. Due to its harmonic nature, tonal noise shows up as discrete frequency peaks in the acoustic spectrum [6]. Broadband noise can be related to turbulent inflow and turbulent flow developed on the blade surface and typically has a stochastic character [10]. This results in a continuous frequency spectrum, with acoustic energy distributed over a wide range of frequencies. Prior research has already focused on the prediction of the tonal noise [11][12][13]. However, modelling and understanding the dominant sources of broadband noise is crucial for understanding the complete acoustic signature of propellers [14][15]. It enables a more realistic assessment of propeller noise from a perceptual perspective, as tonal noise alone does not reflect the sound an observer experiences.

In this thesis, a computational framework has been developed to assess broadband noise models for (electrically driven) propellers across multiple flight regimes. The framework utilises geometric and aerodynamic inputs and is integrated with (semi-)empirical broadband prediction models. The accuracy, consistency, and physical behaviour of these models are systematically evaluated. The validation was conducted using experimental data from a scaled propeller under hover conditions, representative of UAM operations. Additional validation involved the experimental data of a fully electric single-propeller aircraft in forward flight.

1.1. Research Objective

The primary research objective of this thesis is to develop and validate a framework for accurately predicting broadband noise generated by propellers, and to evaluate its performance across hover and forward flight conditions using experimental data. The framework is intended to enable consistent broadband noise prediction for emerging Urban Air Mobility and fixed-wing electric aircraft.

1.2. Research Questions

To achieve this objective, the following main research question is addressed in this thesis:

> **"How can broadband noise from electrically driven propellers be predicted using existing (semi-)empirical models, and to what extent do these models remain applicable across hover and forward flight operating conditions?"**

To address this question, several sub-questions have been formulated:

1. **What are the dominant sources of broadband noise in electrically driven propellers, and how does their relevance depend on operating conditions?**
    - What broadband noise components are identified in the literature for propellers?
    - How do flow conditions, such as Reynolds number and angle of attack, influence the dominance of different broadband noise sources?
2. **Which modelling approaches are available for predicting broadband noise of propellers, and how do their assumptions, input requirements, and computational costs affect their applicability?**
    - How do analytical methods represent broadband noise sources?
    - How does the fidelity of the aerodynamic input influence broadband noise prediction accuracy and computational cost?
    - How do (semi-)empirical models balance physical realism and computational efficiency in broadband noise prediction?
    - How are broadband noise models implemented in practical prediction toolchains?
    - What role can machine learning play in broadband noise prediction, and what are its current limitations?
3. **Which broadband noise prediction approach provides the most suitable balance between accuracy, computational cost, and practicality for electrically driven propellers in hover and forward flight?**
    - How can broadband noise prediction methods be grouped into coherent end-to-end prediction approaches?
    - Which criteria are most relevant for evaluating broadband noise prediction approaches in the context of this thesis?
4. **How can the selected broadband noise prediction approach be implemented in a modular and physically consistent framework?**
    - What are the (aerodynamic) inputs required for the broadband noise prediction approach?
    - How can the aerodynamic and acoustic models be coupled within the broadband noise prediction framework?
5. **How closely does the implemented framework reproduce measured broadband noise for published experimental data?**
    - How accurately do the broadband noise models predict measured propeller broadband noise in hover and forward flight conditions?
6. **Under which conditions do the implemented models fail to reproduce physically realistic behaviour?**

- How do these limitations relate to model assumptions and formulations?

1.3. Thesis Outline

The structure of this report[1] aligns with the sub-questions formulated above. The dominant sources contributing to broadband noise in propellers (sub-question 1) will be introduced in chapter 2. This chapter will be followed by a review of the available literature on broadband noise prediction models (sub-question 2) in chapter 3. Drawing from this review, a trade-off between the identified prediction approaches will be presented in chapter 4 (sub-question 3). The result from this trade-off forms the basis for the broadband noise prediction framework, whose methodology will be described in chapter 5 (sub-question 4). The developed acoustic models will be verified in chapter 6 to ensure that the reproduced results match those reported in the original model publications. Subsequently, chapter 7 will present the validation of both the aerodynamic and acoustic models using two independent experimental data sets: one for hover and one for forward flight (sub-question 5). The prediction framework is then applied to a forward flight take-off case study, with results presented in chapter 8 (sub-questions 5 and 6). Finally, the conclusions, limitations and recommendations will be given in chapter 9. Readers seeking additional background information on aircraft noise fundamentals and digital signal processing concepts can refer to Appendix A.

[1] Grammarly was used as a proofreading tool to improve grammar and language quality. (Grammarly, 2026, Grammarly Inc., https://www.grammarly.com/handbook/)

2

Dominant Sources of Broadband Noise of a Propeller

This chapter will document the dominant sources of broadband noise of propellers. A breakdown of the different components of propeller noise can be found in Figure 2.1. Broadband noise generated by propellers is typically classified into three main categories: blade-wake interaction, turbulent inflow noise, and trailing edge noise (often referred to as self-noise) [9][10]. These three categories will be elaborated on in the following sections. A discussion on the tonal noise components can be found in Appendix A.1.4.

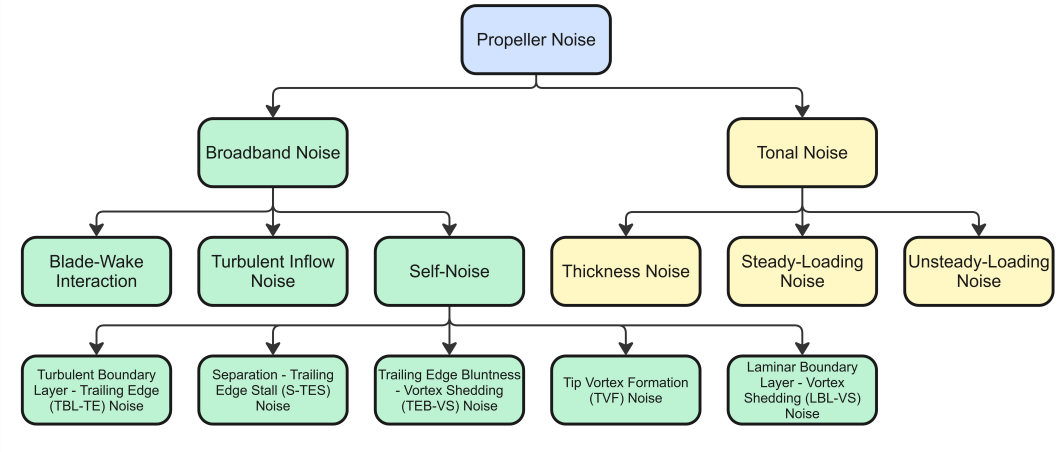

Figure 2.1: Overview Dominant Sources / Components of Propeller Noise

2.1. Blade-Wake Interaction

Blade–wake interaction (BWI) is a broadband noise source in rotating lifting systems, characterised by a mid-frequency spectral peak. Brooks et al. first identified BWI noise during wind tunnel experiments on a scaled helicopter rotor in the Duits-Nederlandse Windtunnel (DNW) [16]. They showed that the noise mechanism was associated with interactions between rotor blades and previously shed blade wakes, rather than with the ingestion of atmospheric turbulence as previously assumed [17]. Consequently, the strength and spectral content of BWI noise depend on the rotor or propeller's operating conditions that influence wake convection and re-ingestion.

2.2. Turbulent Inflow Noise (Leading Edge Noise)

The aerodynamic loading on a propeller blade can be unsteady and may include a stochastic component. This phenomenon leads to what is known as turbulent inflow leading edge (TI-LE) noise. The source of this unsteady aerodynamic loading often originates from turbulence present in the free stream, which strikes the leading edge of a rotating or stationary blade [18]. This source of broadband noise is therefore particularly dominant if a propeller is operating in a turbulent flow or downstream of any obstacle [10].

2.3. Self-Noise (Trailing Edge Noise)

Noise generated by turbulence and boundary layer unsteadiness is often referred to as 'trailing edge noise' or 'self-noise'. Self-noise includes turbulent boundary layer – trailing edge interactions, separation noise, vortex shedding from blunt trailing edges, tip vortex interactions, and noise resulting from laminar separation bubbles [1]. Each self-noise mechanism will be elaborated on in the following subsections.

2.3.1. Turbulent Boundary Layer - Trailing Edge (TBL-TE) Noise

Turbulent Boundary Layer - Trailing Edge (TBL-TE) noise is the most dominant component of self-noise. It originates from the interaction between turbulence in the boundary layer and a sharp solid edge, such as the trailing edge of an airfoil or propeller blade [1]. When turbulent flow interacts with the surface, it generates random pressure fluctuations. The resulting turbulent kinetic energy is converted to acoustic energy when it encounters a change in the boundary conditions imposed by the trailing edge. The resultant noise has a mid- to high-frequency peak. This peak frequency, where noise levels become maximum, is often estimated using Equation 2.1 [19]. In this equation, V_∞ is the freestream velocity, f is the frequency at which TBL-TE noise peaks, and δ^* is a boundary layer displacement thickness. A schematic of the formation of TBL-TE noise can be found in Figure 2.2.

$$\frac{f \cdot \delta^*}{V_\infty} = 0.06 - 0.08 \tag{2.1}$$

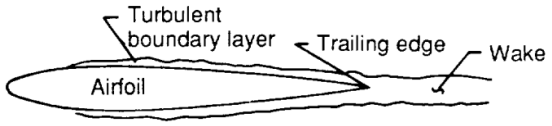

Figure 2.2: Turbulent Boundary Layer - Trailing Edge Noise [1]

2.3.2. Separation - Trailing Edge Stall (S-TES) Noise

For airfoils or propeller blades operating at a high angle of attack, the flow may separate from the surface on the suction side near the trailing edge, as shown in Figure 2.3. In mild separation, the boundary layer becomes unstable and radiates noise. As separation grows into a deep stall, more of the airfoil surface contributes to unsteady vortex formation and lower-frequency noise radiation. Stall-induced noise has been observed to exceed TBL-TE noise by more than 10 dB in severe cases [1].

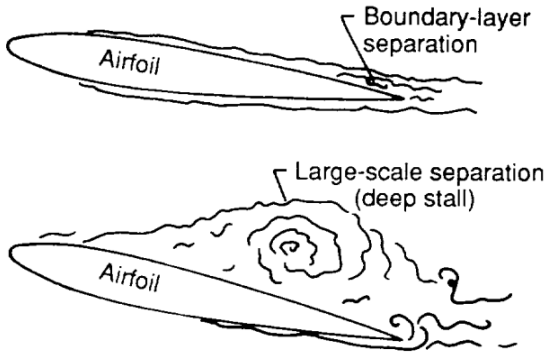

Figure 2.3: Seperation - Trailing Edge Stall Noise [1]

2.3.3. Trailing Edge Bluntness - Vortex Shedding (TEB-VS) Noise

Blunt trailing edges can induce vortex shedding similar to that observed behind bluff bodies. This vortex shedding again leads to alternating pressure zones and generates a high-frequency broadband noise component. Although usually secondary to TBL-TE noise, TEB-VS noise can become significant for blades with a substantial trailing edge thickness compared to the thickness of the boundary layer [1]. Its magnitude depends on both the bluntness geometry and the boundary layer properties at the trailing edge [20].

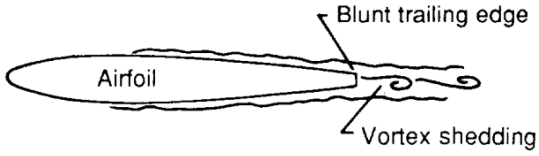

Figure 2.4: Trailing Edge Bluntness - Vortex Shedding Noise [1]

2.3.4. Tip Vortex Formation (TVF) Noise

As the propeller blade generates lift (or thrust), the pressure difference between the pressure side and the suction side of the blade drives flow around the tip [20]. This results in the formation of tip vortices. This vortex contains highly turbulent flow, which can result in a high-frequency Tip Vortex Formation (TVF) broadband noise when it interacts with the trailing edge [1]. The tip vortex formation is visualised in Figure 2.5. This noise source is usually relatively unimportant when other self-noise mechanisms are present due to its low amplitude [20].

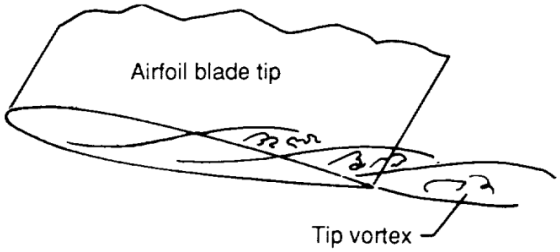

Figure 2.5: Tip Vortex Formation Noise [1]

2.3.5. Laminar Boundary Layer - Vortex Shedding (LBL-VS) Noise

Another source of broadband noise is Laminar Boundary Layer - Vortex Shedding (LBL-VS) noise [1]. LBL-VS originates from the vortex shedding induced by laminar separation bubbles on airfoil or blade surfaces [21]. A laminar boundary layer separates from an airfoil or rotor blade when it encounters

an adverse pressure gradient. This separated flow often transitions to turbulence. The flow gets re-energised and therefore reattaches downstream. This forms a closed recirculating region, also called a laminar separation bubble. The transition to turbulence is frequently associated with the formation and shedding of vortices [22]. These vortices can interact with the trailing edge and radiate acoustic energy. While vortex shedding leads to tonal peaks in fixed 2D airfoils, it manifests as a high-frequency, broadband "whistling" noise in rotating systems such as propellers [23]. LBL-VS noise typically occurs for Reynolds numbers between $Re = 5 \times 10^4$ and $Re = 2 \times 10^6$ and at low angles of attack (up to $\alpha = 5°$) where laminar separation bubbles are prone to form [23]. This broadband noise source can be prevented by tripping the boundary layer to induce turbulence.

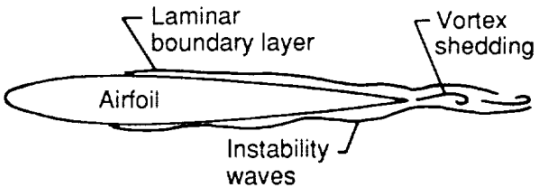

Figure 2.6: Laminar Boundary Layer - Vortex Shedding Noise [1]

2.4. Scope of the Broadband Noise Modelling

The previous (sub-)sections described the dominant sources contributing to broadband propeller noise. These included blade–wake interaction (BWI), turbulent inflow leading edge (TI-LE) noise, and various trailing edge noise mechanisms. However, not all broadband noise components are considered in the prediction framework developed in this thesis. Based on the trade-off and sensitivity analysis presented in section 4.3, the modelling effort is limited to noise sources associated with trailing edge self-noise mechanisms.

This decision is motivated by several considerations. First, trailing edge noise, in particular TBL-TE noise, is generally the most dominant broadband contribution for propellers operating in clean flow conditions [24]. Second, the selected semi-empirical prediction models in chapter 4, namely the Brooks, Pope, and Marcolini (BPM) and Gill and Lee (GL) models, are specifically formulated to capture the spectral characteristics of trailing edge broadband noise.

In contrast, broadband mechanisms such as turbulent inflow noise and blade–wake interaction noise require additional modelling of upstream turbulence and wake convection. These fall outside the scope of the present framework. Consequently, the following chapter, chapter 3, will focus mainly on the existing prediction methods for trailing edge broadband noise.

3

Prediction Models for Broadband Noise of a Propeller: A Review

This chapter will present an overview of the state of the art in trailing edge broadband noise prediction methods for propellers. In section 3.1, existing analytical methods for trailing edge noise will be discussed. Next, section 3.2 will discuss numerical flow solvers categorised by fidelity level. Then, section 3.4 will present (semi-)empirical models for wall-pressure spectra and far-field noise prediction. Existing industrial toolchains are reviewed thereafter in section 3.5. Finally, emerging machine learning approaches for broadband noise prediction will be discussed in section 3.6. The modelling components described in this chapter will be synthesised into complete broadband noise prediction approaches in chapter 4. Furthermore, in chapter 4 the different modelling strategies are compared and a suitable approach for the present study will be selected.

3.1. Analytical Trailing Edge Noise Methods

Analytical methods provide the theoretical foundation for broadband trailing edge noise prediction by establishing a relationship between surface pressure fluctuations and far-field sound radiation. The foundation of most analytical methods lies in acoustic analogies. An acoustic analogy links the sources of sound to the perceived sound by an observer. The methods described below provide physical insight and scaling laws that are important in many broadband noise frameworks.

3.1.1. Ffowcs Williams and Hall Trailing Edge Noise Method

Trailing edge noise can be better understood by simplifying the model to ignore the airfoil's chord and thickness. In this approach, the noise generation is treated as coming from the edge of a semi-infinite flat plate subject to turbulence. Ffowcs Williams and Hall [25] analysed this simplified problem by applying Lighthill's acoustic analogy [19]. They used an exact formulation for Green's function and disregarded the non-isentropic and viscous effects on to the Lighthill stress tensor [24].

The resulting expression for the far-field sound frequency spectrum, S_{pp}, is shown in Equation 3.1, where $S(\omega)$ is the normalised spectral shape function [24]. In this equation, θ is the observer angle and ϕ denotes the angle taken with respect to the trailing edge. L and u represent the length scale of the turbulence and the velocity, respectively. Furthermore, b is the span. An overview of the nomenclature can be found in Figure 3.1. According to this formulation, at high frequencies, where the airfoil chord is large compared to the acoustic wavelength, trailing edge noise exhibits a strong dependence on the fifth power of the flow velocity [25].

$$S_{pp}(\mathbf{x}, \omega) \sim \frac{\sin\phi \sin^2\left(\frac{1}{2}\theta\right) \rho_o^2 U^3 u^2 L b \cos^2\Lambda_o}{|\mathbf{x}|^2 c_\infty} S(\omega) \tag{3.1}$$

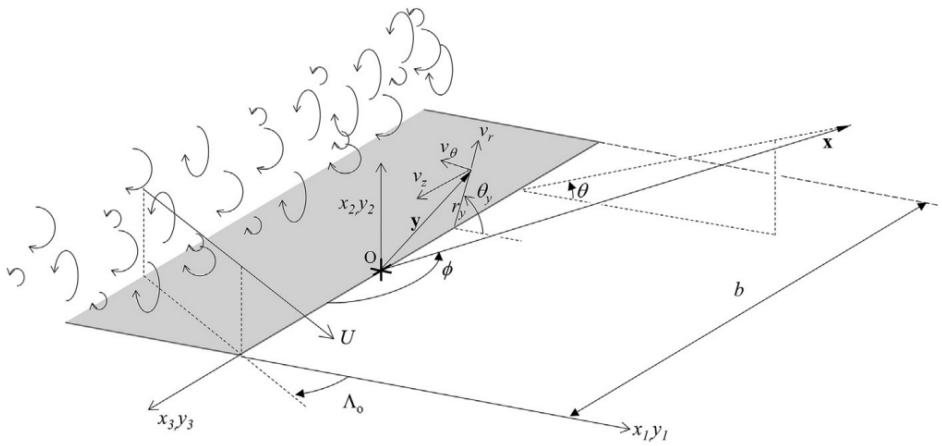

Figure 3.1: Nomenclature Trailing Edge modelled as Semi-Infinite Flat Plate of Zero Thickness [24]

The important outcomes from Ffowcs Williams and Hall's method are the directivity and scaling formulations. However, their trailing edge method assumes a stationary acoustic medium, i.e. zero mean flow [26]. This assumption limits the applicability of Ffowcs Williams and Hall's method in rotating blades.

3.1.2. Amiet's Trailing Edge Noise Method

To address these limitations, Amiet [26][27] proposed a more practical method for predicting trailing edge noise. He used surface-pressure data for a flat-plate boundary layer in his calculations. This was convenient, as it was a simple case and, perhaps even more importantly, the only readily available data [6].

The main input to Amiet's model is the wall-pressure spectrum (WPS). The WPS can be determined numerically. A discussion on the different numerical approaches will follow in section 3.2. The far-field noise spectrum for this method can be calculated using Equation 3.2 [26]. In this equation, x, y, and z are the coordinates in the axial direction, along the span, b, and $\sigma^2 = x^2 + \beta^2 z^2$, where $\beta^2 = 1 - M^2$. c_0 represents the speed of sound, s is the semispan, l_y is the spanwise correlation length, and $\mathcal{L}$ is the generalised lift. Finally, $S_{qq}(\omega, y)$ denotes the spanwise cross-spectrum surface pressure (reducing to the wall-pressure spectrum at zero spanwise separation) on either the upper or lower surface of the airfoil near the trailing edge [26]. The sound from both surfaces needs to be added to find the total noise. This can be done by adding the pressure spectra together if the two surfaces are uncorrelated [6].

$$S_{pp}(x, 0, z, \omega) = \left(\frac{\omega b z}{2\pi c_o \sigma^2}\right)^2 l_y(\omega) s |\mathcal{L}|^2 S_{qq}(\omega, 0) \tag{3.2}$$

More recently, Sinayoko et al. [28] developed a similar expression for trailing edge noise generated by rotating propeller blades. They derived expressions for both the instantaneous spectrum (Equation 3.3) and the time-averaged power spectral density (Equation 3.4). The resulting equations were validated with Schlinker and Amiet [27].

$$S_{pp}\left(x_0, \omega, t\right) = \int_{R_h}^{R_t} \sum_{m=-\infty}^{+\infty} B(m\Omega) e^{-im(\gamma_0 - \pi/2)} \times \left(\sum_{n=-\infty}^{+\infty} \widetilde{I}_{n,n+m}(\omega, m\Omega, r)\right) e^{in\Omega t} dr \tag{3.3}$$

$$\bar{S}_{pp}\left(x_0, \omega\right) = \int_{R_h}^{R_t} B(0) \sum_{m=-\infty}^{+\infty} \widetilde{I}_n(\omega, m\Omega, r) dr \tag{3.4}$$

3.1.3. Roger and Moreau's Trailing Edge Noise Method

Roger and Moreau [29] revisited Amiet's trailing edge theory with two extensions. First, they introduced a correction for leading edge backscattering. This accounts for the interaction between the blade's leading edge and the incident turbulence. The acoustic signature in the far-field can be significantly influenced by this effect, particularly at low frequencies and at low Mach numbers [29]. For larger wind-turbine blades, this phenomenon can be disregarded, while it is more important for blades with a shorter chord length.

The second improvement involved extending Amiet's original method to three dimensions. In their approach, the wall-pressure field near the trailing edge is decomposed into subcritical and supercritical gust components. This decomposition allows for a more accurate estimation of the spectral shape and directivity of the radiated sound.

3.1.4. Howe's Approach

Howe [30] proposed an alternative formulation of the acoustic analogy. Unlike Lighthill's original acoustic analogy [19], which assumes that density can be only defined as a function of pressure, Howe's derivation begins with the ideal gas law, $p = \rho RT$. This results in the general wave equation provided by Equation 3.5. In this equation, enthalpy, B, is defined by Equation 3.6. S is the entropy, ω is the vorticity, c_p denotes the specific heat at constant pressure, and v is the total fluid velocity. Using this alternative formulation, Howe derived an expression for the far-field acoustic spectrum, similar to Amiet's, based on the surface pressure spectrum. This expression can be found in [19] and [30].

$$\begin{aligned}&\left[\frac{D}{Dt}\left(\frac{1}{c^2}\frac{D}{Dt}\right)+\frac{1}{c^2}\frac{Dv}{Dt}\cdot\nabla-\nabla^2\right]B=\nabla\cdot(\omega\times v-T\nabla S)\\&-\frac{1}{c^2}\frac{Dv}{Dt}\cdot(\omega\times v-T\nabla S)+\frac{D}{Dt}\left(\frac{T}{c^2}\frac{DS}{Dt}\right)+\frac{\partial}{\partial t}\left(\frac{1}{c_p}\frac{DS}{Dt}\right)\end{aligned} \tag{3.5}$$

$$B=\int\frac{dp}{\rho}+\frac{1}{2}v^2 \tag{3.6}$$

3.2. Numerical Flow Models for Broadband Noise Prediction

Broadband noise calculations often rely on accurate descriptions of the turbulent boundary layer near the blade surface. These include parameters such as surface pressure fluctuations, boundary layer thickness, turbulence intensity, and wall-pressure spectra (e.g., input to Amiet's method, section 3.1). These parameters are commonly derived from numerical flow simulations. The numerical models can be categorised by their level of fidelity.

3.2.1. Low-Fidelity Methods

Low-fidelity methods, such as XFOIL, Blade Element Momentum Theory (BEMT), and 2D panel methods, are commonly used during conceptual design phases. They estimate blade loading and boundary layer properties under simplified flow assumptions, often in two dimensions. Unfortunately, BEMT methods can yield imprecise predictions of the (post-)stall behaviour of highly loaded blade sections close to the propeller hub at low advance ratios [31].

These low-fidelity tools are often used in conjunction with one of the analytical models described above (see section 3.1) or a (semi-)empirical model (see section 3.4). For example, Casalino et al. [31] conducted a low-fidelity benchmark study using XFOIL, a second-order panel method, and BEMT to assess aerodynamic performance. They used Roger and Moreau [29] and seven semi-empirical wall-pressure spectrum models (see section 3.4) to predict the broadband noise. At mid and high frequencies, this low-fidelity approach showed satisfactory agreement with the experimental and the high-fidelity results [9]. While computationally efficient, these methods do not resolve turbulent structures or unsteady interactions. This limits their accuracy, especially at low frequencies.

3.2.2. Mid-Fidelity Methods

Mid-fidelity simulations typically employ (un)steady Reynolds-Averaged Navier–Stokes (RANS or URANS) solvers, or hybrid approaches such as Detached Eddy Simulation (DES). These methods

provide three-dimensional blade loading, flow separation behaviour, and estimates of turbulence quantities. They are well-suited for capturing the statistical properties of the flow field, which can serve as inputs to acoustic analogies or semi-analytical broadband models.

For example, Su Jung et al. [32] evaluated the broadband noise prediction of a DJI 9443 CF rotor using a mid-fidelity approach. They applied both 2D and 3D RANS simulations to compute boundary layer properties. Furthermore, they combined these boundary layer properties with effective angle of attack estimates from either 3D RANS or the FLIGHTLAB framework. These flow parameters were then used as input for a broadband noise prediction model called BPM, which will be described in section 3.4. The study showed that the 3D RANS-derived effective angle of attack gave better agreement at high frequencies. FLIGHTLAB underpredicted low- and mid-frequency broadband sources, particularly those associated with LBL–VS. Furthermore, predictions based on 2D boundary layer parameters showed better agreement with experimental data than those from 3D RANS simulations. This could be because the underlying empirical corrections in the broadband noise model were based on 2D measurements [9].

Furthermore, unsteady RANS (URANS) solvers, such as OVERFLOW2, have been combined with acoustic toolchains, such as NASA's Aircraft Noise Prediction Program (ANOPP) (see section 3.5), to predict broadband noise spectra of rotorcraft [15]. Although this study showed an underprediction in the mid-frequency range, the overall trends of the broadband noise predictions agreed with the experimental data. Mankbadi et al. [33] used Detached Eddy Simulation (DES) to capture broadband noise. DES is a hybrid method between LES (see "High-Fidelity Methods" below) and URANS. They used DES to simulate the aerodynamic performance and broadband noise of a 9-inch DJI propeller in hover. Their DES framework used LES in the outer flow and unsteady RANS near the wall to balance computational cost and accuracy. The far-field noise was predicted using Farassat's 1A formulation [34]. The results showed that predictions based on a permeable control surface matched experimental data well. However, impermeable surface predictions significantly underpredicted the noise levels.

3.2.3. High-Fidelity Methods

High-fidelity methods resolve time-dependent flow features. This allows for accurate characterisation of turbulent flow. Large Eddy Simulation (LES) models only the small-scale eddies through subgrid-scale (SGS) models, whereas it resolves the large-scale turbulent structures in the flow [9]. This results in high physical accuracy but is computationally expensive. A more efficient alternative is the Implicit LES (ILES). ILES relies on numerical dissipation instead of an explicit SGS model. Kunz et al. [35] employed ILES to simulate broadband noise of a propeller in forward flight in combination with Farassat's Formulation 1A [34]. Overall, their results showed satisfactory agreement with experimental data. However, discrepancies were noted at low and mid frequencies, possibly due to background noise.

The Lattice Boltzmann Method (LBM) offers an alternative high-fidelity computational fluid dynamics (CFD) technique by solving mesoscopic kinetic equations instead of the macroscopic Navier–Stokes equations [9]. In PowerFLOW, LBM is coupled with Very-Large Eddy Simulation (VLES) [31]. Thurman et al. [36] used PowerFLOW (LBM–VLES) in combination with Farassat's Formulation 1A [34] to simulate the broadband noise of a DJI-9450 propeller. Their simulations matched experimental trends well but showed overprediction below 1.5 [kHz] and above 10 [kHz]. The lower-frequency discrepancies were linked to differences in simulated and physical turbulence structures. The high-frequency errors were linked to mesh size.

Direct Numerical Simulation (DNS) remains the most accurate high-fidelity approach, though it requires significant computational resources. It resolves all turbulent scales without modelling. However, DNS is currently limited to low Reynolds number flows (slightly above $Re = 10^5$ can be achieved [19]) and simplified configurations due to its extreme computational cost.

3.3. Experimental Methods

Experimental measurements serve as reference data for validating and calibrating predictive models. Typically, measurements are performed in wind tunnels using microphone arrays and pressure sensors. For instance, rotor model testing in the Duits-Nederlandse Windtunnel (DNW) contributed to the development of the BARC (Broadband Acoustic Rotor Codes) toolchain [20] (see section 3.5). In addition

to validation, experimental data can also be used to derive or inform empirical noise models (see section 3.4) by providing input parameters such as turbulence spectra or surface pressure statistics. Experiments offer high accuracy. However, they are costly and limited in scalability for design iteration.

3.4. (Semi-)Empirical Models

As discussed earlier, the wall-pressure spectrum forms a key input for both Howe's and Amiet's formulations, as well as for extensions of these two methods, such as the Roger and Moreau approach. In practice, this wall-pressure spectrum is typically estimated using empirical or semi-empirical models [19]. For instance, Amiet relied on an empirical model based on the measurements reported by Willmarth and Roos [37].

3.4.1. Empirical (WPS) Models

Empirical models are data-driven approaches developed by fitting analytical expressions to experimental observations [38]. These models typically predict wall-pressure spectra or far-field broadband noise based on simplified flow descriptors, such as boundary layer thickness, turbulence intensity, or flow velocity. One of the most influential models is Goody's model [39], which provides a spectral representation of wall-pressure fluctuations under zero pressure gradient conditions. As noted by Glegg and Devenport [38], Goody's model performs well across a broad range of cases. In 2009, Hwang et al. [40] conducted a comparative analysis of multiple empirical models available at the time. They concluded that Goody's formulation provided the best overall prediction accuracy across the evaluated frequency spectra.

However, over time, limitations in these earlier models became evident. In a 2018 review, Lee [41] assessed several existing wall-pressure spectrum models, including Goody's [39], and observed that none consistently performed satisfactorily across varying geometries and pressure gradients. Therefore, Lee developed a new empirical model. This model demonstrated improved accuracy for flows with zero and adverse pressure gradients, and for small favourable pressure gradient flows [41].

Building on this model, Gill and Lee [2] improved the new empirical broadband noise prediction model by incorporating noise data from a broad range of rotors. This dataset includes small UAV rotors, mid-sized propellers, and large helicopter rotors [2]. This model, formally known as the GL model, was developed using Gene Expression Programming. Gene Expression Programming is a machine learning (ML) algorithm that enables the creation of an optimised spectral formulation using only fundamental rotor performance parameters. First results show that this new empirical model provides substantial agreement with experimental data.

Empirical models remain limited by the scope of the data on which they are based or trained. However, their simplicity and computational efficiency make them an attractive choice for broadband noise prediction. More recent efforts to integrate machine learning techniques will be discussed in section 3.6.

3.4.2. The BPM Model

Amiet's theory provides the theoretical link between boundary layer surface pressure fluctuations and the far-field acoustic signature. However, it requires detailed knowledge of boundary layer properties near the trailing edge. This information is not always known or easy to measure. The Brooks, Pope, and Marcolini (BPM) model [1] avoids this limitation by taking a more empirical approach. The BPM model is the most widely employed semi-empirical approach for predicting airfoil self-noise of the past thirty years [19].

Instead of attempting to measure the fluctuating pressures within the boundary layer itself, Brooks, Pope, and Marcolini opted to measure the far-field acoustic output [1]. They tested a wide range of NACA 0012 airfoils (different sizes), Reynolds numbers, and angles of attack in an anechoic wind tunnel. This provided them with a comprehensive dataset of self-noise spectra under controlled conditions. The measured spectra were then scaled based on the formulation of Ffowcs Williams and Hall (Equation 3.1) to produce normalised spectral shapes. From these, correlations for the boundary layer scaling parameters were derived as functions of the operating conditions [24].

The BPM model can be used to predict each individual self-noise component described in section 2.3, namely Turbulent Boundary Layer - Trailing Edge (TBL-TE) noise, Trailing Edge Bluntness - Vortex

Shedding (TEB-VS) noise, Tip Vortex Formation (TVF) noise, Separation - Trailing Edge Stall (S-TES) noise, and Laminar Boundary Layer - Vortex Shedding (LBL-VS) noise. Each self-noise component is characterised by a spectral shape function and scaling parameters obtained from experimental measurements. The correlations themselves are grounded in aeroacoustic theory. By combining physics-based scaling with data-driven fitting, the BPM model is considered semi-empirical rather than purely empirical. The scaling laws and full calculation procedures for each self-noise component are presented in [1] and will be elaborated on in section 5.5.

3.4.3. The TNO Model

The TNO model is a semi-empirical trailing edge noise model developed by Parchen [42] at the Netherlands' TNO Institute of Applied Physics. The TNO framework combines a theoretical wall-pressure spectrum formulation with an acoustic scattering model. The wall-pressure spectrum is based on Blake [43] to approximate the pressure fluctuations in the turbulent boundary layer near the trailing edge. These fluctuations are then converted into far-field noise using Howe's model [30] (see section 3.1). In some implementations, Amiet's method [26] is used. An advantage of the TNO model is its flexibility in sourcing the aerodynamic input data required to define the boundary layer properties at the trailing edge [19]. These inputs can be obtained either from low-cost aerodynamic solvers such as XFOIL or from higher-fidelity RANS CFD simulations [44].

The original TNO formulation has shown good performance at high frequencies and moderate angles of attack. However, it underpredicts noise levels at low and mid frequencies [44] and at high angles of attack [45]. These limitations have motivated several improvements. Bertagnolio et al. [46] introduced an empirical-tuning correction to better capture the influence of angle of attack. Fischer et al. [45] refined the model by removing Blake's simplifying assumptions and fully modelling the turbulence cross-correlation terms. This improved TNO model showed significantly better agreement between predicted and measured surface-pressure spectra, as well as between far-field noise predictions and measurements. Importantly, the computational cost remained only slightly higher than that of the original TNO model.

3.5. Existing Toolchains for Broadband Prediction

Broadband noise prediction methods are often embedded within larger computational toolchains. In these toolchains, (semi-)empirical and analytical models are often combined with aerodynamic data from varying levels of fidelity. Below, some toolchains that implement the BPM or other broadband noise models will be discussed.

BPM Toolchains

The BPM model has been implemented in several acoustic toolchains. NASA's Aircraft Noise Prediction Program (ANOPP) [47] incorporates BPM alongside other semi-empirical models, including Grosveld's approach [48] for TEB-VS noise and the Schlinker and Amiet formulation [27] for TBL-TE and S-TES [1]. OpenFAST [49] similarly integrates BPM for wind turbine aeroacoustic prediction. Blake et al. [50] predicted self-noise using the BPM method implemented within the ANOPP2 Self-Noise Internal Functional Module (ASNIFM).

UCD-QuietFly

For urban air mobility applications, the UCD-QuietFly framework [51][52][53] combines Amiet's method, BEMT, XFOIL, and the empirical wall-pressure spectrum model developed by Lee [41] to predict trailing edge noise. Li and Lee [51] validated UCD-QuietFly against experimental data for an SUI Endurance rotor, a NASA ideally twisted rotor, and a DJI-CF propeller. The predictions showed good agreement with measurements for small-scale rotors in the mid- to high-frequency range.

TELE-Noise and BARC

TELE-Noise is a semi-analytical code capable of modelling both trailing edge and leading edge broadband noise by relating turbulence statistics from RANS or LES to far-field sound predictions [18]. A similar hybrid framework, called Broadband Acoustic Rotot Codes (BARC) [20], combines analytical theory with experimental surface pressure data. The flexibility of such toolchains makes them attractive for industry applications, where aerodynamic and acoustic inputs may come from disparate sources and computational budgets vary.

Time-Domain Toolchains
Time-domain broadband noise prediction toolchains directly solve the unsteady acoustic equations, often using Farassat's formulations [34] or the Ffowcs Williams–Hawkings (FW-H) equation [54]. These formulations can be implemented in toolchains, as done in ASSPIN [55].

3.6. Machine Learning Approaches

Two general strategies for incorporating machine learning (ML) into broadband noise prediction can be identified. The first is a hybrid approach that uses ML to replace computationally expensive numerical flow simulations. In this case, a model is trained on high-fidelity data. Once trained, it can generate flow fields much faster than the high-fidelity methods. These flow fields are then used in conventional acoustic analogies to predict far-field noise. The second approach is to train ML models on large experimental databases to estimate broadband noise levels directly under conditions similar to those in the experiments.

Following the hybrid approach, Kunz et al. [56] attempted to predict broadband noise using a Fast Random Particle Mesh (FRPM) model and machine learning techniques. The FRPM framework provided a computationally efficient means of generating synthetic turbulent fields for aeroacoustic applications, compared to high-fidelity simulations. However, limitations, such as inaccuracies in the amplitude and smoothness of the generated velocity fluctuations, were identified. Therefore, machine learning was used to enhance the prediction of the turbulence amplitude parameter within the FRPM model. The initial results are promising. However, further refinement of the learning objective is required to more accurately predict the noise sources.

Redonnet et al. [57] focused on predicting airfoil self-noise, specifically TBL–TE noise, of the NACA0012 airfoil. They trained a deep neural network (DNN) on a NASA experimental database of the NACA0012 airfoil. The DNN was then benchmarked against the classical semi-empirical BPM model. The DNN consistently outperformed the BPM model in accuracy. It achieves mean prediction errors of 1.5–2.5 [dB] for sound pressure levels. However, further research is required to assess the accuracy of this deep neural network across different airfoils and operating conditions.

In conclusion, recent developments in machine learning have shown promise for predicting propeller broadband noise. ML models trained on high-fidelity simulations or experimental data can serve as fast surrogates to predict broadband noise. These methods are still in development, but can potentially play an important role in (broadband) noise prediction in the future.

4

Broadband Noise Prediction Approach and Model Selection

From the extensive literature review in chapter 3, it can be concluded that the individual components of broadband noise prediction are highly interconnected. Many models cannot be compared in isolation because their accuracy, computational cost, etc., depend on different inputs, intermediate representations (such as wall-pressure spectra), and the acoustic analogy used. Therefore, in this chapter, different prediction approaches will be compared instead of comparing the individual (components of) models. With a prediction approach, a full modelling framework from input to far-field noise prediction is meant. The prediction approach that follows from the trade-off in this chapter will then be developed into a prediction toolchain in chapter 5.

4.1. Broadband Noise Prediction Approaches

The five distinct approaches identified from the literature study are presented in Table 4.1. These approaches are visualised using a flowchart in Figure 4.1. As illustrated in Figure 4.1, numerical methods can contribute by providing full-time-resolved pressure data (path 1) or by supplying boundary layer or rotor performance characteristics for downstream models (paths 2–3). Experimental data can serve as the basis for a new empirical prediction model (path 4), and this new model can be further enhanced using Machine Learning (path 5).

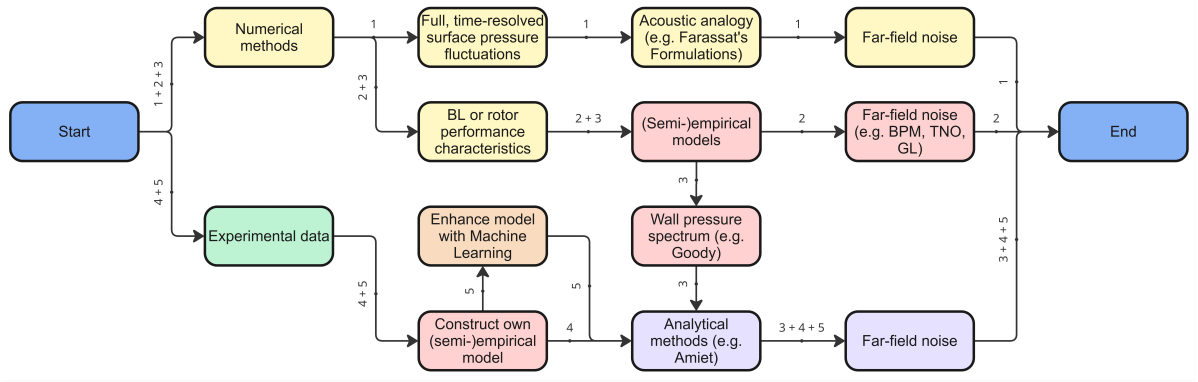

Figure 4.1: Flowchart of the Broadband Noise Prediction Approaches

Table 4.1: The Identified Broadband Noise Prediction Approaches

Path	Approach	Description
1	Numerical → time-resolved $p'(t)$ → acoustic analogy	Numerical flow solver provides full, time-resolved surface pressure fluctuations, which are directly used in an acoustic analogy (e.g., Farassat 1A) to compute far-field noise.
2	Numerical → BL or rotor performance characteristics → (semi-)empirical model → far-field	Numerical simulation provides boundary layer or rotor performance characteristics, which are used in a (semi-)empirical noise model (e.g., BPM, TNO, GL) that has an incorporated acoustic analogy to directly predict far-field noise.
3	Numerical → BL or rotor performance characteristics → WPS model → analytical model → far-field	Numerical simulation provides BL or rotor performance characteristics, which are used in a wall-pressure spectrum (WPS) model (e.g., Goody) to estimate the unsteady surface loading, then fed into an analytical radiation model (e.g., Amiet, Howe) for far-field prediction.
4	Experimental → construct new (semi-)empirical model → analytical model → far-field	Experimental noise data is used to construct a new empirical model, whose output is propagated to the far field using an analytical model.
5	Experimental → construct new (semi-)empirical model → Enhance with ML → analytical model → far-field	Experimental noise data is used to construct a new empirical model, enhanced by Machine Learning, whose output is propagated to the far field using an analytical model.

4.2. Trade-Off Criteria and Weights

The criteria in Table 4.2 have been selected to compare the five broadband noise prediction approaches. Prediction accuracy is weighted most heavily, since reliable agreement with experimental data is fundamental to any credible noise study. Computational cost is also emphasised. This reflects the need to balance prediction accuracy with efficiency in terms of computational time and data storage. Required input data captures the level of aerodynamic or acoustic detail demanded by the approach. Higher scores favour methods that work with more readily available inputs. Similarly, the experimental data demand criterion accounts for the fact that some methods rely heavily on extensive measurements, while others can function with minimal experimental support. Development time is included to account for the resources needed to implement and validate each method during this thesis. Finally, generalisability ensures that the chosen approach remains relevant across a broader range of propeller geometries, operating conditions, and configurations.

Table 4.2: Trade-Off Criteria for evaluating Broadband Noise Prediction Approaches

Criterion	Explanation	Weight
Prediction Accuracy	Expected reliability of far-field noise predictions compared to experimental reference data.	25%
Computational Cost	Computational time and storage requirements.	20%
Required Input Data	Type and level of detail of aerodynamic or acoustic input data needed. Higher scores mean less detailed or more easily obtainable inputs.	15%
Experimental Data Demand	Extent and complexity of physical measurements needed, and how easily these can be obtained. Higher scores mean lower experimental burden and better data accessibility.	15%
Development Time	Time needed to implement and validate the approach within the thesis duration.	15%
Generalisability	Ability of the method to be applied to different propeller geometries, operating conditions, and configurations.	10%

4.3. The Approach Trade-Off and Sensitivity Analysis

For each criterion, the possible approaches are assigned qualitative scores based on their expected performance. These scores are given in the trade-off table below, Table 4.3. This scoring process is inherently subjective and can strongly influence the outcome of the trade-off. Therefore, a sensitivity analysis is conducted to assess the sensitivity of the final ranking to changes in the assigned grades.

First, the average grade for a given criterion is calculated from all the paths' grades. It is assumed that the grades follow a normal distribution around the average (i.e., the mean). From there, the standard deviation can be determined. This standard deviation, noted as $\sigma = ...$, is displayed in the same cell as the criterion in Table 4.3. For each path, the given grade is then considered as the mean of its own normal distribution, with the standard deviation equal to the overall σ for that criterion.

From these distributions, random values are sampled for each path's grade. Once all grades have been sampled, the path with the highest score is marked as "the winner" for that iteration. This process is repeated 10 000 times. The proportion of iterations in which each path emerges as "the winner" is recorded as its win rate, denoted $\omega = ...$, next to the original score in Table 4.3. A significantly higher win rate compared to others suggests a clear superiority. On the other hand, similar win rates among multiple paths indicate that small changes in the assigned grades could alter the ranking.

In addition to the grades, the weighting assigned to each criterion can also influence the overall ranking. Therefore, a second sensitivity analysis has been performed. First, the total grade of each path is provided in the final column in Table 4.3. Then, the standard deviation for the weights, σ_w, was determined similarly to how this was done for the criteria grades. For each path, the total grade is considered as the mean of its own normal distribution, with the standard deviation equal to σ_w.

From these distributions, again, random values are sampled for each path's total grade. The path with the highest total grade is marked as "the winner" for that iteration. This process is repeated 10 000 times. The resulting win rates, ω, in the final column in Table 4.3 show how often each path is the preferred option when the weight of the criteria changes.

Table 4.3: Approach-Level Trade-Off Table

Criteria	Prediction Accuracy	Computational Cost	Required Input Data	Experimental Data Demand	Development Time	Generalisability	Total
	25.0%	*20.0%*	*15.0%*	*15.0%*	*15.0%*	*10.0%*	$\sigma_w = 0.05$
Options	$\sigma = 1.17$	$\sigma = 2.06$	$\sigma = 1.47$	$\sigma = 2.93$	$\sigma = 1.41$	$\sigma = 1.02$	
Path 1	10.0 $\omega = 0.67$	2.0 $\omega = 0.0$	5.0 $\omega = 0.03$	10.0 $\omega = 0.63$	6.0 $\omega = 0.1$	8.0 $\omega = 0.69$	6.85 $\omega = 0.13$
Path 2	7.0 $\omega = 0.01$	8.0 $\omega = 0.51$	8.0 $\omega = 0.64$	7.0 $\omega = 0.17$	8.0 $\omega = 0.61$	5.0 $\omega = 0.0$	7.3 $\omega = 0.85$
Path 3	8.0 $\omega = 0.07$	7.0 $\omega = 0.28$	7.0 $\omega = 0.29$	7.0 $\omega = 0.18$	7.0 $\omega = 0.26$	6.0 $\omega = 0.04$	7.15 $\omega = 0.02$
Path 4	7.0 $\omega = 0.01$	6.0 $\omega = 0.14$	5.0 $\omega = 0.03$	3.0 $\omega = 0.02$	5.0 $\omega = 0.02$	6.0 $\omega = 0.05$	5.5 $\omega = 0.0$
Path 5	9.0 $\omega = 0.24$	5.0 $\omega = 0.07$	4.0 $\omega = 0.01$	2.0 $\omega = 0.01$	4.0 $\omega = 0.01$	7.0 $\omega = 0.21$	5.45 $\omega = 0.0$

A trade-off performance polar plot based on the grades given in Table 4.3 is provided in Figure 4.2. Based on the trade-off and sensitivity analysis, path 2 was selected as the most suitable approach for developing a broadband noise prediction framework in this thesis.

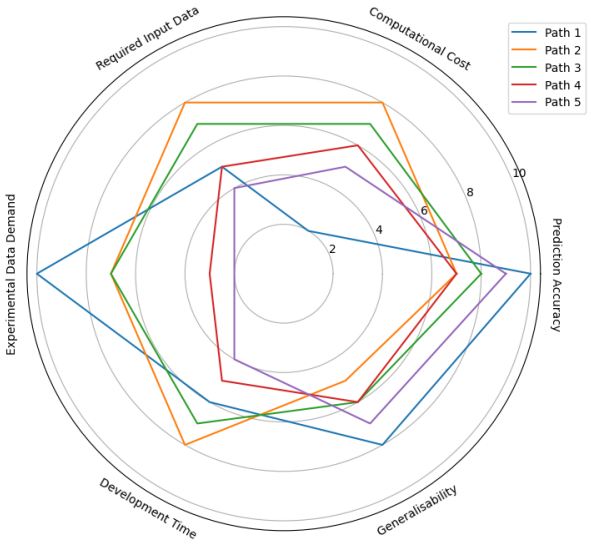

Figure 4.2: Trade-Off Performance Polar Plot

4.4. Considered (Semi-)Empirical and Numerical Models

Following the outcome of the trade-off, two (semi-)empirical models from Path 2 were selected and implemented in this thesis:

- The Brooks, Pope, and Marcolini (BPM) model [1]
- The Gill and Lee (GL) model [2]

The BPM model is a widely used, conventional method. It requires boundary layer parameters and inflow conditions and predicts broadband noise for a static airfoil section. The BPM results must therefore be converted to a rotating reference frame and integrated over the blade span when applied to a propeller. In contrast, the GL model represents a new empirical approach derived using machine learning. An advantage of GL over BPM is that it is formulated directly in terms of rotor (performance) characteristics and produces a full broadband sound pressure spectrum for a rotating propeller. The two models have not been directly compared in the literature to assess whether the newer and easier-to-use GL model matches or improves upon BPM in terms of accuracy. Furthermore, the GL model has been validated primarily for hover operating conditions, with only a single validation case available in forward flight. Therefore, these two models are implemented, verified and validated, applied to different flight cases, and compared in the next chapters.

The aerodynamic input required by the BPM and GL models will be generated using a low-fidelity Blade Element Momentum Theory (BEMT) framework in conjunction with sectional airfoil data from XFOIL. This approach aligns with previous studies, including the UCD-QuietFly methodology [51][52][53], which combined BEMT and XFOIL with empirical wall-pressure spectrum models, as well as a student design synthesis project that integrated BEMT with XFOIL and NeuralFoil for tonal noise estimation [58]. While less detailed than CFD-based methods, the BEMT/XFOIL combination provides all necessary aerodynamic inputs for the BPM and GL formulations at a minimal computational cost. This facilitates quick broadband noise evaluation across a range of operating conditions.

5

The Development of the Broadband Noise Prediction Framework

Based on the trade-off analysis in chapter 4, Path 2 was selected as the broadband noise prediction approach for this thesis. This chapter will describe the implementation of the broadband noise prediction toolchain developed for this thesis. The toolchain combines aerodynamic modelling based on the Blade Element Momentum Theory (BEMT) with two unrelated broadband noise models (the BPM and GL models) to predict the acoustic emission from an isolated propeller. All modules are integrated in a Python framework.

5.1. Overview of the Broadband Noise Prediction Toolchain

The broadband noise prediction framework consists of several components. A schematic representation of this workflow is provided in Figure 5.1. The process starts with the user providing all required inputs in the main input text file. These files, and their structure, are discussed in detail in section 5.2.

In the input file, the user can specify whether a Blade Element Momentum Theory (BEMT) analysis has already been carried out for the case under consideration. If a previously computed BEMT output file is provided, the toolchain loads this file directly. If no BEMT solution is available, the toolchain proceeds to perform a full BEMT analysis. This analysis will provide the local thrust distribution, effective velocity, and the angle of attack at each radial blade position. A more detailed description of the BEMT analysis will be given in section 5.3.

The aerodynamic outputs serve as the primary inputs to the two broadband noise models implemented in the toolchain, namely the Gill and Lee model [2] and the Brooks, Pope, and Marcolini model [1]. The details of these noise models, as well as the intermediate steps such as boundary layer parameter estimation and directivity computation, will be discussed in section 5.4 and section 5.5.

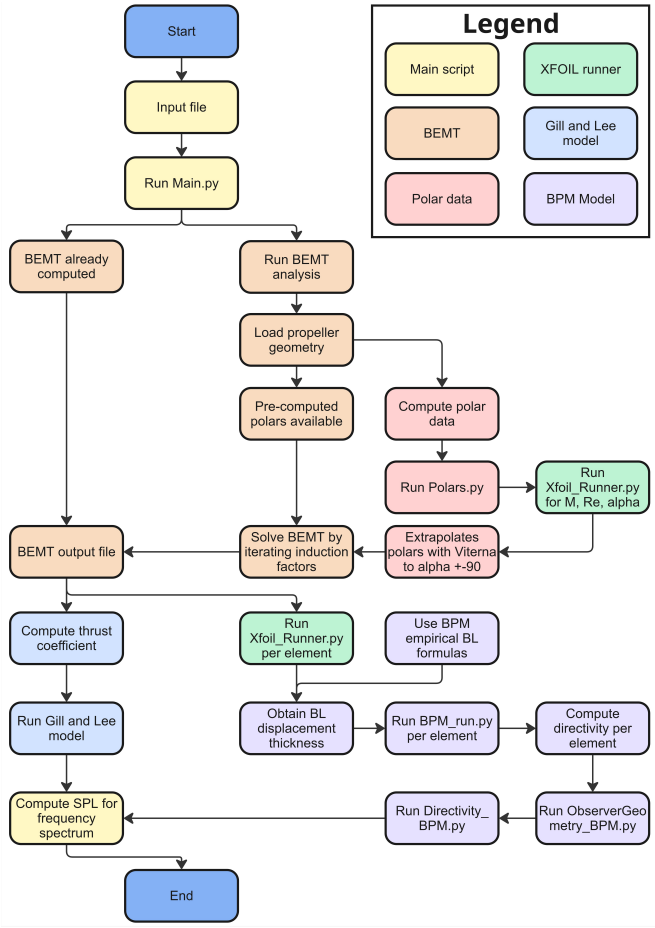

Figure 5.1: Flowchart of the Broadband Noise Prediction Toolchain

5.2. Model Input

The broadband noise prediction toolchain relies on a set of input files that define the geometric, aerodynamic, operational, and acoustic parameters required for the simulations. This section describes the content of these input files and explains how the user can configure the toolchain for different cases.

5.2.1. Propeller Geometry File

The propeller geometry file, which can be seen in Figure 5.2, provides the spatial distribution of the blade geometric properties. This file contains the radial position, twist, relative chord length, and airfoil information at each radial station of the blade. The airfoil coordinates are formatted following the XFOIL convention [59]. This means the airfoil coordinates are ordered from the trailing edge to the leading edge, then back to the trailing edge. The geometry file is referenced in the main input file, which is discussed below. This enables the user to switch between propeller configurations without modifying the underlying code.

```
R/Rp,          Twist[deg],     Chord/R,        Airfoil
0.250000,      16.843496,      0.111098,       Airfoil_rR0.250000
0.275000,      17.239553,      0.123299,       Airfoil_rR0.275000
0.300000,      17.090071,      0.132524,       Airfoil_rR0.300000
0.325000,      17.003599,      0.138452,       Airfoil_rR0.325000
0.350000,      16.774155,      0.141362,       Airfoil_rR0.350000
0.375000,      16.463179,      0.142550,       Airfoil_rR0.375000
0.400000,      15.027552,      0.141387,       Airfoil_rR0.400000
0.425000,      15.795998,      0.142224,       Airfoil_rR0.425000
0.450000,      13.567715,      0.140432,       Airfoil_rR0.450000
0.475000,      13.314288,      0.140035,       Airfoil_rR0.475000
0.500000,      12.786768,      0.136399,       Airfoil_rR0.500000
0.525000,      11.288682,      0.131532,       Airfoil_rR0.525000
0.550000,      11.031975,      0.130026,       Airfoil_rR0.550000
0.575000,      10.512068,      0.128948,       Airfoil_rR0.575000
0.600000,      9.894395,       0.126226,       Airfoil_rR0.600000
0.625000,      8.663667,       0.123290,       Airfoil_rR0.625000
0.650000,      8.367052,       0.120204,       Airfoil_rR0.650000
0.675000,      6.879022,       0.116835,       Airfoil_rR0.675000
0.700000,      6.792328,       0.114016,       Airfoil_rR0.700000
0.725000,      6.238451,       0.110975,       Airfoil_rR0.725000
0.750000,      5.664524,       0.107776,       Airfoil_rR0.750000
0.775000,      5.504046,       0.104631,       Airfoil_rR0.775000
0.800000,      4.238601,       0.097954,       Airfoil_rR0.800000
0.825000,      3.891329,       0.101375,       Airfoil_rR0.825000
0.850000,      3.768089,       0.094700,       Airfoil_rR0.850000
0.875000,      3.419512,       0.091309,       Airfoil_rR0.875000
0.900000,      3.123348,       0.087866,       Airfoil_rR0.900000
0.925000,      2.674458,       0.084609,       Airfoil_rR0.925000
0.950000,      2.890645,       0.080488,       Airfoil_rR0.950000
0.975000,      2.532004,       0.069288,       Airfoil_rR0.975000
```

Figure 5.2: The Propeller Geometry Input File

5.2.2. Main Input File

The main input file governs all parameters required to execute both the BEMT analysis and the broadband noise prediction. This text file is divided into several sections, which will be discussed below. The input file can be seen in Figure 5.3.

```
============== PROPELLER PARAMETERS ==============
Pipistrel ..................................... Case name
0.82 .......................................... Propeller radius [m]
3 ............................................. Number of blades
0.15 .......................................... Relative hub radius [r/R]
18.0 .......................................... Blade pitch angle [deg]
0.75 .......................................... Blade reference pitch location
20 ............................................ Number of blade radial segments
propeller_geometry_Pipistrel.csv .............. Input file describing propeller blade geometry
BEMT_output_pipistrel_FO1 ..................... Propeller BEMT output file (if already computed, otherwise: None)

============= OPERATIONAL PARAMETERS =============
2500 .......................................... Propeller RPM
41.7091 ....................................... Freestream velocity [m/s]

============= AERODYNAMIC PARAMETERS =============
19.5 .......................................... Ambient temperature [deg C]
67 ............................................ Relative humidity [%]
340.817 ....................................... Speed of sound [m/s]
1.8e-5 ........................................ Dynamic viscosity [m^2/s]
1.2156 ........................................ Air density [kg/m^3]

============== OBSERVER PARAMETERS ===============
0.0 ........................................... Observer x position [m]
12.1852 ....................................... Observer y position [m]
0.0 ........................................... Observer z position [m]
0.0 ........................................... Observer elevation angle for GL model [deg]

================ BEMT PARAMETERS =================
False ......................................... Compute new polars (True - yes, False - no)
True .......................................... Use general pre-computed polars (True - yes, False - no)
True .......................................... Compressibility correction
PG ............................................ Compressibility correction method ("PG" for Prantl-Glauert or "KT" for Karman-Tsien)
True .......................................... Root and tip loss correction
True .......................................... Glauert correction for heavily loaded propellers
BEMT_output ................................... Desired BEMT ouput file name

================ XFOIL PARAMETERS ================
1.0 ............................................ N_crit
1.0 ............................................ Transition location suction side
1.0 ............................................ Transition location pressure side
500 ........................................... Maximum iterations
False ......................................... Use Xfoil boundary layer parameters in BPM model

================ BPM PARAMETERS ==================
0 ............................................. Trip condition (0 - untripped, 1 - tripped)
True .......................................... Turbulent Boundary Layer Trailing Edge Noise / Separation Noise (True - on, False - off)
False ......................................... Laminar Boundary Layer Vortex Shedding Noise (True - on, False - off)
False ......................................... Trailing Edge Bluntness Noise (True - on, False - off)
False ......................................... Tip Vortex Formation Noise (True - on, False - off)

============= RESULTS and VALIDATION =============
Narrow ........................................ Spectral domain ("Octave" for 1/3 octave band or "Narrow" for narrow band)
False ......................................... Plot scaled propeller validation data
True .......................................... Plot single-propeller fully electric aircraft validation data
FO1 ........................................... Validation case ("FO1", "TO1", "TO2", or "TO3")
Overhead ...................................... Position w.r.t. observer ("Overhead", "45_degree_before_overhead", or "45_degree_after_overhead")
```

Figure 5.3: The Main Input File

Propeller Parameters
The first part of the main input file defines the primary propeller parameters. These include the propeller radius, the number of propeller blades, the hub radius ratio, the pitch setting and pitch reference location, and the number of radial blade elements used for aerodynamic discretisation. The file also specifies the filename of the propeller geometry file described in subsection 5.2.1. Additionally, this input file enables the user to supply a previously computed BEMT output file. If such a file is provided, the BEMT solver is bypassed. This reduces computational time when performing multiple acoustic analyses under identical operating conditions.

Operational Parameters & Aerodynamic Parameters
The operating conditions and aerodynamic parameters include the propeller rotational speed, the freestream velocity, the ambient temperature, the air density, and the relative humidity. They are used to determine the local flow conditions, Reynolds numbers, and Mach numbers along the blade span.

Observer Parameters
The observer parameters specify the observer's location in terms of its x, y, and z coordinates. These coordinates define the propagation distance and directivity angles used in the broadband noise models. The details of the general coordinate system will be discussed in subsection 5.5.3. For the Gill and Lee model, an observer elevation angle must also be provided. This angle follows from the definition provided in subsection 5.4.2.

BEMT Parameters
The input file also allows the user to configure the Blade Element Momentum Theory solver. Several correction models can be (de)activated. These correction models include compressibility corrections (either Prandtl–Glauert or Kármán–Tsien), Prandtl root and tip loss corrections, and the Glauert correction for heavily loaded propellers. The user can choose whether new aerodynamic polars must be computed for the analysis or whether existing polars should be used. If general precomputed polars are used, the solver loads data spanning Mach numbers of 0.00, 0.05, 0.25, and 0.50 and Reynolds numbers of 50 000, 150 000, 250 000, 350 000, and 450 000. Alternatively, when case-specific polars are desired, the toolchain determines the appropriate Reynolds and Mach number ranges based on the blade geometry and operating conditions. The minimum and maximum flow velocities along the blade are computed. The minimum and maximum Reynolds numbers are determined using the minimum and maximum chord lengths. These values are rounded to the nearest 10 000. Finally, a set of five evenly spaced Reynolds numbers is constructed between the minimum and maximum Reynolds numbers. The maximum local Mach number is similarly determined from the maximum flow velocity. This value is rounded to the nearest 0.1 and used to generate a Mach number range from zero to the maximum value in increments of 0.1. This ensures that the aerodynamic polars cover the relevant aerodynamic envelope for the specific case.

XFOIL Parameters
Several XFOIL parameters can be adjusted by the user. These include the N_{crit} parameter, the transition locations on the pressure and suction sides, and the maximum number of iterations allowed [59]. Furthermore, it allows the user to switch between XFOIL boundary layer parameters and BPM's empirical boundary layer parameters.

BPM Parameters
The main input file contains the configuration of the BPM broadband noise model. The user can (de)activate the individual broadband noise source mechanisms described in chapter 2 (i.e. Turbulent Boundary Layer - Trailing Edge noise, Laminar Boundary Layer - Vortex Shedding noise, Trailing Edge Bluntness - Vortex Shedding noise, Separation - Trailing Edge Stall noise, and Tip Vortex Formation noise). The boundary layer trip condition can also be specified.

Results and Validation
Finally, the main input file allows the user to configure the output format of the acoustic results. The sound pressure level spectra generated by the broadband noise models can be specified in one-third octave bands, the standard output format of both the BPM and Gill and Lee models, or in narrowband form. The narrowband option is useful for validation purposes. The experimental spectra are available

in narrowband form. Converting such data to one-third octave bands may obscure spectral details that are relevant for model assessment.

In addition, the plotting of experimental validation data can be enabled or disabled through the input file. Validation datasets corresponding to the acoustics of the scaled propeller and flyover experiments are supported. More information about these validation cases will be provided in chapter 7 and chapter 8.

5.3. Blade Element Momentum Theory

The Blade Element Momentum Theory (BEMT) forms the aerodynamic core of the broadband noise prediction toolchain. The method combines the basic principles from blade element theory and momentum theory. The BEMT analysis used in the toolchain will be described below.

Blade Element Theory

In Blade Element Theory (BET), the propeller blade is divided into several sections, called blade elements [60]. Every element is treated as a two-dimensional airfoil section. The entire blade is then represented as a spanwise distribution of these 2D airfoils. An example of such an airfoil is shown in Figure 5.4. The aerodynamic performance of each section is determined using the relative (or effective) velocity, V_{eff}, and the angle of attack, α, at which this velocity acts [61].

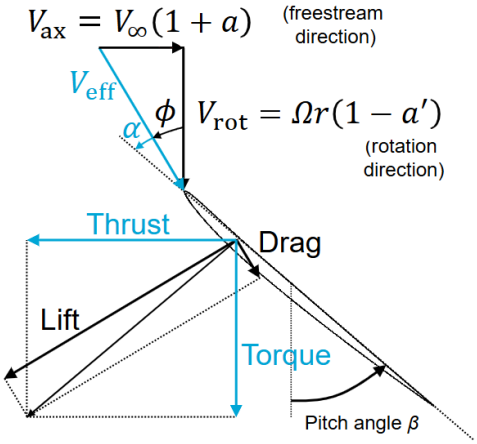

Figure 5.4: Velocity Triangle at a Fixed-Pitch Propeller Blade Section

The relative velocity experienced by a blade element, V_{eff}, can be decomposed into two components: the axial velocity (free-stream direction), V_{ax}, and the rotational/tangential velocity (rotational direction), V_{rot}. The inflow angle, ϕ, can then be expressed as the angle between the relative velocity and the rotational velocity [61], $\phi = \tan^{-1}(\frac{V_{\text{ax}}}{V_{\text{rot}}})$. The blade generates a low-pressure region on one of its surfaces, resulting in a suction force. This force can be decomposed into a lift component, which is perpendicular to V_{eff}, and a drag component, which aligns with V_{eff}. The sectional thrust and torque can then be calculated using Equation 5.1 and Equation 5.2 [60].

$$\frac{\mathrm{d}T}{\mathrm{d}r} = \frac{1}{2}\rho_\infty V_{\text{eff}}^2 \, b_c(c_l \cos\phi - c_d \sin\phi) \tag{5.1}$$

$$\frac{\mathrm{d}Q}{\mathrm{d}r} = \frac{1}{2}\rho_\infty V_1^2 b_c(c_d \cos\phi + c_l \sin\phi)r \tag{5.2}$$

Induced Velocities and Momentum Theory

The effect of the blade on the surrounding flow is introduced through two induction factors: the axial induction factor a and the tangential induction factor a'. These factors modify the local velocity triangle shown in Figure 5.4. They, therefore, change the inflow angle, the angle of attack, and the resulting lift

and drag forces. Because the aerodynamic forces depend on the induced velocities, and these induced velocities depend on the aerodynamic forces, the problem becomes implicit.

Momentum theory can provide the link between the induced velocities and the forces generated by the propeller. In momentum theory, the propeller thrust is evaluated as the time rate of change of momentum of the airflow passing through the rotor disk [62]. It assumes that the flow through the propeller forms a well-defined streamtube. The propeller can then be modelled as an actuator disk, as illustrated in Figure 5.5. Momentum theory further assumes that the pressure and velocity distributions are uniform over the disk surface and that the flow remains incompressible and irrotational [61].

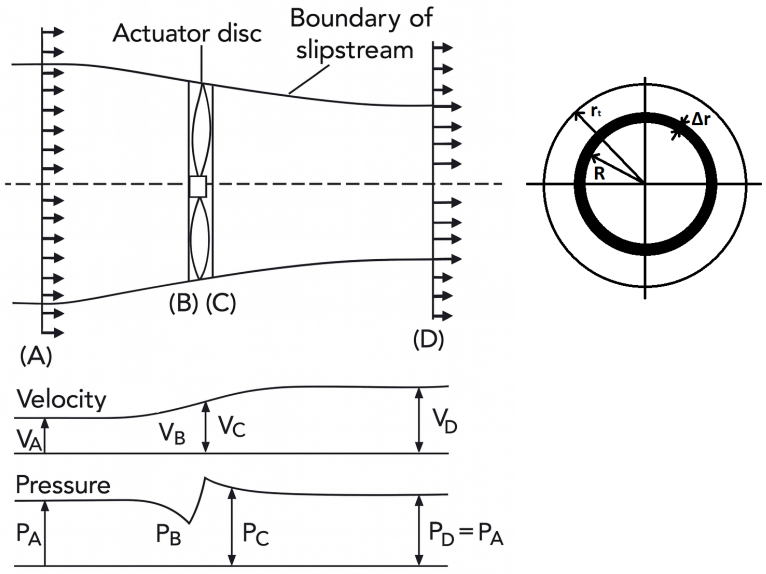

Figure 5.5: Visualisation of the Actuator Disk Theory (adapted from [63])

To apply the momentum relations, the actuator disk is divided into a series of thin radial annuli. They can each be analysed independently since neighbouring rings are assumed not to interact. An annulus at radius R with thickness Δr (see Figure 5.5) has an area $\mathrm{d}A = 2\pi R \Delta r$. The sectional thrust on each annulus can be calculated as the product of the mass flow rate through the annulus and the total change in velocity [62], i.e. $\Delta T = \dot{m}\ (V_D - V_A)$. The mass flow rate passing through the annulus follows directly from its area and local axial velocity, Equation 5.3.

$$\dot{m} = \rho_\infty \, \mathrm{d}A \, V_{\mathrm{ax}} = 2\pi \rho_\infty V_{\mathrm{ax}} R \Delta r \tag{5.3}$$

The axial flow velocity at the disk plane is increased relative to the freestream due to induction, and can therefore be written as $V_x = V_\infty(1 + a)$. The velocity far downstream exceeds the freestream by twice the induced component, $V_D - V_A = 2aV_A = 2aV_\infty$ [64]. Combining these results leads to an expression for the sectional thrust on the annulus, Equation 5.4.

$$\Delta T = \dot{m}\ V_D - V_A = 2\pi \rho_\infty V_x R \Delta r\ V_D - V_A = 4\pi \rho_\infty V_\infty^2 (1 + a) a R \Delta r \tag{5.4}$$

Combining this result with the Blade Element Theory, Equation 5.1 and Equation 5.2, the sectional thrust and torque on an annulus can be determined by creating the equilibria provided in Equation 5.5 and Equation 5.6 [65].

$$\Delta T = 4\pi R_\infty V_\infty^2 (1 + a) a \Delta r = \frac{1}{2} \rho_\infty V_1^2 b_c (c_l \cos\phi - c_d \sin\phi) B \Delta r \tag{5.5}$$

$$\Delta Q = 4\pi r^3 \rho_\infty V_\infty \Omega(1+a)a'\Delta r = \frac{1}{2}\rho_\infty V_1^2 b_c(c_d \cos\phi + c_l \sin\phi)Br\Delta r \tag{5.6}$$

In the toolchain, these equilibria are solved iteratively. This means that the induction factors are first guessed, which, in turn, define the local velocity triangle and the aerodynamic loading. From these loads, the values for a and a' are updated. This process is repeated until the induction factors converge.

Pre-Computed Polar Data
Evaluating the aerodynamic loads on a blade element with XFOIL at every iteration would be computationally expensive. To avoid these repeated external aerodynamic computations, the toolchain relies on pre-computed airfoil polars. These polars are generated once (using XFOIL) over a range of angles of attack of [-10, 10] and a range of Mach numbers and Reynolds numbers (see subsection 5.2.2). During the BEMT analysis, the c_l and c_d values are obtained by interpolating from the pre-computed polars, rather than rerunning XFOIL. For post-stall behaviour, the polars are extended using the Viterna & Corrigan extrapolation [66] to $\alpha = \pm 90°$ [65].

Correction Models
The BEMT solver established in this toolchain incorporates several correction models to improve accuracy beyond the idealised assumptions of the momentum theory. Compressibility effects at higher Mach numbers are taken into account through either the Prandtl-Glauert or Kármán-Tsien correction, depending on the user selection. In addition, Prandtl's root and tip loss correction is applied. For operating conditions where the rotor becomes heavily loaded, the Glauert correction can be included.

Output of the BEMT Solver
Once the induction factors have converged for all radial elements, the performance of the entire propeller is evaluated by integrating the aerodynamic properties of each blade element along the blade radius (r) and multiplying it by the number of propeller blades (N_B) [60]. The integrals used to calculate the total thrust and torque of the propeller can be found in Equation 5.7 and Equation 5.8, respectively [67].

$$T = \rho N_B \int_{hub}^{tip} dT\, dr \tag{5.7}$$

$$Q = \rho N_B \int_{hub}^{tip} dQ\, dr \tag{5.8}$$

In addition to the (sectional) thrust and torque, the solver outputs the thrust coefficient, C_T, and the torque coefficient, C_Q, Equation 5.9 and Equation 5.10, respectively [68][69]. Finally, sectional flow variables, including the local effective velocity and the angle of attack, are exported. The BEMT results form the input to both the GL broadband noise model and the BPM model, which will be discussed in the following sections.

$$C_T = \frac{T}{\rho A\,(\Omega R)^2} \tag{5.9}$$

$$C_Q = \frac{Q}{\rho A\,(\Omega R)^3} \tag{5.10}$$

5.4. Gill and Lee Model Implementation

One of the broadband noise prediction models implemented in this toolchain is the empirical Gill and Lee (GL) model [2]. The model is derived from a dataset covering small drone rotors, medium-sized propellers, and large helicopter rotors. In the following subsections, the spectral formulation and coordinate system used in the GL model will be described.

5.4.1. Spectrum Function Gill and Lee Model

The underlying structure of the one-third octave band expression of the GL model is inspired by the universal wall-pressure spectrum of Lee [41]. The original wall-pressure formulation relies on boundary layer quantities. However, Gill and Lee reformulated the expression to depend solely on rotor performance parameters. This reduces the computational cost compared to conventional boundary layer-dependent prediction models. The resulting spectrum model is provided in Equation 5.11.

$$\mathrm{SPL}_{1/3} = \frac{f_0 \Delta^{0.6}}{[f_3 \Delta^{f_4} + f_5]^{f_6} + [f_7 \Delta]^{f_8}} \tag{5.11}$$

In this formulation, $\Delta = S_t - (f_1 \log_{10}(C_T) + f_2 \log_{10}(\sigma)$, where $S_t = \frac{f c}{V_t}$ is the Strouhal number derived from the solidity-weighted chord length, $c = \frac{\sigma \pi R}{N}$, and the propeller tip velocity, V_t [2]. Parameters f_0 to f_8 are defined through a machine learning process called Gene Expression Programming (GEP). Gene Expression Programming (GEP) is a machine learning method in which candidate mathematical expressions evolve toward an optimal fit to a training dataset [70]. Each candidate is represented as a chromosome consisting of one or more genes. Each gene contains a "head" with mathematical operators and a "tail" with variables or constants. These gene structures allow GEP to construct complex non-linear functions. Through mutation and recombination, the genes progressively evolve towards a solution that best fits the training data. The parameters f_0 to f_8 determined by the GEP are provided in Equation 5.12.

$$
\begin{aligned}
f_0 &= 10 \log_{10} V_t^{7.84} \\
f_1 &= \sigma \\
f_2 &= 0.9 M_t \sigma (M_t + 3.82) \\
f_3 &= 1 \\
f_4 &= 1 \\
f_5 &= -2M_t^2 + 2.06 \\
f_6 &= -C_T M_t (C_T - \sin|\theta_0| + 2.06) + 1 \\
f_7 &= C_T \\
f_8 &= 4.97 C_T \sin|\theta_0| (1.5(s_0/R) M_t - (s_0/R) + 15)
\end{aligned}
\tag{5.12}
$$

One of the inputs for these parameters is the thrust coefficient, C_T. In the broadband noise prediction toolchain, this thrust coefficient is directly obtained from the BEMT analysis described in section 5.3. Other inputs include the blade tip Mach number, M_t, propeller solidity, σ, propeller radius, R, and variables related to the observer's location.

5.4.2. Coordinate System Gill and Lee Model

The observer's relative position is incorporated in the GL model through the elevation angle, θ_0, and the observer distance, s_0. The elevation angle is expressed as the angle between the propeller plane and the line connecting the propeller hub to the observer. $\theta_0 = 0°$ lies in the propeller plane, whereas $\theta_0 = 90°$ corresponds to an observer located directly in front of the propeller (positive z-axis). The distance denotes the straight line separation between the observer and the rotor hub. The coordinate system used to define θ_0 and s_0 is illustrated in Figure 5.6.

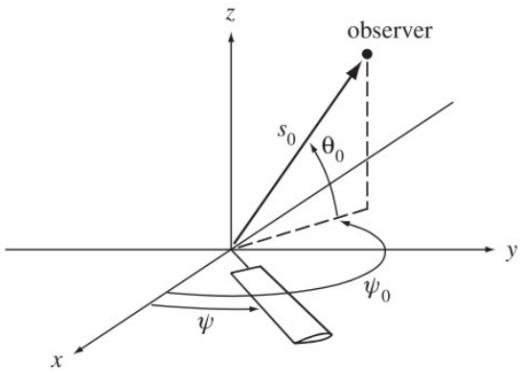

Figure 5.6: Coordinate System GL Model [71]

5.5. Brooks, Pope, and Marcolini Model Implementation

The Brooks, Pope, and Marcolini (BPM) model [1] is the second broadband noise prediction model implemented in the toolchain. It is one of the most widely used semi-empirical approaches for predicting trailing edge noise (self-noise) of the past thirty years [19]. The model is constructed using measurements

of far-field acoustic radiation from NACA 0012 airfoils of various chord lengths, Reynolds numbers, and angles of attack in an anechoic wind tunnel. The measured spectra were then scaled using the formulation of Ffowcs Williams and Hall [25] to produce normalised spectral shapes. From these, correlations for the boundary layer scaling parameters were derived as functions of the operating conditions [24]. The BPM model can be used to predict all individual self-noise components described in section 2.3, namely Turbulent Boundary Layer - Trailing Edge (TBL-TE) noise, Separation - Trailing Edge Stall (S-TES) noise, Trailing Edge Bluntness - Vortex Shedding (TEB-VS) noise, Tip Vortex Formation (TVF) noise, and Laminar Boundary Layer - Vortex Shedding (LBL-VS) noise. Each noise source is characterised by a spectral shape function and scaling parameters obtained from experimental measurements.

5.5.1. Trailing Edge Boundary Layer Parameters

The BPM model requires understanding of the boundary layer thickness, δ, and the boundary layer displacement thickness, δ^*, at the trailing edge. These boundary layer properties govern the spectral scaling. Within the broadband noise prediction framework of this thesis, the boundary layer parameters can be obtained in two ways. The first option is to use the empirical correlations provided by Brooks, Pope, and Marcolini. Secondly, they can be extracted directly from XFOIL for each blade section. Both approaches will be described below.

BPM Empirical Boundary Layer Parameters

Brooks, Pope, and Marcolini provide empirical formulas that estimate the boundary layer properties at the trailing edge directly from the chord Reynolds number, Re_c, and the angle of attack, α_*. These relations were derived by the curve fits to the wind tunnel data [1]. It allows for fast boundary layer estimations based on the NACA0012 airfoil. For an **untripped** boundary layer, the baseline thickness and displacement thickness are given in Equation 5.13 and Equation 5.14. The zero subscripts denote a zero angle of attack and no lift on the airfoils.

$$\frac{\delta_0}{c} = 10^{\left[1.6569 - 0.9045\log(Re_c) + 0.0596\left(\log(Re_c)\right)^2\right]} \tag{5.13}$$

$$\frac{\delta_0^*}{c} = 10^{\left[3.0187 - 1.5397\log(Re_c) + 0.1059\left(\log(Re_c)\right)^2\right]} \tag{5.14}$$

For a **tripped** boundary layer, the displacement thickness is described by the piecewise relation in Equation 5.15. This relation distinguishes between low and high Reynolds number regimes.

$$\frac{\delta_0^*}{c} = \begin{cases} 0.0601 Re_c^{-0.114} & \left(Re_c \leq 0.3 \times 10^6\right) \\ 10^{[3.411 - 1.5397\log(Re_c) + 0.1059(\log(Re_c))^2]} & \left(Re_c > 0.3 \times 10^6\right) \end{cases} \tag{5.15}$$

Both the **untripped** and **tripped** boundary layer on the **pressure side** scales with angle of attack according to the empirical ratios in Equation 5.16 and Equation 5.17.

$$\frac{\delta_p}{\delta_0} = 10^{[-0.04175\alpha_* + 0.00106\alpha_*^2]} \tag{5.16}$$

$$\frac{\delta_p^*}{\delta_0^*} = 10^{[-0.0432\alpha_* + 0.00113\alpha_*^2]} \tag{5.17}$$

On the suction side, the displacement thickness varies between tripped and untripped configurations. For the **untripped suction side** boundary layer, the scaling relations are given in Equation 5.18.

$$\frac{\delta_s^*}{\delta_0^*} = \begin{cases} 10^{0.0679\alpha_*} & \left(0° \leq \alpha_* \leq 7.5°\right) \\ 0.0162\left(10^{0.3066\alpha_*}\right) & \left(7.5° < \alpha_* \leq 12.5°\right) \\ 52.42\left(10^{0.0258\alpha_*}\right) & \left(12.5° < \alpha_* \leq 25°\right) \end{cases} \tag{5.18}$$

For the **tripped suction side** boundary layer, BPM propose the relations given in Equation 5.19.

$$\frac{\delta_s^*}{\delta_0^*} = \begin{cases} 10^{0.0679\alpha_*} & (0° \leq \alpha_* \leq 5°) \\ 0.381\left(10^{0.1516\alpha_*}\right) & (5° < \alpha_* \leq 12.5°) \\ 14.296\left(10^{0.0258\alpha_*}\right) & (12.5° < \alpha_* \leq 25°) \end{cases} \tag{5.19}$$

XFOIL Boundary Layer Parameters
Alternatively, using the angle of attack and effective velocity computed from the BEMT analysis, XFOIL can be run for each blade section to obtain the required boundary layer characteristics. The boundary layer (displacement) thicknesses are extracted at 95% of the chord. XFOIL captures the airfoil-specific effect, such as camber, Reynolds number variation and local flow conditions [59]. As a result, it generally provides more physically representative boundary layer estimates than the empirical BPM correlations, which were originally derived for the NACA 0012 airfoil and may not accurately reflect the behaviour of airfoils with different geometries. The main drawback is computational cost, as XFOIL must be executed for every blade element. This makes it computationally more expensive than using the empirical relations.

5.5.2. Implementation of the Broadband Noise Source Mechanisms

The BPM model represents broadband noise as the sum of several broadband source mechanisms. Each mechanism is described by its own governing equations, scaling laws, and spectral shape functions [1]. In this subsection, the formulations for the Turbulent Boundary Layer – Trailing Edge (TBL-TE) and Separation – Trailing Edge Stall (S-TES) noise are presented in detail. These two mechanisms serve as representative examples of how the BPM model is implemented in the present framework.

TBL-TE and S-TES Noise
The total Turbulent Boundary Layer – Trailing Edge (TBL-TE) and Separation – Trailing Edge Stall (S-TES) noise spectrum in a one-third octave band is obtained by combining the pressure side, suction side, and separation contributions. This overall level is computed using the logarithmic sum shown in Equation 5.20 [1][72].

$$SPL_{TOT} = 10\log\left(10^{SPL_p/10} + 10^{SPL_s/10} + 10^{SPL_a/10}\right) \tag{5.20}$$

The pressure and suction side components of the TBL-TE noise follow the formulations given in Equation 5.21 and Equation 5.22, respectively. In these equations, δ^* denotes the boundary layer displacement thickness, L is the span of the element, M is the local Mach number, and r_{obs} is the observer distance. The two directivity functions, $\bar{D}_h$ and $\bar{D}_l$ will be given in subsection 5.5.3.

$$SPL_p = 10\log\left(\frac{\delta_p^* M^5 L \bar{D}_h}{r_{obs}^2}\right) + A\left(\frac{St_p}{St_1}\right) + (K_1 - 3) + \Delta K_1 \tag{5.21}$$

$$SPL_s = 10\log\left(\frac{\delta_s^* M^5 L \bar{D}_h}{r_{obs}^2}\right) + A\left(\frac{St_s}{St_1}\right) + (K_1 - 3) \tag{5.22}$$

The separation noise contribution is defined as Equation 5.23.

$$SPL_a = 10\log\left(\frac{\delta_s^* M^5 L \bar{D}_h}{r_{obs}^2}\right) + B\left(\frac{St_s}{St_2}\right) + K_2 \tag{5.23}$$

When the airfoil approaches stall, separation noise dominates over boundary layer trailing edge noise. In particular, if either condition

$$\alpha_* > 12.5^\circ \quad \text{or} \quad \alpha_* > \gamma_0$$

is satisfied, only the separation component is retained. In this stall-dominated regime, the TBL-TE contributions are set to $-\infty$ as shown in Equation 5.24 and Equation 5.25. Furthermore, the modified separation expression in Equation 5.26 is used, where A' represents the spectral shape function A evaluated at a value of Re_c that is three times the actual value [1].

$$SPL_p = -\infty \tag{5.24}$$

$$SPL_s = -\infty \tag{5.25}$$

$$SPL_a = 10\log\left(\frac{\delta_s^* M^5 L \bar{D}_l}{r_{obs}^2}\right) + A'\left(\frac{St_s}{St_2}\right) + K_2 \tag{5.26}$$

To evaluate the spectral shape functions A and B, the Strouhal numbers corresponding to the pressure side and suction side boundary layers are defined in Equation 5.27 and Equation 5.28, respectively. The other Strouhal definitions are given in Equation 5.29, Equation 5.30, and Equation 5.31.

$$St_p = \frac{f\delta_p^*}{V} \tag{5.27}$$

$$St_s = \frac{f\delta_s^*}{V} \tag{5.28}$$

$$St_1 = 0.02M^{-0.6} \tag{5.29}$$

$$St_2 = St_1 \times \begin{cases} 1 & (\alpha_* < 1.33^\circ) \\ 10^{0.0054(\alpha_* - 1.33)^2} & (1.33^\circ \leq \alpha_* \leq 12.5^\circ) \\ 4.72 & (\alpha_* > 12.5^\circ) \end{cases} \tag{5.30}$$

$$\overline{St_1} = \frac{St_1 + St_2}{2} \tag{5.31}$$

The spectral shape functions A and B are constructed by interpolating between the minimum and maximum envelopes, as defined in Equation 5.32 and Equation 5.33.

$$A(a) = A_{\min}(a) + A_R(a_0)[A_{\max}(a) - A_{\min}(a)] \tag{5.32}$$

$$B(b) = B_{\min}(b) + B_R(b_0)[B_{\max}(b) - B_{\min}(b)] \tag{5.33}$$

The interpolation limits for A are given in Equation 5.34 and Equation 5.35.

$$A_{\min}(a) = \begin{cases} \sqrt{67.552 - 886.788a^2} - 8.219 & (a < 0.204) \\ -32.665a + 3.981 & (0.204 \leq a \leq 0.244) \\ -142.795a^3 + 103.656a^2 - 57.757a + 6.006 & (a > 0.244) \end{cases} \tag{5.34}$$

$$A_{\max}(a) = \begin{cases} \sqrt{67.552 - 886.788a^2} - 8.219 & (a < 0.13) \\ -15.901a + 1.098 & (0.13 \leq a \leq 0.321) \\ -4.669a^3 + 3.491a^2 - 16.699a + 1.149 & (a > 0.321) \end{cases} \tag{5.35}$$

The auxiliary variable a represents the absolute value of the logarithm of the ratio between the Strouhal number to the peak Strouhal number, Equation 5.36.

$$a = |\log(St/St_{\text{peak}})| \tag{5.36}$$

The interpolation factor A_R is defined in Equation 5.37 and scales the spectral envelope between its minimum and maximum bounds.

$$A_R(a_0) = \frac{-20 - A_{\min}(a_0)}{A_{\max}(a_0) - A_{\min}(a_0)} \tag{5.37}$$

The reference value a_0, which governs the interpolation level for A, depends on the Reynolds number, as given in Equation 5.38.

$$a_0(Re_c) = \begin{cases} 0.57 & (Re_c < 9.52 \times 10^4) \\ (-9.57 \times 10^{-13})(Re_c - 8.57 \times 10^5)^2 + 1.13 & (9.52 \times 10^4 \leq Re_c \leq 8.57 \times 10^5) \\ 1.13 & (Re_c > 8.57 \times 10^5) \end{cases} \tag{5.38}$$

Similarly, the spectral interpolation for the spectral shape function B uses bounding curves $B_{\min}$ and $B_{\max}$, given in Equation 5.39 and Equation 5.40.

$$B_{\min}(b) = \begin{cases} \sqrt{16.888 - 886.788b^2} - 4.109 & (b < 0.13) \\ -83.607b + 8.138 & (0.13 \leq b \leq 0.145) \\ -817.810b^3 + 355.210b^2 - 135.024b + 10.619 & (b > 0.145) \end{cases} \tag{5.39}$$

$$B_{\max}(b) = \begin{cases} \sqrt{16.888 - 886.788b^2} - 4.109 & (b < 0.10) \\ -31.330b + 1.854 & (0.10 \leq b \leq 0.187) \\ -80.541b^3 + 44.174b^2 - 39.381b + 2.344 & (b > 0.187) \end{cases} \tag{5.40}$$

The argument b is defined in Equation 5.41.

$$b = |\log(St_s/St_2)| \tag{5.41}$$

The corresponding interpolation coefficient B_R, comparable to A_R, is defined in Equation 5.42.

$$B_R(b_0) = \frac{-20 - B_{\min}(b_0)}{B_{\max}(b_0) - B_{\min}(b_0)} \tag{5.42}$$

The reference value b_0, which selects the interpolation level for the separation spectral model, is determined from the Reynolds number using Equation 5.43.

$$b_0(Re_c) = \begin{cases} 0.30 & (Re_c < 9.52 \times 10^4) \\ (-4.48 \times 10^{-13})(Re_c - 8.57 \times 10^5)^2 + 0.56 & (9.52 \times 10^4 \leq Re_c \leq 8.57 \times 10^5) \\ 0.56 & (Re_c > 8.57 \times 10^5) \end{cases} \tag{5.43}$$

The amplitude function K_1, which appears in both pressure side and suction side TBL-TE noise components, also depends on Reynolds number as shown in Equation 5.44.

$$K_1 = \begin{cases} -4.31\log(Re_c) + 156.3 & (Re_c < 2.47\times10^5) \\ -9.0\log(Re_c) + 181.6 & (2.47\times10^5 \le Re_c \le 8.0\times10^5) \\ 128.5 & (Re_c > 8.0\times10^5) \end{cases} \tag{5.44}$$

A correction ΔK_1 is added for the pressure side contribution when the displacement thickness Reynolds number, $Re_{d_p^*}$, is small. This correction is defined in Equation 5.45.

$$\Delta K_1 = \begin{cases} \alpha_*[1.43\log(Re_{d_p^*}) - 5.29] & (Re_{d_p^*} \le 5000) \\ 0 & (Re_{d_p^*} > 5000) \end{cases} \tag{5.45}$$

The amplitude function K_2, used exclusively in the separation noise, modifies K_1 based on the effective angle of attack relative to a stall threshold. Its definition is given in Equation 5.46.

$$K_2 = K_1 + \begin{cases} -1000 & (\alpha_* < \gamma_0 - \gamma) \\ \sqrt{\beta^2 - (\beta/\gamma)^2(\alpha_* - \gamma_0)^2} + \beta_0 & (\gamma_0 - \gamma \le \alpha_* \le \gamma_0 + \gamma) \\ -12 & (\alpha_* > \gamma_0 + \gamma) \end{cases} \tag{5.46}$$

The parameters γ, γ_0, β, and β_0 depend only on Mach number and are given in Equation 5.47.

$$\left.\begin{aligned} \gamma &= 27.094M + 3.31 & \gamma_0 &= 23.43M + 4.651 \\ \beta &= 72.65M + 10.74 & \beta_0 &= -34.19M - 13.82 \end{aligned}\right\} \tag{5.47}$$

Other Broadband Noise Sources and Total Broadband Noise

In addition to TBL-TE and S-TES noise, the BPM model includes several other broadband source components. The complete formulations for these self-noise mechanisms are provided in the original work of Brooks, Pope, and Marcolini [1] and are not reproduced here for brevity. In the current implementation, these components are evaluated based on the published correlations. They can be added to the TBL-TE and S-TES contributions to obtain the total broadband noise level for each blade element. The individual spectra are combined through logarithmic summation across all active source mechanisms to form the full BPM broadband noise prediction.

5.5.3. Geometric Framework for BPM in Rotating Propellers

The BPM model is formulated for a stationary three-dimensional airfoil segment. When applied to a rotating propeller blade, however, the orientation of each blade element continuously changes relative to the observer. As a result, the directivity angles and observer distance vary with azimuth. This requires a geometric framework that maps the blade kinematics into the global coordinate system [73]. This subsection will describe the coordinate frame used, the definition of the directivity angles, and the procedures for azimuthal averaging and spanwise integration.

Blade Segment Directivity Angles and Functions

The BPM model includes directional corrections for each broadband noise mechanism (see subsection 5.5.2). These corrections are formulated in terms of the spherical angles Θ and Φ (see Figure 5.7). The directivity function for high frequencies, Equation 5.48, is used for all source mechanisms with the exception of the stall regime. In this case, the low-frequency directivity function, Equation 5.49, is used.

$$\overline{D}_h(\Theta_e, \Phi_e) \approx \frac{2\sin^2(\Theta_e/2)\sin^2\Phi_e}{(1 + M\cos\Theta_e)\left[1 + (M - M_c)\cos\Theta_e\right]^2} \tag{5.48}$$

$$\overline{D}_\ell(\Theta_e, \Phi_e) \approx \frac{\sin^2(\Theta_e/2)\sin^2\Phi_e}{(1 + M\cos\Theta_e)^4} \tag{5.49}$$

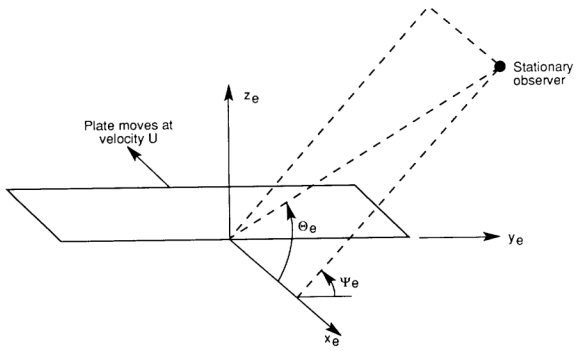

Figure 5.7: Nomenclature BPM Angles in Directivity Functions [1]

Propeller Coordinate Frame and Observer Transformation

All geometric quantities are expressed in a right-handed coordinate system with its origin at the propeller hub. When standing in front of the propeller, the x-axis points to the right, the y-axis upward, and the z-axis toward the observer, normal to the propeller disk (see Figure 5.8). The observer location is specified by the user in this hub-fixed frame.

To evaluate the BPM directivity functions for a rotating blade, the observer position relative to the blade's segment must be determined. In this thesis, three different coordinate transformations were implemented. The first transformation follows the formulation of Vargas [72] and assumes that the blade section is not rotated about its pitch axis. This transformation forms the baseline implementation and is illustrated in Figure 5.9. A second transformation extends this formulation by explicitly including blade pitch. The sensitivity of the broadband noise prediction to the assumption of not including blade pitch in the coordinate transformation will be assessed in chapter 7. Finally, a third transformation based on the formulation of Lee and Li [52] is implemented to validate the pitch-inclusive transformation developed in this thesis.

Coordinate transformation no blade pitch (cs:1)

For a blade element at radial position, r, and azimuthal angle, ψ, the trailing edge coordinates follow from the chord geometry, Equation 5.50 and Equation 5.51. In these equations, $c_2 = c - c_1$ denotes the trailing edge offset and c_1 is the distance from the leading edge to the pitch axis (assumed to be $0.25c$) [72].

$$x_s = \sin\psi\, r - \cos\beta\, c_2 \tag{5.50}$$

$$y_s = \cos\psi\, r + \sin\beta\, c_2 \tag{5.51}$$

The observer position (x_o, y_o, z_o) is then expressed relative to this trailing edge point, Equation 5.52 and Equation 5.53.

$$x'_e = x_o - x_s \tag{5.52}$$

$$y'_e = y_o - y_s \tag{5.53}$$

To align the coordinate system with the BPM formulation for a stationary airfoil segment, Figure 5.7, this vector is rotated about the local z-axis by $\theta = \pi - \psi$, Equation 5.54 and Equation 5.55.

$$x_e = \cos\theta\, x'_e + \sin\theta\, y'_e, \tag{5.54}$$

$$y_e = -\sin\theta\, x'_e + \cos\theta\, y'_e. \tag{5.55}$$

This yields the relative observer vector, Equation 5.56. The distance and directivity angles required by BPM then follow from Equation 5.57, Equation 5.58, and Equation 5.59. It should be noted that an important limitation of this coordinate transformation is that it assumes that the propeller blade is not rotated about its pitch axis [72].

$$\mathbf{r}_e = (x_e,\, y_e,\, z_o) \tag{5.56}$$

$$r_{obs} = \|\mathbf{r}_e\| \tag{5.57}$$

$$\Theta_e = \arctan\left(\frac{\sqrt{y_e^2 + z_o^2}}{x_e}\right) \tag{5.58}$$

$$\Phi_e = \arctan\left(\frac{z_o}{y_e}\right) \tag{5.59}$$

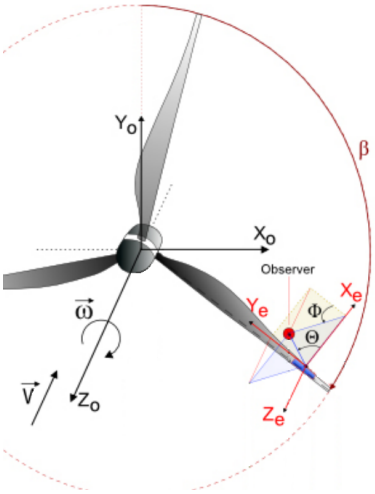

Figure 5.8: Propeller Coordinate System (adapted from [72])

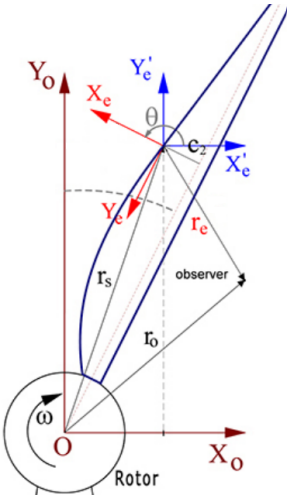

Figure 5.9: Coordinate System Transformation (adapted from [72])

Coordinate transformation inclusion of blade pitch (cs:2)
The second coordinate transformation extends the baseline formulation by explicitly including the blade pitch angle, β. In contrast to cs:1, the blade element is no longer assumed to lie entirely in the propeller disk plane. The trailing edge position is first defined without the chord-wise offset in the propeller disk plane. The trailing edge coordinates given in Equation 5.50 and Equation 5.51 therefore become Equation 5.60 and Equation 5.61, respectively.

$$x_s = \sin\psi\, r \tag{5.60}$$

$$y_s = \cos\psi\, r \tag{5.61}$$

The observer position relative to the trailing edge is subsequently defined as before, Equation 5.52 and Equation 5.53. As in cs:1, the observer vector is first rotated about the z-axis to account for blade azimuth. To account for blade pitch, this intermediate observer vector, $\vec{r_E}$, is subsequently rotated about the local pitch axis by the pitch angle, β. This additional rotation yields the final observer coordinates, as shown in Equation 5.62.

$$\vec{r}_e = \begin{bmatrix} \cos(\beta) & 0 & -\sin(\beta) \\ 0 & 1 & 0 \\ \sin(\beta) & 0 & \cos(\beta) \end{bmatrix} \cdot \vec{r}_E + \begin{bmatrix} c_2 \cos(\beta) \\ 0 \\ 0 \end{bmatrix} \tag{5.62}$$

Again, the distance and directivity angles required by BPM follow from Equation 5.57, Equation 5.58, and Equation 5.59, respectively.

Coordinate transformation by Lee and Li (cs:3)
The third coordinate transformation implemented in this work follows the formulation proposed by Li and Lee [52], as given in Equation 5.63. This formulation simultaneously accounts for the blade azimuth angle ψ and the blade pitch angle β within a single transformation matrix [73]. The translation term shifts the coordinate system from the propeller hub to the local blade element at radial position r.

$$\begin{bmatrix} x_e \\ y_e \\ z_e \end{bmatrix} = \begin{bmatrix} \sin\psi\cos\beta & -\cos\psi\cos\beta & -\sin\beta \\ \cos\psi & \sin\psi & 0 \\ \sin\psi\sin\beta & -\cos\psi\sin\beta & \cos\beta \end{bmatrix} \begin{bmatrix} X \\ Y \\ Z \end{bmatrix} + \begin{bmatrix} 0 \\ -r \\ 0 \end{bmatrix} \tag{5.63}$$

Spanwise Integration
As mentioned before, each propeller blade is discretised into multiple radial elements. Each section is treated as an independent contributor to the BPM noise prediction. For a given azimuthal position, the broadband noise spectrum is first evaluated for each blade element. After evaluating the BPM model for all radial elements at a fixed azimuth, the acoustic contributions are summed in a linear pressure scale. This spanwise integration yields the broadband noise spectrum of a single blade at that specific azimuthal position.

Azimuthal Integration of a Blade
While the aerodynamic and boundary layer properties of each blade element (obtained from either BEMT or the empirical BPM formulas) are assumed to remain constant over one revolution, the relative orientation of the blade with respect to the observer changes continuously. To account for this effect, the blade azimuth angle is discretised into 36 equally spaced positions,

$$\beta \in \{0^\circ, 10^\circ, 20^\circ, \ldots, 350^\circ\}.$$

For each azimuthal position, the observer transformation is applied, the BPM model is evaluated for all blade elements, and the spanwise integration is performed to obtain the broadband noise spectrum of a single blade at that azimuth. Repeating this procedure for all azimuth angles yields a set of blade-level noise spectra corresponding to different blade orientations. The broadband noise contribution of a single blade is then obtained by averaging the spectra over all azimuthal positions. This azimuthal averaging ensures that the predicted noise represents the time-averaged broadband radiation of a rotating blade, rather than a snapshot associated with a particular blade orientation. Finally, the total broadband noise spectrum of the propeller is obtained by logarithmically summing the contributions of all blades, as given in Equation 5.64.

$$\mathrm{SPL}_{\mathrm{tot}} = 10\log_{10}\left(\sum_{b=1}^{N_b} 10^{\mathrm{SPL}_b/10}\right) \tag{5.64}$$

6

Verification of the Broadband Noise Models

In this chapter, the implementation of the broadband noise models employed in this thesis will be verified against the original formulations reported in the literature. The objective of this verification is to demonstrate that the implemented models reproduce the published results when identical input parameters are used. This verification step is important to establish confidence in the correctness of the implementation.

6.1. Verification Gill and Lee Model Implementation

The Gill and Lee model predicts the broadband noise generated by a rotating propeller. As such, the verification of this model is performed at the propeller level rather than for an isolated blade or airfoil section. Figure 6.1 presents a comparison between the reference results reported by Gill and Lee [2] and the output obtained using the implementation developed in this thesis. The same propeller performance parameters and operating conditions as reported in the original work were used. These are provided in Table 6.1.

Table 6.1: Propeller Performance Parameters and Operating Conditions to verify the GL Model Implementation

Propeller	Blade Number	RPM	Radius [m]	M_t	C_T	Solidity	s_0 [m]	θ_0 [°]
COPR-5 [74]	5	4782	0.3048	0.45	0.0342	0.255	6.583	-57.5

Figure 6.1 demonstrates that the predicted sound pressure level spectra closely match the reference results across the full frequency range. This confirms the correctness of the Gill and Lee model implementation and its suitability for subsequent use within the broadband noise prediction toolchain.

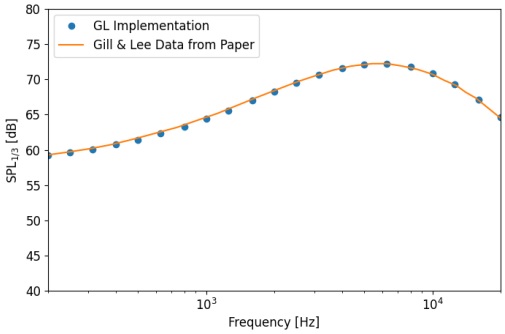

Figure 6.1: Verification of the GL Model Implementation

6.2. Verification Brooks, Pope, and Marcolini Model Implementation

The Brooks, Pope, and Marcolini (BPM) model was originally developed to predict broadband noise generated by stationary airfoil sections. Consequently, the BPM model implementation is verified for a non-rotating airfoil configuration, consistent with the original formulation. For the verification, the model is thus not yet embedded within the rotating propeller framework described in chapter 5. This separation ensures that the verification focuses solely on the correctness of the BPM source models themselves, independent of any coordinate transformations.

Turbulent Boundary Layer - Trailing Edge, Separation - Trailing Edge Stall, and Laminar Boundary Layer - Vortex Shedding Noise

The verification of the Turbulent Boundary Layer - Trailing Edge (TBL-TE), Separation - Trailing Edge Stall (S-TES), and Laminar Boundary Layer - Vortex Shedding (LBL-VS) noise mechanisms is presented in Figure 6.2. In this figure, the crosses indicate the results presented by Brooks, Pope, and Marcolini [1]. The other symbols, on the other hand, show the corresponding predictions obtained with the present implementation. The airfoil parameters and operating conditions used for this verification are provided in Table 6.2.

Table 6.2: Airfoil Parameters and Operating Conditions to verify the BPM TBL-TE, S-TES, and LBL-VS Implementation

Airfoil	Span [m]	c [m]	Θ [°]	Φ [°]	r_e [m]	α_* [°]	V_{eff} [m/s]
NACA 0012	0.4572	0.3048	90.0	90.0	1.22	1.516	71.3

As shown in Figure 6.2, the implemented model accurately reproduces the spectral sound pressure levels reported in the original work. The contribution of the different self-noise sources to the total broadband noise prediction is consistent with the reference results. This agreement confirms the correct implementation of the BPM formulations for the three broadband noise sources.

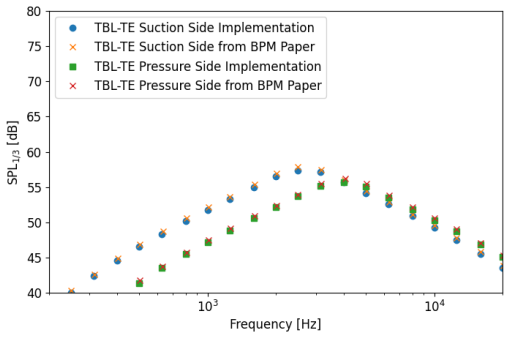

(a) TBL-TE

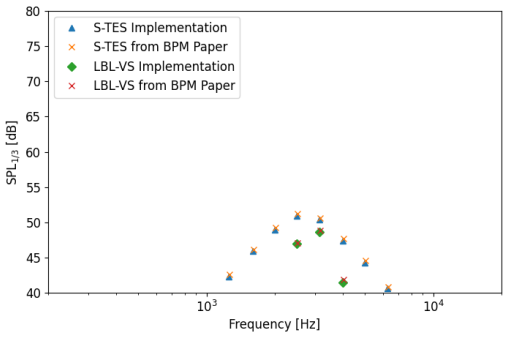

(b) S-TES and LBL-VS

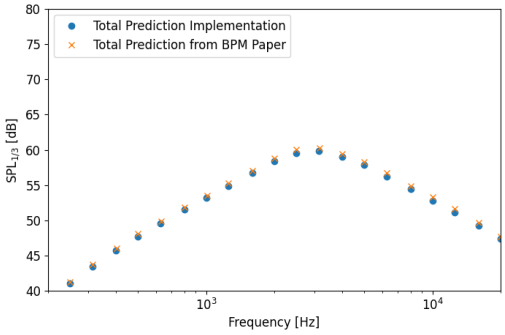

(c) Total Noise Prediction (i.e. Logarithmic Sum of TBL-TE, S-TES, and LBL-VS)

Figure 6.2: TBL-TE, S-TES, and LBL-VS Noise Verification

Trailing Edge Bluntness - Vortex Shedding Noise

The verification of the Trailing Edge Bluntness - Vortex Shedding (TEB-VS) noise is presented in Figure 6.3. The airfoil parameters and operating conditions used for the verification of TEB-VS are summarised in Table 6.3, where H and ψ_{TE} denote the trailing edge bluntness and trailing edge angle, respectively. The predicted broadband noise source again agrees closely with the published results.

Table 6.3: Airfoil Parameters and Operating Conditions to verify the BPM TEB-VS Implementation

Airfoil	Span [m]	c [m]	Θ [°]	Φ [°]	r_e [m]	α_* [°]	V_{eff} [m/s]	H [mm]	ψ_{TE} [°]
NACA 0012	0.533	0.229	90.0	90.0	2.81	0.0	105.5	0.63	23.0

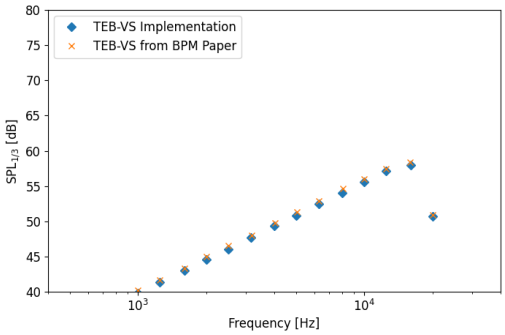

Figure 6.3: TEB-VS Noise Verification

Tip Vortex Formation Noise

Finally, the verification of the Tip Vortex Formation (TVF) noise is presented in Figure 6.4. Note that the total prediction in Figure 6.4 corresponds to the logarithmic sum of TBL-TE, S-TES, and TVF noise for a tripped boundary layer. The airfoil parameters and operating conditions used for the verification of TVF are provided in Table 6.4, where α_{tip} is the tip angle of attack.

Table 6.4: Airfoil Parameters and Operating Conditions to verify BPM TVF Implementation

Airfoil	Span [m]	c [m]	Θ [°]	Φ [°]	r_e [m]	α_* [°]	V_{eff} [m/s]	α_{tip} [°]
NACA 0012	0.3048	0.1524	90.0	90.0	1.22	5.4	71.3	10.8

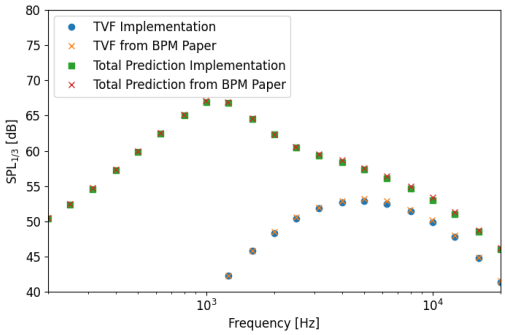

Figure 6.4: TVF Noise Verification

Overall, the results presented in this chapter demonstrate that both the Gill and Lee and the Brooks, Pope, and Marcolini broadband noise models have been implemented correctly. The close agreement with the original reference results provides a solid foundation for applying these models to rotating propeller configurations and experimental validation cases in the following chapters.

7

Validation of the Blade Element Momentum Theory Solver and the Broadband Noise Models

This chapter will present the validation of the aerodynamic and acoustic modules of the broadband noise prediction toolchain. The validation process considers both the implemented Blade Element Momentum Theory (BEMT) solver and the two broadband noise prediction models, namely the Brooks, Pope, and Marcolini (BPM) model and the Gill and Lee (GL) model. Model predictions are compared against two independent experimental data sets: (I) the hover performance and acoustic measurements of a geometrically scaled propeller obtained by Tinney and Valdez [69], and (II) full-scale flyover measurements of a single-propeller fully electric aircraft. For the following comparisons between different models, the coordinate transformation including blade pitch (cs:2) was used for BPM (see subsection 5.5.3).

7.1. Validation Case I: Hover Performance and Acoustics of Scaled Propeller

The first validation case concerns the hover experiment of a scaled model of an eVTOL propeller. The rotor performance and noise measurements of this propeller are available under well-defined operating conditions [69][75][76]. The case, therefore, serves as a basis for validating both the BEMT aerodynamic predictions and the broadband noise models in a rotating propeller setting.

7.1.1. Case Description

Tinney and Valdez [69] conducted a combined aerodynamic and acoustic study on a 35% scaled replica of the Joby Aviation rotor. The model consisted of five blades with a diameter of $D = 1.015$ [m] and a maximum chord of $c_{max} = 83.76$ [mm] at $r/R = 0.40$, where R denotes the rotor radius. Hover performance measurements were obtained for rotational speeds of 30 [rps] and 35 [rps] across several blade pitch angles.

The experiment was conducted in the Gas Dynamics Laboratory at the Applied Research Laboratories of the University of Texas at Austin. The facility operated at near standard atmospheric conditions, summarised in Table 7.1. The sound field was captured using a vertical array of 12 G.R.A.S. free-field microphones. Data was recorded continuously over a 20.48 [s] interval using a 50 [kHz] sampling rate. The microphones were arranged such that the fourth microphone (measured from the facility floor) was located in the propeller disk plane [76]. The array was traversed radially in increments of $\delta r/D = 0.5$ over $1.0 \leq r/D \leq 3.5$ to construct a two-dimensional map of the acoustic field, as shown in Figure 7.1.

Table 7.1: Operating Conditions of the Hover Performance and Acoustics Experiments

Condition	Value	Unit
Temperature	294	[K]
Pressure	103 325	[Pa]
Density	1.2008	[kg/m^3]
Speed of Sound	343.81	[m/s]

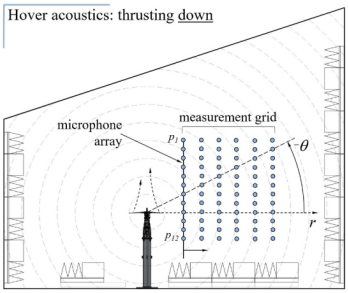

Figure 7.1: Rotor and Microphone Setup for Acoustic Measurements [69]

7.1.2. Blade Element Momentum Theory Validation - Scaled Propeller

Figure 7.2 compares the thrust coefficient, C_T, predicted by the BEMT solver with the hover measurements of Tinney and Valdez [69]. A consistent overprediction of C_T is observed across all pitch settings. This behaviour is also reflected in the predictions of total thrust (Figure 7.3) and torque (Figure 7.4). For torque, good agreement with the measurements is obtained at low pitch angles, while the overprediction increases with increasing pitch.

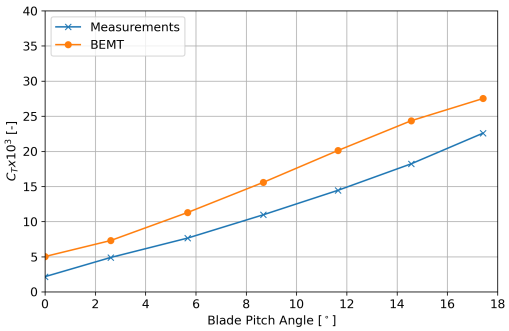

Figure 7.2: Comparison of Thrust Coefficient (C_T) between BEMT Solver Predictions and Experimental Data from Tinney and Valdez [69]

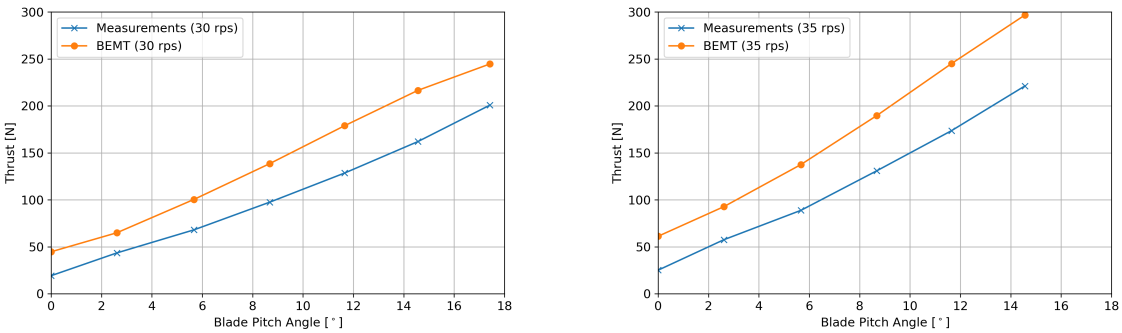

(a) 30 [rps] **(b)** 35 [rps]

Figure 7.3: Comparison of Total Thrust between BEMT Solver Predictions and Experimental Data from Tinney and Valdez [69] for 30 [rps] and 35 [rps]

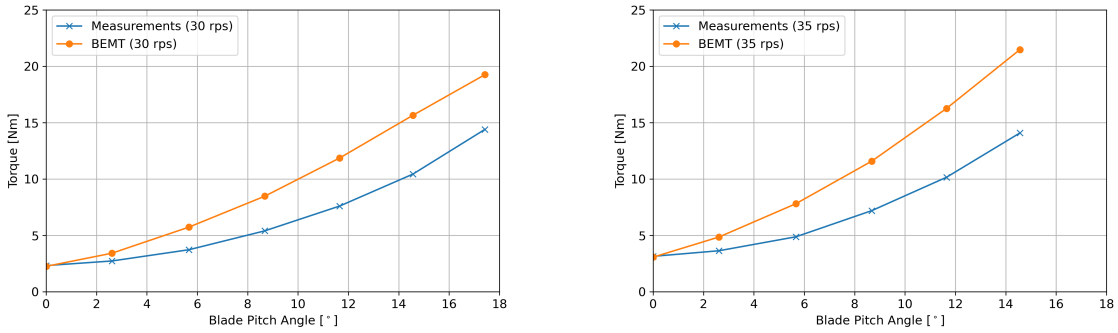

(a) 30 [rps] **(b)** 35 [rps]

Figure 7.4: Comparison of Total Torque between BEMT Solver Predictions and Experimental Data from Tinney and Valdez [69] for 30 [rps] and 35 [rps]

Despite this offset, the trends and overall variation in thrust and torque with pitch are well reproduced. This indicates that the implemented BEMT formulation captures the rotor's dominant aerodynamic behaviour. The overprediction aligns with known limitations of classical BEMT. For example, Boatto et al. [77] demonstrated that the Prandtl tip-loss correction (implemented in the BEMT solver) provides 5% to 15% higher loading in comparison with RANS CFD simulations. As previously mentioned in section 5.4, the thrust coefficient serves as one of the inputs to the Gill and Lee model. The influence of the overprediction observed in the BEMT solver on the broadband prediction was therefore investigated. Figure 7.5 shows the predicted broadband noise levels for the hover validation case with the microphone positioning and the operating conditions elaborated on below. The dashed line uses the thrust coefficients as obtained from the experiment, whereas the straight line uses the thrust coefficient obtained from the BEMT solver. It can be observed that overpredicting the thrust coefficient results in only a minimal increase in predicted broadband noise levels and a slight shift in the peak frequency. Therefore, given the correspondence in trends and magnitudes, the BEMT model is considered sufficient for use as aerodynamic input to the broadband noise prediction models.

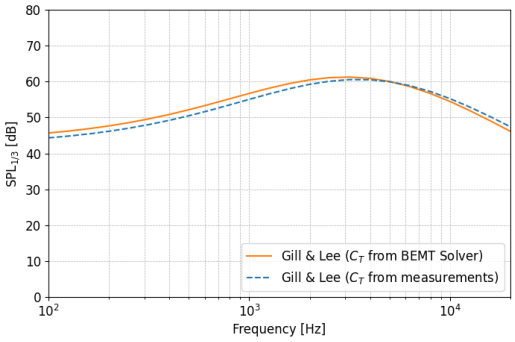

Figure 7.5: Influence of C_T Overprediction by BEMT Solver on Broadband Noise Prediction Levels

7.1.3. Broadband Noise Prediction Validation – Scaled Propeller

A comparison between the measured acoustic data and the broadband noise predictions of the GL and BPM models is presented in Figure 7.6. The predictions were generated for a microphone positioned at $r/D = 2.0$ and an elevation angle $\theta = -45°$ (see Figure 7.1). The rotor was operated at 30 [rps] with a blade pitch setting of 15°. The sound pressure spectrum levels were computed using a Hanning window with $N = 3 \times 2^{13}$ samples per block and 75% overlap, resulting in a frequency resolution of $\delta f = 2.0345$ [Hz] [69].

Figure 7.6a shows the narrowband SPL spectrum obtained from the experiment and the corresponding one-third octave representation. It is important to note that the experimental data contains both tonal

noise and broadband noise components. As expected, conversion to the one-third octave spectrum yields higher SPL values. This is attributed to the accumulation of narrowband energy into wider frequency bins. This observation aligns with comparable results found in the literature by Wu et al. [78].

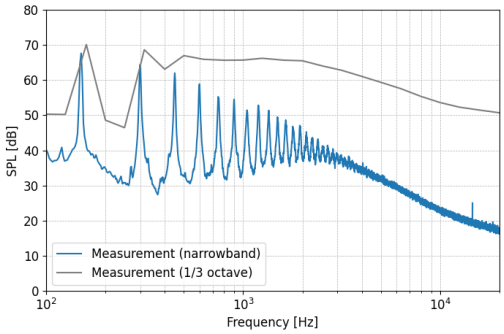

(a) Narrowband vs One-Third Octave Experimental Data

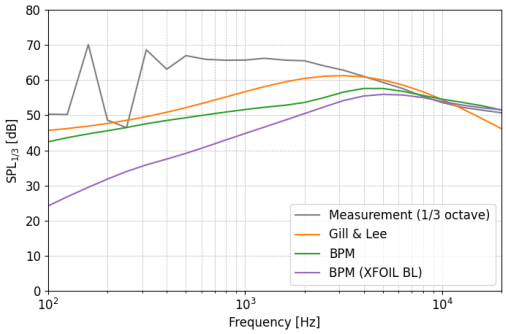

(b) Comparison in the One-Third Octave Domain

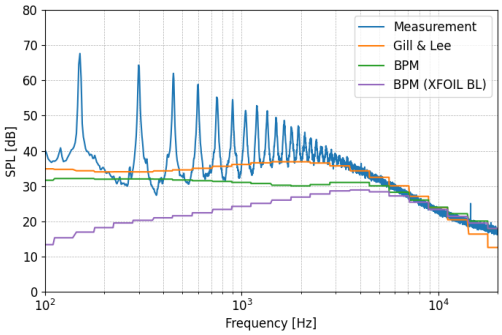

(c) Comparison in the Narrowband Domain

Figure 7.6: Comparison of Measured and Predicted Broadband Noise Spectra for the Scaled Propeller using the BPM and GL Models

Figure 7.6b and Figure 7.6c compare the experimental measurements with predictions from the GL model and the BPM model in both one-third octave and narrowband form. For the BPM model, two variants are shown: one using empirical boundary layer parameters and the other using boundary layer properties estimated with XFOIL (see subsection 5.5.1). All model predictions show good agreement with the measured broadband noise levels in the higher-frequency range where broadband noise dominates. The GL model in particular provides an almost exact match to the experimental data. The narrowband tonal peaks observed in the experimental data correspond to tonal noise, which is not captured by broadband noise models and is therefore expected to be missing from the predictions. Both the GL model and the BPM model using empirical boundary layer parameters intersect the lower envelope of the tonal peaks, as can be noticed in Figure 7.6c.

7.1.4. Directivity and Distance Scaling Analysis - Scaled Propeller

A combined directivity and distance scaling study was performed by evaluating the predicted broadband noise at observer locations distributed around a circular path centred on the rotor, as illustrated in Figure 7.7. The purpose of this analysis is to assess both the angular variation of the predicted sound pressure levels and the (expected) reduction in noise levels across increasing observer radii for the GL and BPM models.

Figure 7.8 presents the influence of the three implemented coordinate transformations (cs:1, cs:2, and cs:3, see subsection 5.5.3) on the BPM model prediction at a radius of 5 [m]. Neglecting blade pitch (cs:1) results in a noticeable dip in sound pressure level in the propeller disk plane (90° and 270°). Incorporating blade pitch through cs:2 and cs:3 yields a smooth directivity pattern. The close agreement between cs:2 and cs:3 supports the validity of the pitch-inclusive transformation introduced in this

thesis. As stated before, for the following comparisons between different models, cs:2 was used for the BPM coordinate transformation (see subsection 5.5.3).

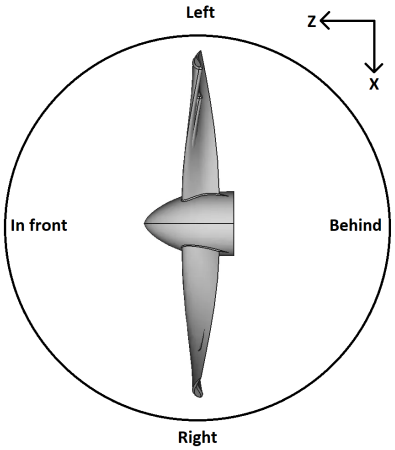

Figure 7.7: Orientation of the Propeller for the Directivity and Distance Scaling Analysis

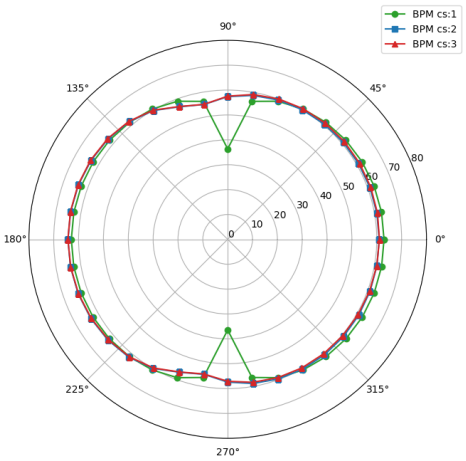

Figure 7.8: Directivity Plot at Radius 5 [m] for Different BPM Coordinate Transformations

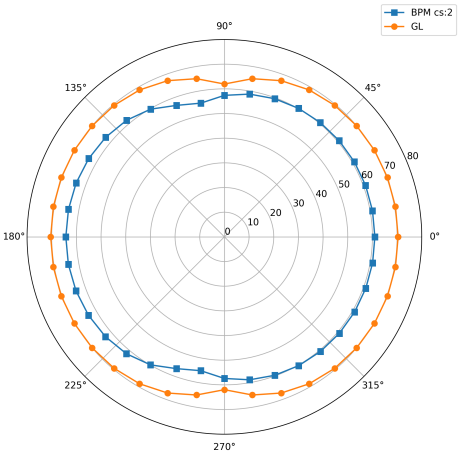

(a) Radius 5 [m] (s_0/R = 9.85)

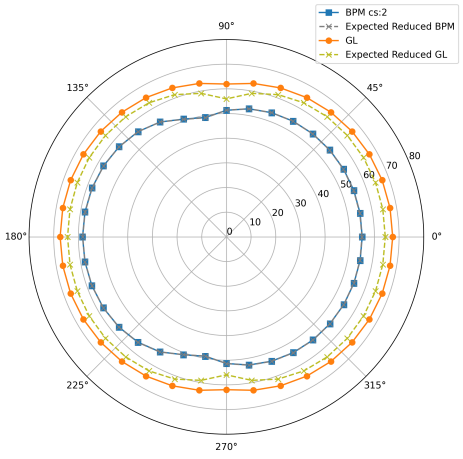

(b) Radius 10 [m] (s_0/R = 19.70)

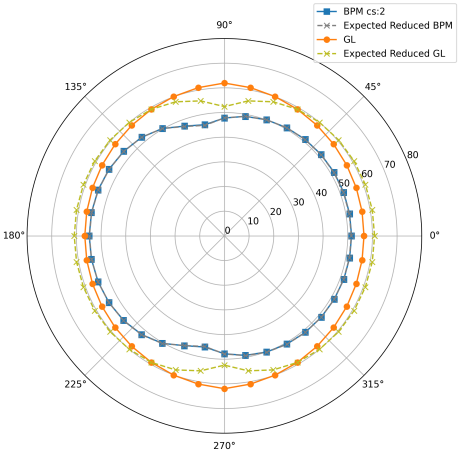

(c) Radius 15 [m] (s_0/R = 29.56)

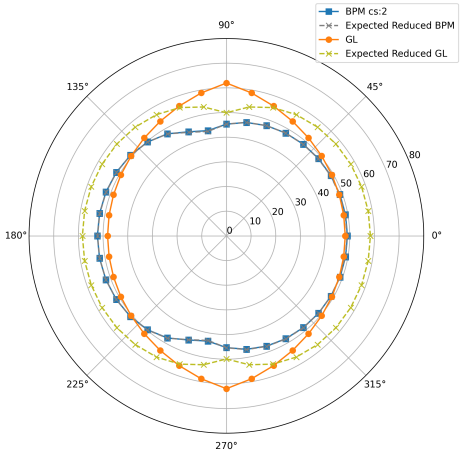

(d) Radius 20 [m] (s_0/R = 39.41)

Figure 7.9: Directivity and Distance Scaling Comparison for Different Observer Radii for Validation Case I

Figure 7.9a presents the directivity pattern at a radius of 5 [m] for both the BPM model and the GL model. Figure 7.9b, Figure 7.9c, and Figure 7.9d show the corresponding predictions at larger observer distances. In these figures, the model predictions are compared against the expected reduction in sound pressure level relative to the 5 [m] case based on spherical spreading. This expected reduction is computed using $20\log(s_0)$. The expected reduction is denoted by dashed lines for both models. For the BPM model, the model predictions and the dashed reference lines overlap. This means that the reduction in sound pressure level with increasing observer distance follows the expected $20\log(s_0)$ trend exactly. It indicates that spherical spreading is correctly captured by the BPM formulation.

For the Gill and Lee model, a reduction in sound pressure level with increasing distance is also observed. However, the scaling deviates from the expected $20\log(s_0)$ behaviour. At a radius of 10 [m], Figure 7.9b, the predicted reduction is smaller than expected. On the other hand, at radii of 15 [m] and 20 [m], the predicted reduction exceeds the spherical spreading trend. This discrepancy becomes increasingly pronounced as one moves from 15 [m] to 20 [m]. A plausible explanation for this behaviour is that the Gill and Lee model was trained using data within the range $5 \leq s_0/R \leq 25$, where s_0/R is the normalised observer distance from the rotor hub. The 15 [m] and 20 [m] cases correspond to $s_0/R = 29.56$ and $s_0/R = 39.41$, respectively, which fall outside the original training domain.

An exception to the distance scaling behaviour occurs for the Gill and Lee model in the propeller disk plane. Here, the predicted sound pressure level remains constant as the observer distance increases. This behaviour follows directly from the model formulation. In Equation 5.12, setting $\theta_0 = 0$ results in $\sin|\theta_0| = 0$. This effectively removes the distance contribution s_0 from the term f_8. Note that $\theta_0 = 0$ in the Gill and Lee coordinate system corresponds to 90° in Figure 7.9, which is the propeller disk plane (see Figure 5.6 and Figure 7.7). This leads to a physically unrealistic lack of sound pressure level decay with distance in these directions.

7.2. Validation Case II: Single-Propeller Fully Electric Aircraft Flyover Experiment (FO1)

The second validation case will assess the predictive performance of the broadband noise models for a full-scale propeller operating in forward flight. This validation case is chosen to complement the hover-based validation of section 7.1.

7.2.1. Case Description

To further assess the broadband noise prediction models, acoustic data from a flyover of a single-propeller fully electric aircraft were used. The aircraft has a three-bladed propeller with a diameter of 1.64 [m]. Additional details regarding the experiment, microphone arrangement, and propeller geometry are provided in the thesis of Elbers [13]. The relevant flight and atmospheric conditions for the flyover case are given in Table 7.2 and Table 7.3, respectively.

Table 7.2: Flight Conditions of the Flyover Experiment [11]

Case	h [m]	V_{inf} [m/s]	RPM	α_{disk} [°]	J
FO1	7.43D	41.7091	2500	0.0	0.6055

Table 7.3: Operating Conditions of the Flyover Experiment [13]

Condition	Value	Unit
Temperature	292.65	[K]
Pressure	102 170	[Pa]
Density	1.216	[kg/m^3]
Speed of Sound	342.92	[m/s]
Relative Humidity	67	[%]

In Figure 7.10, the time-resolved SPL spectrum of the flyover experiment can be seen. The SPL peak at $t = 22.34$ [s] corresponds to the moment that the aircraft is above the observer (i.e. the overhead position). A snapshot of 0.1 [s] is taken centred around the corresponding time of the desired position of the aircraft. The noise spectra can then be obtained using a Fourier transform with 50% overlap, a Hamming window, and a bandwidth of 6.1035 [Hz].

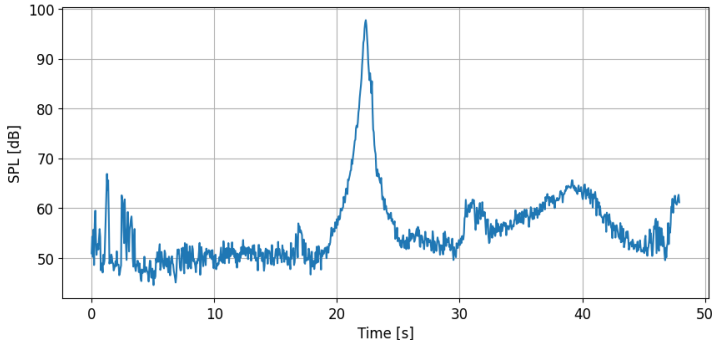

Figure 7.10: SPL over Time of Flyover

It should be noted that the time of maximum received SPL does not exactly coincide with the geometric overhead position due to the speed of sound. The acoustic signal is received with a propagation delay of approximately s_0/c. For the present flyover altitude of $h = 7.43D$, this delay is on the order of 10^{-2} [s] and corresponds to a spatial shift of approximately 1.5 [m]. Furthermore, during the selected time interval of 0.1 [s], the aircraft travels approximately 4 [m]. At the considered altitude, this corresponds to an angular variation of approximately $\pm 10°$. The extracted spectra, therefore, represent a small angular range rather than one angle.

7.2.2. Broadband Noise Prediction - FO1

Three aircraft positions were selected to examine the broadband noise predictions: (i) directly overhead ($t = 22.34$ [s] in Figure 7.10), (ii) 45° before overhead, and (iii) 45° after overhead. At each position, the measured spectra are compared with predictions from the GL and BPM models, using both empirical and XFOIL boundary layer parameters.

Overhead Position

Figure 7.11a shows the narrowband and one-third octave experimental noise spectra when the aircraft is at the overhead position. As shown in Figure 7.11b and Figure 7.11c, the BPM model using empirical boundary layer parameters slightly underpredicts the measured broadband noise levels in both spectral domains. Incorporating XFOIL boundary layer parameters yields improved agreement in SPL amplitude. However, the predicted broadband noise peak shifts to a lower frequency than indicated by the measurements.

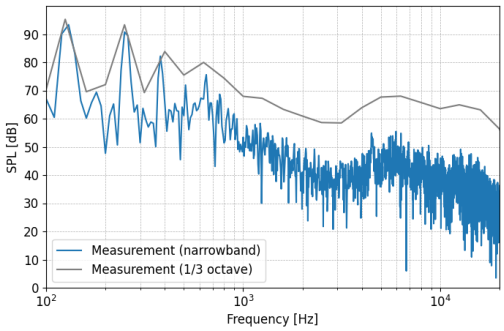

(a) Narrowband vs One-Third Octave Experimental Data

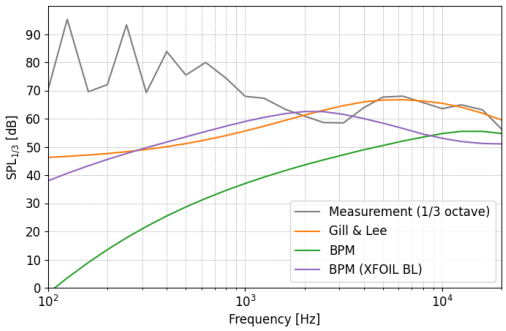

(b) Comparison in the One-Third Octave Domain

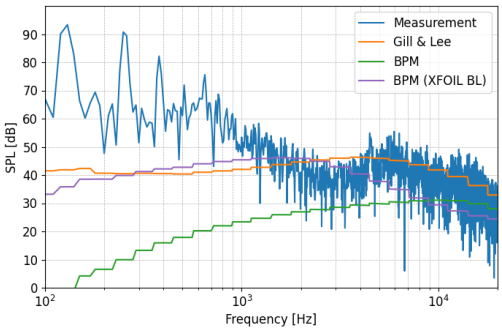

(c) Comparison in the Narrowband Domain

Figure 7.11: Comparison of Measured and Predicted Broadband Noise Spectra for the Flyover at the Overhead Position

The GL model again provides an almost perfect match to the measured spectrum when evaluated at the overhead position. However, based on the directivity and distance scaling analysis carried out for the hover case (subsection 7.1.4), it is known that the GL formulation can fail to account for observer distance when the observer lies in the rotor plane. The agreement observed at the overhead position may therefore be partly coincidental. This motivates assessing the GL model at positions where earlier directivity limitations were less pronounced.

45 Degree Before and After Overhead Position

The results for the observer location 45° before overhead are shown in Figure 7.12. Both variants of the BPM model again exhibit a slight underprediction. In contrast to the overhead result, the GL model now substantially overpredicts the broadband noise levels.

The same behaviour is observed when the aircraft is located 45° after overhead, as shown in Figure 7.13. To investigate the origin of this overprediction, a directivity analysis will be described in the following subsection. The aim is to determine whether similar discrepancies occur at other observer angles and to assess how the GL model behaves across different observer distances in this forward flight validation case.

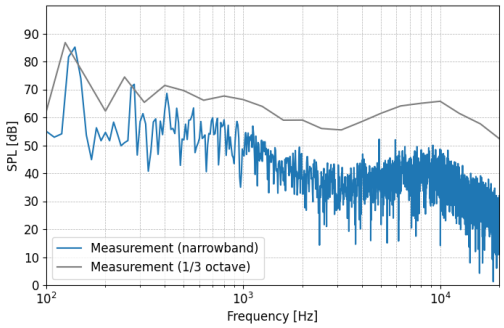

(a) Narrowband vs One-Third Octave Experimental Data

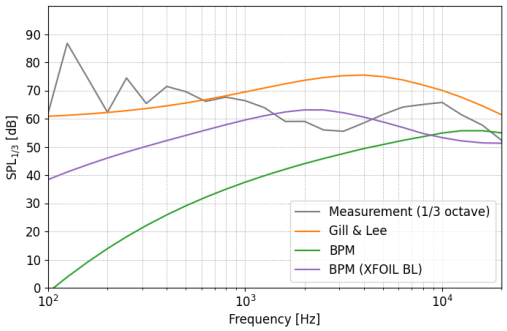

(b) Comparison in the One-Third Octave Domain

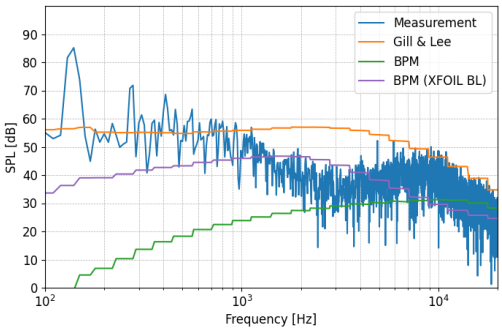

(c) Comparison in the Narrowband Domain

Figure 7.12: Comparison of Measured and Predicted Broadband Noise Spectra for the Flyover at 45° Before the Overhead Position

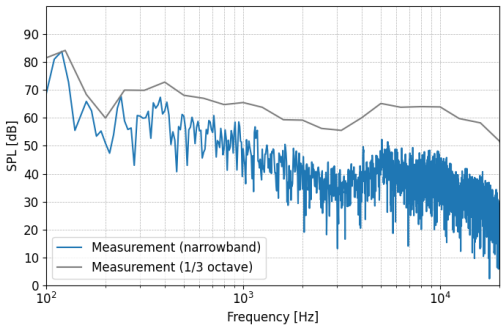

(a) Narrowband vs One-Third Octave Experimental Data

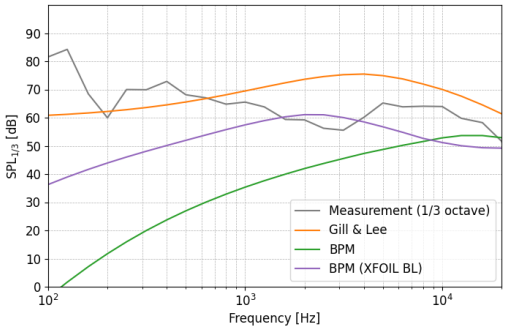

(b) Comparison in the One-Third Octave Domain

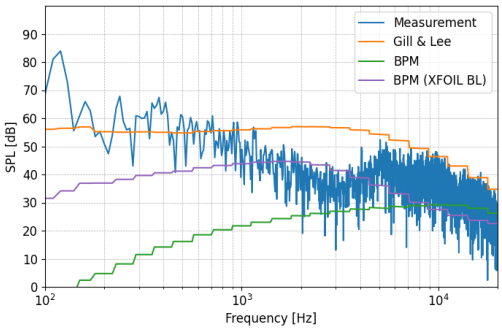

(c) Comparison in the Narrowband Domain

Figure 7.13: Comparison of Measured and Predicted Broadband Noise Spectra for the Flyover at 45° After the Overhead Position

7.2.3. Directivity and Distance Scaling Analysis - FO1

The directivity and distance scaling analysis follows the same conventions as established in subsection 7.1.4 and illustrated in Figure 7.7. The resulting plots for observer radii of 5 [m], 10 [m], 20 [m], and 30 [m] are shown in Figure 7.14. For the BPM model, a clear reduction in sound pressure level with increasing observer distance is observed across all angles. This reduction is consistent with the expected $20\log(s_0)$ spherical spreading behaviour. It confirms that the BPM formulation maintains correct distance scaling under forward flight operating conditions.

In contrast to the hover case, the Gill and Lee model exhibits no meaningful reduction in sound pressure level with increasing observer distance. Increasing the observer radius from 5 [m] to 30 [m] results in a physically unexpected SPL change of approximately 1 [dB] across all observer positions. This indicates that spherical spreading is not properly represented in the GL predictions for this validation case and explains the overprediction observed in the earlier comparisons (Figure 7.12 and Figure 7.13).

Several factors may explain why this unphysical behaviour appears in this validation case, while some degree of distance scaling was still present in the hover validation case. First, the GL model was developed using experimental data primarily obtained from rotors operating in hover [2]. Forward flight is only indirectly represented in the model through a change in thrust coefficient. There is no explicit dependence on, for example, the advance ratio. Second, the blade loading and tip Mach number ranges used to develop the GL model are $0.05 \leq C_T/\sigma \leq 0.18$ and $0.08 \leq M_t \leq 0.67$, respectively. The dataset does not include scenarios with the combination of a high tip speed and a low blade loading [2]. However, the flyover case operates at a blade loading of $C_T/\sigma = 0.035$ and a tip Mach number of approximately $M_t = 0.62$. The scaled propeller experiment, on the other hand, falls well within the ranges with a blade loading of $C_T/\sigma = 0.11$ and a lower tip Mach number of $M_t = 0.28$. Furthermore, the (only) forward flight validation demonstrated in the original work by Gill and Lee [2] involves a smaller COPR-3 propeller (diameter $D = 0.610$ [m]) than the flyover case propeller ($D = 1.64$ [m]).

Additionally, this analysis reaches $s_0/R = 36.59$ at a radius of 30 [m]. This exceeds the upper bound of $s_0/R = 25$ of the training dataset. The absence of any distance-related SPL decrease, even within the nominal training range, suggests that the role of s_0/R in the GL formulation may serve as a scaling parameter tied to the experimental dataset, rather than representing true spherical spreading behaviour. However, this interpretation contrasts with the statement in Gill and Lee's paper [2] that observer distance is factored into the model formulation, as well as with the earlier observed SPL decrease in the hover case. Nevertheless, the present results indicate that the current formulation does not reliably reproduce physical distance scaling under forward flight conditions.

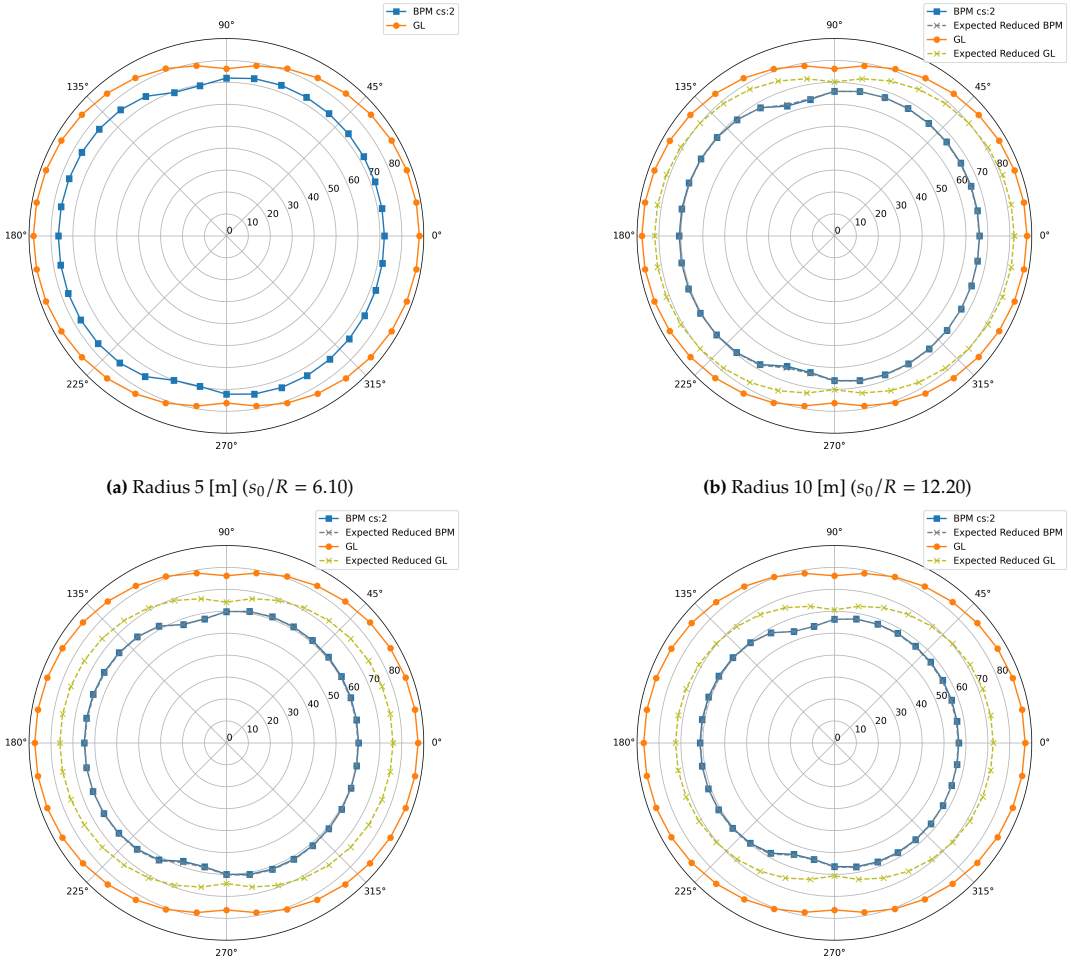

(a) Radius 5 [m] ($s_0/R = 6.10$)

(b) Radius 10 [m] ($s_0/R = 12.20$)

(c) Radius 20 [m] ($s_0/R = 24.39$)

(d) Radius 30 [m] ($s_0/R = 36.59$)

Figure 7.14: Directivity and Distance Scaling Comparison for Different Observer Radii for Validation Case II

7.3. Summary of Broadband Noise Prediction Validation

The validation demonstrates satisfactory agreement between the model predictions and experimental data for the hovering scaled propeller case. The GL model shows a limitation at observer positions in the propeller plane, as the distance term disappears from its formulation. For the forward flight case, the BPM model exhibits a small but consistent underprediction of broadband noise levels, while maintaining physically correct distance scaling. In contrast, the GL model shows significant distance scaling and directivity-related issues. This results in overprediction away from the overhead position. The consequences of these observations and conclusions on the prediction of the entire flyover event will be assessed in section 8.1. Since the GL formulation is primarily derived from hover-based rotor measurements and has been validated only in limited forward flight configurations, its applicability to medium-scale propellers in forward flight remains uncertain. Therefore, section 8.2 will evaluate three additional flyover cases to determine whether similar issues arise and to further explore the boundaries of applicability of the Gill and Lee model in forward flight.

8

Application of the Broadband Noise Framework to Forward Flight Cases

This chapter will present the application of the broadband noise framework to four acoustic measurements of a single-propeller fully electric aircraft. The first part, section 8.1, focuses on the FO1 flyover case, already introduced in section 7.2. It provides a time–frequency analysis by comparing measured spectrograms with predictions obtained using the implemented broadband noise models. These spectrograms allow a qualitative assessment of broadband noise throughout the entire flyover event. The second part, section 8.2, will extend the analysis to three additional take-off cases to evaluate the applicability of the Gill and Lee model in forward flight conditions beyond FO1.

8.1. Spectrograms FO1 Flyover

The spectrogram of the measured FO1 flyover experiment is shown in Figure 8.1. The high sound pressure levels at low frequency, visible as a small, concentrated red region, are most likely due to the propeller's tonal noise. This tonal component has been modelled separately by Yunus et al. [11] and is not included in this thesis. The present study focuses on broadband noise, which dominates the higher frequency region of the spectrogram. These higher frequencies, therefore, constitute the portion of the acoustic signature that broadband noise models aim to predict. The corresponding spectrogram generated using the BPM model with empirically determined boundary layer parameters is shown in Figure 8.2. Its shape matches the measured spectrogram well.

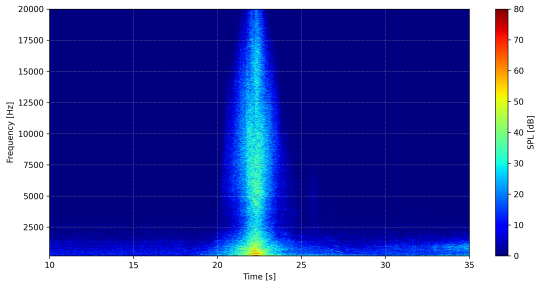

Figure 8.1: Spectrogram FO1 Flyover obtained from Measurement

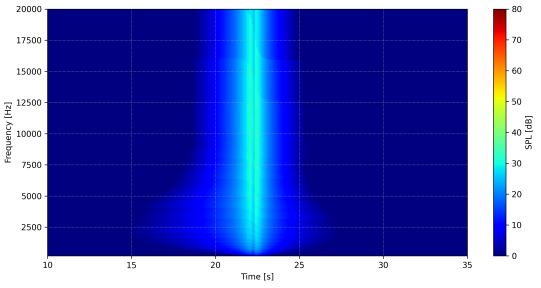

Figure 8.2: Spectrogram FO1 Flyover obtained from BPM Prediction

The spectrogram computed using the BPM model with XFOIL boundary layer parameters is shown in Figure 8.3. Compared to Figure 8.2, a clear increase in sound pressure levels is observed. This is particularly visible in the lower frequency range. A similar feature also appears in the measured spectrogram in Figure 8.1. It remains, however, uncertain whether this energy in the measurement represents broadband content or only the earlier described tonal noise contributions. The observation,

however, is consistent with earlier results: the BPM model using XFOIL boundary layer parameters better matches the measured SPL magnitude but predicts a peak at a lower frequency. A more definitive assessment would require separating the broadband noise component from the tonal noise in the measurements. Another approach would be to combine the broadband models with a tonal noise model and study the total prediction.

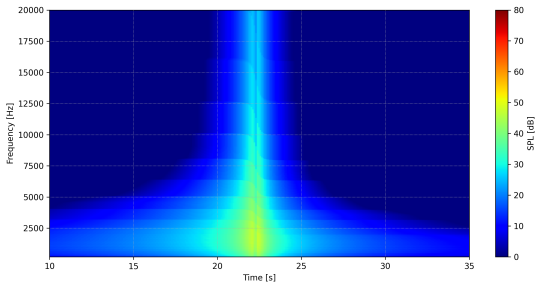

Figure 8.3: Spectrogram FO1 Flyover obtained from BPM Prediction using XFOIL Boundary Layer Parameters

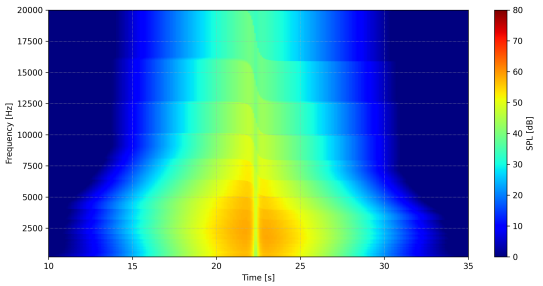

Figure 8.4: Spectrogram FO1 Flyover obtained from Gill and Lee Prediction

The spectrogram obtained using the Gill and Lee model is presented in Figure 8.4. The predicted sound pressure levels are higher than those obtained from the measurement. This is consistent with the overpredictions identified in section 7.2. In all the predicted spectrograms, the frequency shift between the before and after overhead positions is a consequence of the implemented Doppler effect, as described in section A.1. Furthermore, the observed attenuation at higher frequencies is most likely due to atmospheric absorption. This attenuation follows the expectations, given that absorption effects increase with frequency [79] (see section A.1). To assess whether the discrepancies observed in the Gill and Lee predictions are specific to the FO1 case or persist under other flight conditions, three additional take-off cases will be analysed in the next section.

8.2. Applicability of the Gill and Lee Model in Forward Flight

The three additional forward flight take-off cases are summarised in Table 8.1. The operating conditions for these cases are identical to those of the FO1 flyover given earlier in Table 7.3. As before, further details regarding the experiment and aircraft configuration can be found in Elbers [13].

Table 8.1: Flight Conditions of the Take-Off Experiments

Case	h [m]	V_{inf} [m/s]	RPM	α_{disk} [°]	J
TO1	46.46D	31.0443	2430	5.6	0.4674
TO2	24.16D	36.8442	2460	2.53	0.5480
TO3	26.07D	36.1095	2440	2.67	0.5414

8.2.1. Comparison with Measurements

The spectrogram of the first take-off case (TO1) is shown in Figure 8.5a. Compared to FO1 (Figure 8.1), TO1 shows a broader noise contour with significantly reduced sound pressure levels at higher frequencies. The noise is mainly concentrated below 10 000 [Hz]. As previously mentioned, atmospheric absorption damps the higher frequencies most strongly (section A.1). The greater altitude of this take-off case may therefore explain the reduced high-frequency content. The Gill and Lee prediction shown in Figure 8.5b again substantially overpredicts the broadband noise. This is consistent with the behaviour observed for FO1. The overprediction suggests similar directivity and distance scaling issues of the Gill and Lee model as found for the flyover case in section 7.2.

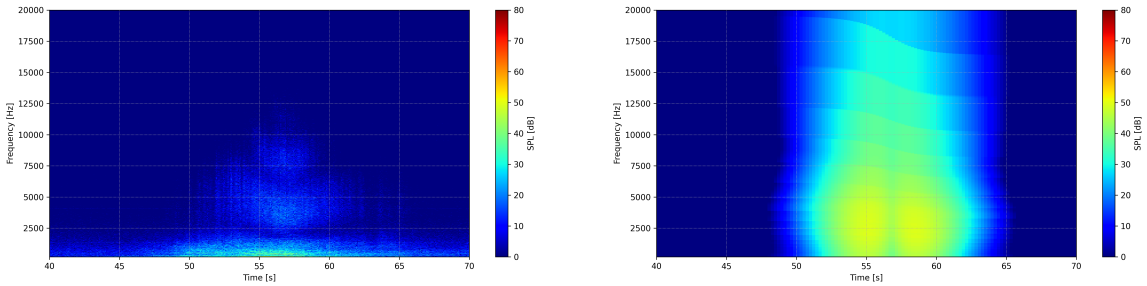

(a) Measurement **(b)** Gill and Lee Model

Figure 8.5: Comparison of the Spectrogram predicted by the Gill and Lee Model against Experimental Data for the TO1 Case

For the remaining take-off cases TO2 and TO3, shown in Figure 8.6 and Figure 8.7, a similar overprediction is observed. However, the overall shape of the Gill and Lee spectrograms (Figure 8.6b and Figure 8.7b) more closely resembles the experimental contours (Figure 8.6a and Figure 8.7a) than in either FO1 or TO1. A notable observation, however, is that all four Gill and Lee predictions (FO1, TO1, TO2, and TO3) show a consistent, similar pear-shaped distribution. In these cases, only the SPL magnitude changes, while the overall spectrogram shape remains the same. This indicates that the Gill and Lee formulation does not distinguish between different forward flight conditions (e.g., from level flight to take-off). However, this behaviour aligns with expectations, as the model does not contain any explicit variables representing flight condition, such as advance ratio or propeller disk angle.

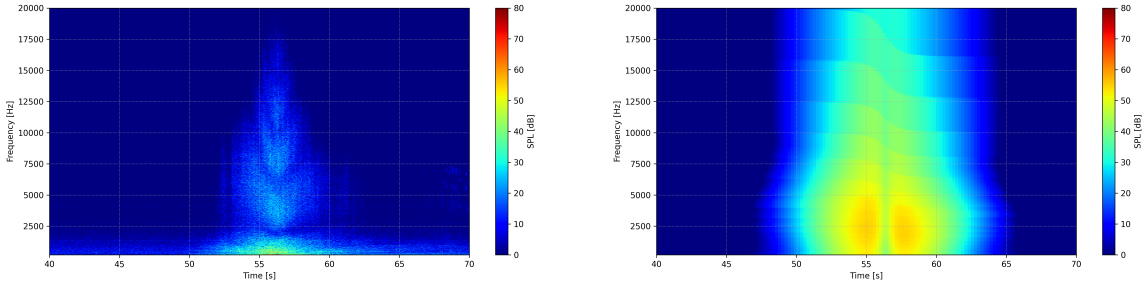

(a) Measurement **(b)** Gill and Lee Model

Figure 8.6: Comparison of the Spectrogram predicted by the Gill and Lee Model against Experimental Data for the TO2 Case

The overprediction behaviour identified in FO1 is also evident in each take-off case. Varying the freestream velocity, propeller rotational speed, or flight altitude did not mitigate the previously observed directivity and distance scaling issues. A limited sensitivity study suggested that reducing the propeller radius below approximately 0.6 [m] eliminated the abnormal distance scaling (i.e. SPL remaining nearly constant between 5 [m] and 30 [m]). While this could not be experimentally validated in this thesis, it may indicate a dependency on propeller size or propeller tip velocity. Also, further research is necessary to determine whether the propeller radius is directly responsible or acts indirectly, for example, through changes in inflow. Nevertheless, the only forward flight validation provided in Gill and Lee's paper corresponds to a significantly smaller propeller, suggesting a plausible explanation.

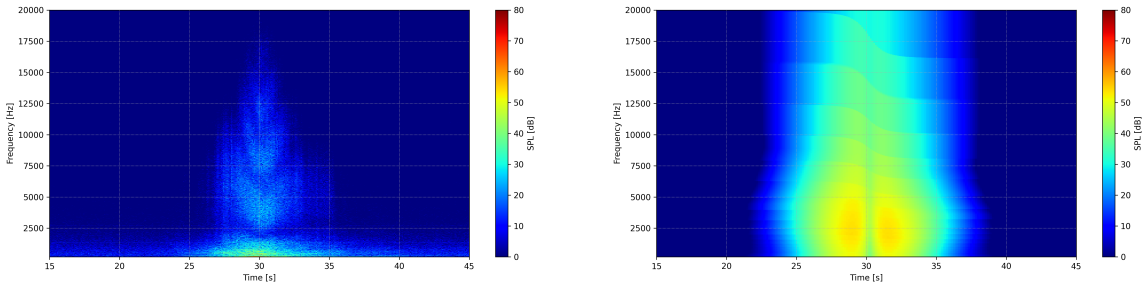

(a) Measurement

(b) Gill and Lee Model

Figure 8.7: Comparison of the Spectrogram predicted by the Gill and Lee Model against Experimental Data for the TO3 Case

Across all four forward flight cases examined in this thesis, the Gill and Lee model did not demonstrate physically consistent behaviour or agreement with experimental results. Consequently, the concluding suggestion by Gill and Lee that forward flight applicability could be achieved indirectly by adjusting the thrust coefficient [2] is not supported by the present findings. Incorporating explicit flight condition parameters into the formulation appears necessary for reliable prediction of propeller broadband noise in forward flight.

8.2.2. Comparison with Predictions using the BPM Model

The BPM model, in contrast, demonstrates a better agreement across all three take-off cases (Figure 8.8, Figure 8.9 and Figure 8.10). Spectrograms generated using both empirical boundary layer parameters and XFOIL boundary layer parameters remain reasonably close to the experimental data. Based on these results, the BPM formulation remains the more reliable model for predicting broadband propeller noise in forward flight conditions.

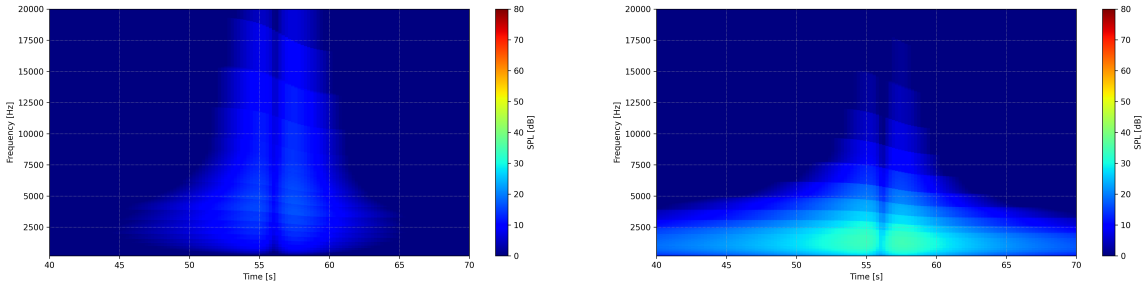

(a) Empirical Boundary Layer Parameters

(b) XFOIL Boundary Layer Parameters

Figure 8.8: Spectrograms for TO1 as predicted by the BPM Model

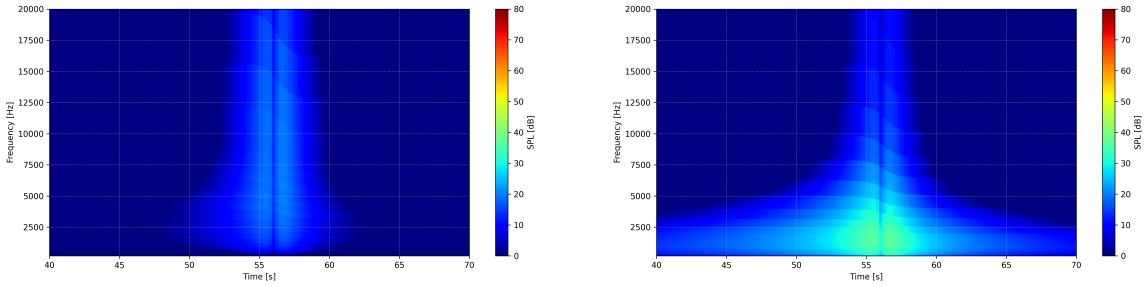

(a) Empirical Boundary Layer Parameters

(b) XFOIL Boundary Layer Parameters

Figure 8.9: Spectrograms for TO2 as predicted by the BPM Model

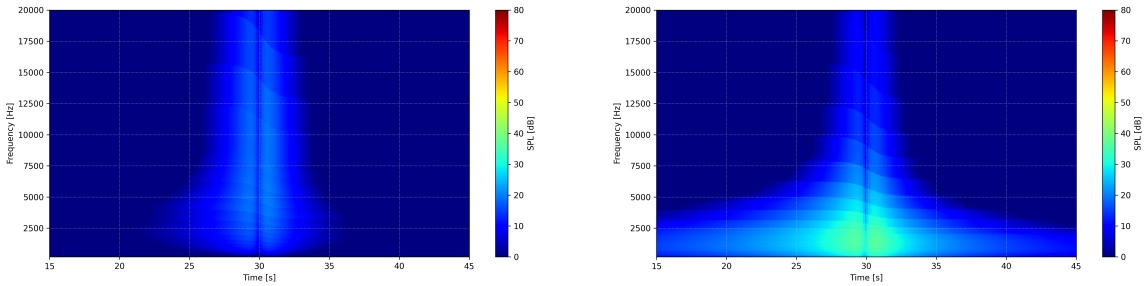

(a) Empirical Boundary Layer Parameters

(b) XFOIL Boundary Layer Parameters

Figure 8.10: Spectrograms for TO3 as predicted by the BPM Model

9

Conclusions, Limitations, and Recommendations

This thesis investigated the prediction of broadband noise generated by propellers operating in hover and forward flight conditions. A modular broadband noise prediction framework was developed and applied to experimental propeller measurements in both hover and forward flight. A particular focus was on the accuracy of the implemented (semi-)empirical models across different flight conditions (hover, level forward flight, and take-off). Two broadband noise models were considered in the framework: the Brooks, Pope, and Marcolini (BPM) model [1] and the more recently developed Gill and Lee (GL) model [2]. An advantage of the Gill and Lee model over the classical BPM formulation is its reliance on propeller performance parameters, such as the thrust coefficient and tip Mach number, rather than on detailed boundary layer parameters, which are often computationally expensive to obtain accurately. For the BPM model, two variants were considered. They are distinguished by the source of the boundary layer parameters: empirically derived parameters following the BPM formulation, or parameters extracted from XFOIL. The following sections will summarise the main conclusions of the thesis. Next, the limitations of this research will be identified. Following the conclusions and limitations, recommendations for future research will be provided.

9.1. Conclusions

Both broadband noise models showed satisfactory agreement with experimental measurements under hover conditions. Both versions of the BPM model slightly underpredicted broadband noise levels. The Gill and Lee model, on the other hand, closely reproduced the measured sound pressure levels and overall spectral trends. These results suggest that the Gill and Lee model is well-suited for hover operating conditions, which are particularly relevant for electric vertical take-off and landing (e-VTOL) vehicles and urban air mobility applications. However, the directivity and distance scaling analysis in hover revealed an important limitation of the Gill and Lee model. At observer positions close to the propeller plane, the distance dependence effectively disappears from the model formulation. This results in an unphysically small variation in sound pressure level with increasing observer distance in the propeller plane. Furthermore, the distance scaling at other observer angles does not match the expected sound pressure level loss due to spherical spreading ($20\log(s_0)$).

When applied to forward flight conditions, the limitations of the Gill and Lee model become more pronounced. Validation against full-scale single-propeller fully electric aircraft flyover measurements showed a systematic overprediction of broadband noise levels for multiple observer positions. In contrast to the hover case, the Gill and Lee model exhibited almost no reduction in predicted sound pressure level with increasing observer distance. These findings were further supported by the overpredictions observed in the spectrogram analysis of the level forward flight case and three take-off cases. Across all cases, the Gill and Lee model produced spectrograms with nearly identical shapes, despite variations in observer distance, freestream velocity, propeller rotational speed, and propeller disk angle. This

lack of sensitivity suggests that the model does not adequately capture the influence of varying flight conditions (hover, level flight, and take-off).

Several plausible explanations for this behaviour were identified. First, the Gill and Lee model was primarily developed and trained using hover data with blade loading and tip Mach number ranges of $0.05 \leq C_T/\sigma \leq 0.18$ and $0.08 \leq M_t \leq 0.67$, respectively, and limited validation in forward flight. The forward flight case in this thesis operates at a smaller blade loading of $C_T/\sigma = 0.035$ and a relatively high tip Mach number of $M_t = 0.62$. This combination of low blade loading and high tip speed is not represented in the original training dataset and may therefore fall outside the model's validity range. As a result, the underlying formulation may not capture the different aerodynamic mechanisms introduced by forward flight, such as changes in inflow velocity and thus the effective angle of attack of the propeller blades. Second, and closely related to this, the model formulation does not explicitly include flight condition parameters, such as advance ratio or propeller disk angle. Third, the experimental validation presented by Gill and Lee for forward flight corresponds to a significantly smaller propeller than the one investigated in this thesis. This, along with a short sensitivity study, suggests that propeller size or tip speed effects may play an important role in the applicability of the Gill and Lee model. However, this hypothesis should be further researched. Finally, the identified directivity and distance scaling issues at observer positions near the propeller plane, where the distance dependence effectively vanishes from the formulation, further limit the model's reliability in realistic flyover scenarios. The contrasting behaviour observed between hover and forward flight suggests that the normalised observer distance term (s_0/R) in the Gill and Lee formulation primarily reflects scaling within the bounds of the experimental training data, rather than representing true spherical spreading.

The forward flight analyses presented in this thesis indicate that the BPM model remains the more accurate method for predicting broadband propeller noise under forward flight conditions. Using boundary layer parameters extracted from XFOIL improved agreement with the measured sound pressure level magnitude, whereas empirically defined boundary layer parameters yielded a better prediction of the spectral peak location. Compared to the Gill and Lee model, the BPM model captures the variations in operating conditions and spherical spreading behaviour more effectively. This results in spectrograms that more closely match the measured acoustic signatures. Additionally, the findings in this thesis highlight the potential of the Gill and Lee modelling philosophy. The strong agreement observed in hover conditions and the reduced input requirements suggest that broadband noise models based on propeller performance parameters offer a promising direction for future research. With further development to account for varying flight conditions, these models may eventually surpass conventional approaches in terms of usability and predictive accuracy.

9.2. Limitations

Several limitations of the present study should be acknowledged. First, the comparison between predicted and measured broadband noise was complicated by tonal noise components in the experimental data. This limited the ability to perform a purely quantitative broadband noise validation. Second, the investigation of the Gill and Lee model limitations in forward flight was constrained to a limited set of experimental cases for a single propeller configuration. Although consistent trends were observed across all cases, the generality of the conclusions could not be assessed without broader experimental research. In addition, the exploratory sensitivity analysis on propeller radius and distance scaling could not be experimentally validated within the scope of this thesis. As a result, the role of propeller size and tip speed in the observed discrepancies remains speculative. Finally, this study cannot conclusively determine whether the normalised observer distance term (s_0/R) in the Gill and Lee model represents true spherical spreading behaviour or serves as a scaling parameter within the bounds of the experimental training database. Therefore, the physical interpretation of the distance dependence in the Gill and Lee formulation remains uncertain.

9.3. Recommendations for Future Work

Based on the conclusions and limitations identified in this thesis, several directions for future research are recommended. First, the broadband noise models should either be combined with a tonal noise prediction model or separated from the tonal noise components. These two approaches would yield a more adequate comparison between the predictions and measurements and support a more complete

assessment of propeller noise. In addition to conventional spectral comparisons, future studies should evaluate broadband noise models from a perceptual perspective. This would help assess how accurately different modelling approaches represent the noise as perceived by an observer. It is relevant for evaluating the importance of the differences observed in this thesis, such as the difference between improved sound pressure level magnitude with BPM using XFOIL boundary layer parameters and improved spectral peak prediction with empirically obtained boundary layer parameters.

Further research should focus on other hover and forward flight cases to identify the operational regime in which the Gill and Lee model becomes inapplicable. In parallel, the limiting factors governing the applicability of the Gill and Lee model in forward flight can be examined in more detail. In particular, the hypothesis that propeller radius or tip velocity plays an important role in the observed discrepancies in forward flight should be evaluated using a broader range of propeller sizes and rotational speeds.

Another recommendation is to expand the experimental database used to train and validate the Gill and Lee model. Including forward flight cases and a wider range of observer positions would help address the identified directivity and distance scaling issues. This could, for example, possibly resolve the limitation at the overhead position, where the current formulation exhibits non-physical distance scaling behaviour. In addition, developing a new broadband noise model following the general methodology of Gill and Lee represents a promising direction for future work. By explicitly incorporating flight condition parameters, such as advance ratio and propeller disk angle, and using machine learning, the forward flight applicability of these models could be significantly improved. Finally, the broadband noise framework developed in this thesis could be extended to include additional (semi-)empirical models, such as the TNO model. This would improve the identification of the relative strengths and limitations of the different models and support the development of more robust broadband noise prediction tools for future electric propulsion.

References

[1] T. F. Brooks, D. Stuart, and M. A. Marcolini, "Airfoil Self-Noise and Prediction," Jul. 1989.

[2] H. Gill and S. Lee, "Development of New Empirical Rotor Broadband Noise Prediction Models for Urban Air Mobility Applications," in *AIAA SCITECH 2024 Forum*, Reston, Virginia: American Institute of Aeronautics and Astronautics, Jan. 2024. DOI: 10.2514/6.2024-2473.

[3] ANP, *Schiphol to maintain 15% noise reduction plan despite calls for greater cuts*, Feb. 2025.

[4] Schiphol, *Schiphol's response to announced package of measures by Ministry of I&W*, Sep. 2024.

[5] Federal Aviation Administration, "United States Aviation Climate Action Plan," 2021.

[6] Magliozzi and A. Hanson, "Propeller and Propfan Noise," 1991.

[7] A. Stoll and J. Bevirt, "Development Of eVTOL Aircraft For Urban Air Mobility At Joby Aviation," in *Proceedings of the Vertical Flight Society 78th Annual Forum*, The Vertical Flight Society, May 2022, pp. 1–11. DOI: 10.4050/F-0078-2022-17528.

[8] B. Ibeawuchi, *The Battle for eVTOL Supremacy: Joby and Archer Aviation Race to Reshape the Low Altitude Economy*, Sep. 2025.

[9] J. Hua and R. R. Mankbadi, "Prediction and Control of Broadband Noise Associated with Advanced Air Mobility—A Review," *Applied Sciences*, vol. 14, no. 18, p. 8455, Sep. 2024. DOI: 10.3390/app14188455.

[10] S. Glegg and W. Devenport, "Broadband noise from open rotors and leading edge noise," in *Aeroacoustics of Low Mach Number Flows*, Elsevier, 2024, ch. 13, pp. 409–427. DOI: 10.1016/b978-0-443-19112-1.00016-3.

[11] F. Yunus, B. V. von Den Hoff, and M. Snellen, "Predicting tonal noise of full-electric propeller-driven aircraft in outdoor environments using low-order models," *30th AIAA/CEAS Aeroacoustics Conference, 2024*, 2024. DOI: 10.2514/6.2024-3418.

[12] C. B. Bello, "The development of a distributed electric propulsion (DEP) noise model," Delft, Dec. 2023.

[13] N. Elbers, "Assessment of an aircraft propeller noise model by verification and experimental validation," Delft, 2021.

[14] S. Glegg and W. Devenport, "Propeller and open rotor noise," in *Aeroacoustics of Low Mach Number Flows*, Elsevier, 2024, ch. 6, pp. 163–206. DOI: 10.1016/b978-0-443-19112-1.00017-5.

[15] N. S. Zawodny, J. Boyd D. Douglas, and C. L. Burley, "Acoustic Characterization and Prediction of Representative, Small-Scale Rotary-Wing Unmanned Aircraft System Components," 2016.

[16] T. F. Brooks, M. A. Marcolini, and D. S. Pope, "Main Rotor Broadband Noise Study in the DNW," *Journal of the American Helicopter Society*, vol. 34, no. 2, pp. 3–12, Apr. 1989. DOI: 10.4050/JAHS.34.2.3.

[17] C. S. Thurman and J. D. Baeder, "Blade-Wake Interaction Noise for Small Hovering Rotors, Part I: Characterization Study," *AIAA Journal*, vol. 61, no. 6, pp. 2552–2569, May 2023. DOI: 10.2514/1.J062565.

[18] A. Pagano, M. Barbarino, D. Casalino, and L. Federico, "Tonal and broadband noise calculations for aeroacoustic optimization of a pusher propeller," *Journal of Aircraft*, vol. 47, no. 3, pp. 835–848, 2010. DOI: 10.2514/1.45315.

[19] S. Lee, L. Ayton, F. Bertagnolio, S. Moreau, T. P. Chong, and P. Joseph, "Turbulent boundary layer trailing-edge noise: Theory, computation, experiment, and application," *Progress in Aerospace Sciences*, vol. 126, p. 100 737, Oct. 2021. DOI: 10.1016/j.paerosci.2021.100737.

[20] N. Pettingill and N. Zawodny, "Identification and Prediction of Broadband Noise for a Small Quadcopter," in *Proceedings of the Vertical Flight Society 75th Annual Forum*, The Vertical Flight Society, May 2019, pp. 1–16. DOI: 10.4050/F-0075-2019-14443.

[21] R. W. Paterson and R. K. Amiet, "Noise of a model helicopter rotor due to ingestion of isotropic turbulence," *Journal of Sound and Vibration*, vol. 85, no. 4, pp. 551–577, Dec. 1982. DOI: 10.1016/0022-460X(82)90323-6.

[22] S. Redonnet and T. G. Schmidt, "Experimental investigation of the laminar boundary layer vortex-shedding noise by an airfoil within a closed-vein wind tunnel," *International Journal of Aeroacoustics*, vol. 21, no. 8, pp. 658–683, Nov. 2022. DOI: 10.1177/1475472X221136882.

[23] C. S. Thurman, N. S. Zawodny, and N. A. Pettingill, "The Effect of Boundary Layer Character on Stochastic Rotor Blade Vortex Shedding Noise," in *78th Vertical Flight Society Annual Forum and Technology Display, FORUM 2022*, Vertical Flight Society, 2022. DOI: 10.4050/f-0078-2022-17428.

[24] S. Glegg and W. Devenport, "Trailing edge noise and roughness noise," in *Aeroacoustics of Low Mach Number Flows*, Elsevier, 2024, ch. 14, pp. 429–461. DOI: 10.1016/b978-0-443-19112-1.00011-4.

[25] J. E. Williams and L. H. Hall, "Aerodynamic sound generation by turbulent flow in the vicinity of a scattering half plane," *Journal of Fluid Mechanics*, vol. 40, no. 4, pp. 657–670, Mar. 1970. DOI: 10.1017/S0022112070000368.

[26] R. Amiet, "Noise due to turbulent flow past a trailing edge," *Journal of Sound and Vibration*, vol. 47, no. 3, pp. 387–393, Aug. 1976. DOI: 10.1016/0022-460X(76)90948-2.

[27] R. Schlinker and R. Amiet, "Helicopter rotor trailing edge noise," in *7th Aeroacoustics Conference*, Reston, Virigina: American Institute of Aeronautics and Astronautics, Oct. 1981. DOI: 10.2514/6.1981-2001.

[28] S. Sinayoko, M. Kingan, and A. Agarwal, "Trailing edge noise theory for rotating blades in uniform flow," *Proceedings of the Royal Society A: Mathematical, Physical and Engineering Sciences*, vol. 469, no. 2157, Sep. 2013. DOI: 10.1098/rspa.2013.0065.

[29] M. Roger and S. Moreau, "Back-scattering correction and further extensions of Amiet's trailing-edge noise model. Part 1: theory," *Journal of Sound and Vibration*, vol. 286, no. 3, pp. 477–506, Sep. 2005. DOI: 10.1016/J.JSV.2004.10.054.

[30] M. S. Howe, "A review of the theory of trailing edge noise," *Journal of Sound and Vibration*, vol. 61, no. 3, pp. 437–465, Dec. 1978. DOI: 10.1016/0022-460X(78)90391-7.

[31] D. Casalino, E. Grande, G. Romani, D. Ragni, and F. Avallone, "Definition of a benchmark for low Reynolds number propeller aeroacoustics," *Aerospace Science and Technology*, vol. 113, p. 106 707, Jun. 2021. DOI: 10.1016/J.AST.2021.106707.

[32] Y. S. Jung, J. Baeder, and C. He, "Investigation of empirical rotor broadband prediction using CFD boundary layer parameters extraction," *77th Annual Vertical Flight Society Forum and Technology Display, FORUM 2021: The Future of Vertical Flight*, 2021. DOI: 10.4050/F-0077-2021-16692.

[33] R. R. Mankbadi, S. Afari, and V. V. Golubev, "Simulations of Broadband Noise of a Small UAV Propeller," in *AIAA Scitech 2020 Forum*, Reston, Virginia: American Institute of Aeronautics and Astronautics, Jan. 2020. DOI: 10.2514/6.2020-1493.

[34] F. Farassat, "Derivation of Formulations 1 and 1A of Farassat," 2007.

[35] F. T. Kunz, S. Pullin, B. Y. Zhou, *et al.*, "High-Fidelity Propeller Broadband Noise Prediction using SU2," *AIAA Aviation and Aeronautics Forum and Exposition, AIAA AVIATION Forum 2023*, 2023. DOI: 10.2514/6.2023-4185.

[36] C. S. Thurman, N. S. Zawodny, N. A. Pettingill, L. V. Lopes, and J. D. Baeder, "Physics-informed broadband noise source identification and prediction of an ideally twisted rotor," in *AIAA Scitech 2021 Forum*, American Institute of Aeronautics and Astronautics Inc, AIAA, 2021, pp. 1–15. DOI: 10.2514/6.2021-1925.

[37] W. W. Willmarth and F. W. Roos, "Resolution and structure of the wall pressure field beneath a turbulent boundary layer," *Journal of Fluid Mechanics*, vol. 22, no. 1, pp. 81–94, 1965. DOI: 10.1017/S0022112065000599.

[38] S. Glegg and W. Devenport, "Wall pressure fluctuations in turbulent boundary layers," in *Aeroacoustics of Low Mach Number Flows*, Academic Press, Jan. 2024, ch. 12, pp. 379–405. DOI: 10.1016/B978-0-443-19112-1.00003-5.

[39] M. Goody, "Empirical spectral model of surface pressure fluctuations," *AIAA Journal*, vol. 42, no. 9, pp. 1788–1794, 2004. DOI: 10.2514/1.9433.

[40] Y. F. Hwang, W. K. Bonness, and S. A. Hambric, "Comparison of semi-empirical models for turbulent boundary layer wall pressure spectra," *Journal of Sound and Vibration*, vol. 319, no. 1-2, pp. 199–217, Jan. 2009. DOI: 10.1016/J.JSV.2008.06.002.

[41] S. Lee, "Empirical Wall-Pressure Spectral Modeling for Zero and Adverse Pressure Gradient Flows," *AIAA Journal*, vol. 56, no. 5, pp. 1818–1829, May 2018. DOI: 10.2514/1.J056528.

[42] R. Parchen, "Progress Report DRAW: A Prediction Scheme for Trailing Edge Noise Based on Detailed Boundary Layer Characteristics," 1998.

[43] W. K. Blake and S. Temkin, "Mechanics of Flow-Induced Sound and Vibration. Vol. I: General Concepts and Elementary Sources by William K. Blake," *The Journal of the Acoustical Society of America*, vol. 83, no. 1, pp. 397–398, Jan. 1988. DOI: 10.1121/1.396227.

[44] D. Nguyen and S. Lee, "Investigation on the Accuracy of the TNO Model Using RANS CFD and XFOIL Inputs for Airfoil Trailing Edge Noise Predictions," in *2018 AIAA/CEAS Aeroacoustics Conference*, Reston, Virginia: American Institute of Aeronautics and Astronautics, Jun. 2018. DOI: 10.2514/6.2018-2811.

[45] A. Fischer, F. Bertagnolio, and H. A. Madsen, "Improvement of TNO type trailing edge noise models," *European Journal of Mechanics, B/Fluids*, vol. 61, pp. 255–262, Jan. 2017. DOI: 10.1016/j.euromechflu.2016.09.005.

[46] F. Bertagnolio, A. Fischer, and W. Jun Zhu, "Tuning of turbulent boundary layer anisotropy for improved surface pressure and trailing-edge noise modeling," *Journal of Sound and Vibration*, vol. 333, no. 3, pp. 991–1010, Feb. 2014. DOI: 10.1016/J.JSV.2013.10.008.

[47] D. S. Weir, S. J. Jumper, C. L. Burley, and R. A. Golub, "Aircraft noise prediction program theoretical manual: Rotorcraft System Noise Prediction System (ROTONET), part 4," 1995.

[48] F. W. Grosveld, "Prediction of broadband noise from horizontal axis wind turbines," *Journal of Propulsion and Power*, vol. 1, no. 4, pp. 292–299, Jul. 1985. DOI: 10.2514/3.22796.

[49] P. Bortolotti, E. Branlard, A. Platt, P. Moriarty, C. Sucameli, and C. Bottasso, "Aeroacoustics Noise Model of OpenFAST," Golden, CO (United States), Aug. 2020. DOI: 10.2172/1660130.

[50] J. D. Blake, C. S. Thurman, N. S. Zawodny, and L. V. Lopes, "Broadband Predictions of Optimized Proprotors in Axial Forward Flight," in *AIAA AVIATION 2023 Forum*, Reston, Virginia: American Institute of Aeronautics and Astronautics, Jun. 2023. DOI: 10.2514/6.2023-4183.

[51] S. Li and S. Lee, "UCD-QuietFly: A New Program to Predict Multi-Rotor eVTOL Broadband Noise," Jan. 2020.

[52] S. Li and S. Lee, "Prediction of Rotorcraft Broadband Trailing-Edge Noise and Parameter Sensitivity Study," *Journal of the American Helicopter Society*, vol. 65, no. 4, Oct. 2020. DOI: 10.4050/JAHS.65.042006.

[53] S. Li and S. Lee, "Prediction of Urban Air Mobility Multirotor VTOL Broadband Noise Using UCD-QuietFly," *Journal of the American Helicopter Society*, vol. 66, no. 3, Jul. 2021. DOI: 10.4050/JAHS.66.032004.

[54] J. E. Ffowcs Williams and D. L. Hawkings, "Sound Generation by Turbulence and Surfaces in Arbitrary Motion," 1969.

[55] M. H. Dunn and G. M. Tarkenton, "Computational methods in the prediction of advanced subsonic and supersonic propeller induced noise: ASSPIN users' manual," 1992.

[56] F. Teixeira Kunz, L. Ugur, B. Y. Zhou, and R. Ewert, "A Machine Learning FRPM Model for Broadband Noise Prediction," in *30th AIAA/CEAS Aeroacoustics Conference (2024)*, Reston, Virginia: American Institute of Aeronautics and Astronautics, Jun. 2024. DOI: 10.2514/6.2024-3129.

[57] S. Redonnet, T. Bose, A. Seth, and L. K. Li, "Airfoil self-noise prediction using deep neural networks," *Engineering Analysis with Boundary Elements*, vol. 159, pp. 180–191, Feb. 2024. DOI: 10.1016/J.ENGANABOUND.2023.11.024.

[58] I. Grigas, M. Castro Gracia, E. Devos, *et al.*, "High-performance Acoustic Rotor & Modular Noise-Integrating Architecture," Jun. 2025.

[59] M. Drela, "XFOIL: An Analysis and Design System for Low Reynolds Number Airfoils," in 54), Berlin, Germany, Springer-Verlag, 1989, Berlin, Germany, Springer-Verlag, 1989, pp. 1–12. DOI: 10.1007/978-3-642-84010-4{_}1.

[60] S. Gudmundsson, "Thrust Modeling for Propellers," *General Aviation Aircraft Design*, pp. 597–656, Jan. 2022. DOI: 10.1016/B978-0-12-818465-3.00015-X.

[61] H. Hou, W. Shi, Y. Xu, and Y. Song, "Actuator disk theory and blade element momentum theory for the force-driven turbine," *Ocean Engineering*, vol. 285, p. 115 488, Oct. 2023. DOI: 10.1016/J.OCEANENG.2023.115488.

[62] T. Sinnige, "Aerodynamic and Aeroacoustic Interaction Effects for Tip-Mounted Propellers An Experimental Study," Ph.D. dissertation, Sep. 2018. DOI: 10.4233/uuid:214e1e9a-c53e-47c7-a12c-b1eb3ec8293b.

[63] B. Massey and J. Ward-Smith, *Mechanics of fluids*, 8th ed. Crc Press, 2006, vol. 1.

[64] G. J. Ruijgrok, M. Voskuijl, and C. Varriale, *Elements of Airplane Performance*. TU Delft OPEN Publishing, Nov. 2025. DOI: 10.59490/mt.235.

[65] F. Yunus, "Methodologies and algorithms for sound propagation in complex environments with application to urban air mobility: A ray acoustics approach," Ph.D. dissertation, Delft University of Technology, 2023. DOI: /10.4233/uuid:72d10b7a-6790-41fc-9b15-26f9cccdb77f.

[66] L. A. Viterna and R. D. Corrigan, "Fixed pitch rotor performance of large horizontal-axis wind turbines," 1982.

[67] T. Sinnige, "AE4130 – Aircraft Aerodynamics: Propeller Propulsion Aerodynamics," Jan. 2025.

[68] G. J. Leishman, *Principles of Helicopter Aerodynamics*, 2nd ed. Cambridge: Cambridge University Press, 2016.

[69] C. E. Tinney and J. A. Valdez, "Hover Performance and Acoustics of a 35% Scale Notional eVTOL Rotor.," in *30th AIAA/CEAS Aeroacoustics Conference, 2024*, American Institute of Aeronautics and Astronautics Inc, AIAA, 2024. DOI: 10.2514/6.2024-3219.

[70] C. Ferreira, "Gene Expression Programming: a New Adaptive Algorithm for Solving Problems," *Complex Systems*, vol. 13, no. 2, pp. 87–129, Dec. 2001. DOI: 10.48550/arXiv.cs/0102027.

[71] J. Wayne, "Noise," in *Rotorcraft Aeromechanics*, ser. Cambridge Aerospace Series, W. Johnson, Ed., Cambridge: Cambridge University Press, 2013, ch. 14, pp. 493–544.

[72] L. F. Vargas, "Wind Turbine Noise Prediction," Ph.D. dissertation, Instituto Superior Técnico, Lisbon, 2008.

[73] H. Wu, P. Zhou, X. Zhang, *et al.*, "Broadband Noise of a Hovering Rotor: Measurement, Prediction, and Reduction," *AIAA Journal*, vol. 63, no. 8, pp. 3275–3287, Aug. 2025. DOI: 10.2514/1.J064974.

[74] N. S. Zawodny, N. A. Pettingill, L. V. Lopes, and D. J. Ingraham, "Experimental Validation of an Acoustically and Aerodynamically Optimized UAM Proprotor Part 1: Test Setup and Results," 2023.

[75] C. E. Tinney and J. A. Valdez, "Optimum Hover Conditions for Reduced Noise from a Notional eVTOL Rotor," in *AIAA Aviation Forum and ASCEND, 2025*, American Institute of Aeronautics and Astronautics Inc, AIAA, 2025, pp. 1–15. DOI: 10.2514/6.2025-3136.

[76] C. E. Tinney, J. Valdez, and Y. Zhao-Dubuc, "Urban Air Mobility Rotor Noise at Moderate Reynolds Numbers with Collective Pitch Control," in *11th Convention of the European Acoustics Association*, Jun. 2025.

[77] U. Boatto, P. A. Bonnet, F. Avallone, and D. Ragni, "Assessment of Blade Element Momentum Theory-based engineering models for wind turbine rotors under uniform steady inflow," *Renewable Energy*, vol. 214, pp. 307–317, Sep. 2023, ISSN: 0960-1481. DOI: 10.1016/J.RENENE.2023.04.050.

[78] H. Wu, W. Chen, H. Jiang, S. Zhong, and X. Zhang, "Experimental investigation of the effect of sectional airfoil profile deviation on propeller noise," *Physics of Fluids*, vol. 35, no. 2, Feb. 2023. DOI: 10.1063/5.0135555.

[79] M. Arntzen, *Aircraft noise calculation and synthesis in a non-standard atmosphere*. 2014. DOI: 10.4233/uuid:c56e213c-82db-423d-a5bd-503554653413.

[80] D. G. Simons and M. Snellen, "Course AE4431-23 Aircraft Noise: An introduction to general acoustics and aircraft noise," Sep. 2023.

[81] P. Koelewijn, *Noise Control: Part 1 – What is sound?* Feb. 2018. [Online]. Available: https://www.heinenhopman.com/noise-control-part-1-what-is-sound/.

[82] A. Filippone, "Aircraft noise prediction," *Progress in Aerospace Sciences*, vol. 68, pp. 27–63, 2014. DOI: 10.1016/j.paerosci.2014.02.001.

[83] Tutorials Point, *Analyzing Signals in Communication*, 2025. [Online]. Available: https://www.tutorialspoint.com/principles_of_communication/principles_of_communication_analyzing_signals.htm.

[84] K. E. Kroemer Elbert, H. B. Kroemer, and A. D. Kroemer Hoffman, *Ergonomics: Chapter 5 - Human Senses*, 3rd. Academic Press, 2018, pp. 171–252. DOI: 10.1016/B978-0-12-813296-8.00005-0.

[85] G. J. Leishman, *Introduction to Aerospace Flight Vehicles*. Embry-Riddle Aeronautical University, 2022, pp. 2197–2260. DOI: 10.15394/eaglepub.2022.1066.

[86] A. Wykes, *What is the proximity effect, and why does it occur?* Jul. 2021. [Online]. Available: https://www.soundguys.com/proximity-effect-explained-51333/.

[87] B. Von Den Hoff, D. Simons, and M. Snellen, "Breakdown of propeller aircraft noise by applying conventional beamforming jointly with imaging using the rotating source identifier," Jun. 2022.

[88] D. G. Simons and M. Snellen, "Digital Signal Processing - an introduction," Feb. 2024.

A

Background Information

A.1. Fundamentals of Aircraft Noise

In aerospace applications, sound is considered noise when it is unwanted by the observer. Aircraft noise can be distinguished into two types of noise. Interior noise affects the passengers, whereas exterior noise affects the observers on the ground. This appendix will discuss the fundamentals of exterior aircraft noise, including the basics of acoustics, the main propagation effects, and standard noise metrics used in the aerospace industry.

A.1.1. The Basics of Acoustics

From a physical standpoint, sound is a propagating pressure disturbance. These disturbances are pressure variations relative to the ambient static pressure and are denoted as p'. The sound pressure in Pascals of a harmonic (=radiating at a single frequency) sound wave from a point source can be described by Equation A.1. In this equation, the distance from the point source in meters is denoted by the radius, r, t is the time in seconds, ω is the angular frequency in [rad/s], c is the speed of sound in [m/s], and A is the amplitude of the wave at 1 meter from the source [80].

$$p'(r,t) = \frac{A}{r}\cos[\omega(t - r/c)] \tag{A.1}$$

The wavelength, λ, is defined as the distance at which the wave has travelled one period, T, and can be calculated using Equation A.2. In this equation, c is equal to the propagation speed in [m/s]. This propagation speed is also referred to as the speed of sound, as given by Equation A.4, with the specific heat of air, $\gamma = 1.4$, and the specific gas constant, $R = 287$ [J/kg·K]. At room temperature (20 [°C] or 293.15 [K]), the speed of sound in air is equal to $c = 353$ [m/s]. The frequency of a sound wave, f, is related to the period according to Equation A.3. The characteristics of a sound wave are visualised in Figure A.1.

$$\lambda = c \cdot T \tag{A.2}$$

$$f = \frac{1}{T} \tag{A.3}$$

$$c = \sqrt{\gamma \cdot R \cdot T} \tag{A.4}$$

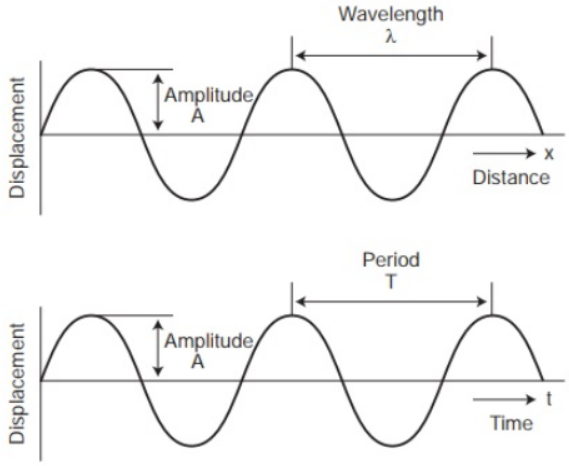

Figure A.1: The Characteristics of a Sound Wave [81]

The strength of a sound wave can be described by the effective sound pressure, p_e. The effective sound pressure represents the root-mean-square (RMS) of the acoustic pressure fluctuations over a period of time, T [80]. Note that in Equation A.5, T is a sufficiently long integration time and not the period of a harmonic wave.

$$p_e = \left[\frac{1}{T}\int_0^T \left[p'(t)\right]^2 dt\right]^{1/2} \tag{A.5}$$

To interpret and compare effective sound pressure, it is often expressed on a logarithmic scale. The result of this conversion is called the Sound Pressure Level (SPL), expressed in decibels [dB]. The SPL is defined in Equation A.6. In this equation, p_0 is the reference sound pressure that corresponds to the minimum threshold of hearing for humans and equals $p_{e0} = 2 \cdot 10^{-5}$ [Pa] [80]. Similarly, the sound can also be defined in terms of Power Watt Level (PWL), Equation A.7. In this equation, W is the acoustic power of a source in watts. This is the quantity of sound energy that is emitted per unit of time. The reference acoustic power, W_0, is generally equal to $W_0 = 10^{-12}$ [W] [80].

$$\text{SPL} = 10\log\left(\frac{p_e^2}{p_{e0}^2}\right) \tag{A.6}$$

$$\text{PWL} = 10\log\left(\frac{W}{W_0}\right) \tag{A.7}$$

To better understand effective sound pressure and sound pressure level, Table A.1 presents typical p_e and SPL values for various acoustic sources. After Table A.1, a short discussion about the decibel will follow.

Table A.1: Typical Effective Sound Pressures and their corresponding Sound Pressure Level for Various Acoustic Sources [80]

P_e in [N/m^2]	SPL in [dB]	Acoustic Source
2000	160	Threshold of pain
200	140	Jet aircraft
20	120	Chipping hammer
2	100	Heavy truck
0.2	80	Automobile
0.02	60	Normal conversation
2×10^{-3}	40	Library
2×10^{-4}	20	Whisper
2×10^{-5}	0	Threshold of hearing

What Are Decibels?

A decibel is a logarithmic measure to indicate sound intensity. It is defined as the ratio of a measured sound pressure to a standard reference pressure. As previously noted, this standard reference pressure is usually 20 [μPa], which aligns with the limit of human hearing. Due to this definition, a sound pressure level of 0 [dB] does *not* indicate the absence of sound. It only denotes that the sound pressure matches the reference level. Therefore, even negative decibel values are possible and indicate sounds quieter than this reference value.

Due to the logarithmic scale, decibels do not add arithmetically. For example, two noise events of 35 [dB] do *not* add up to 70 [dB]. Instead, the combined level is:

$$10\log\left(10^{35/10} + 10^{35/10}\right) \approx 38 \text{ dB}$$

This shows that doubling the sound source increases the total level by only about 3 [dB] [82]. Furthermore, if one sound source is 10 [dB] (or more) quieter than another (e.g., 70 [dB] vs. 80 [dB]), its contribution to the total level is considered negligible:

$$10\log\left(10^{80/10} + 10^{70/10}\right) \approx 80.4 \text{ dB}$$

This statement holds because a 1 [dB] change in SPL is just barely perceptible to the average human ear. Therefore, specifying results with a precision better than 1 [dB] is considered not meaningful in most applications.

Finally, although a 3 [dB] increase corresponds to a doubling of the sound power, the human ear perceives a 10 [dB] increase as roughly twice as loud.

Finally, acoustic data can be investigated in either the time domain or the frequency domain. Time-domain representations show how sound pressure evolves over time. This makes the time domain useful for identifying the timing and duration of noise events. In contrast, the frequency domain describes the same signal in terms of its frequencies. The frequency domain representation reveals which frequencies are present and how strong they are. A visual comparison of the two representations is provided in Figure A.2.

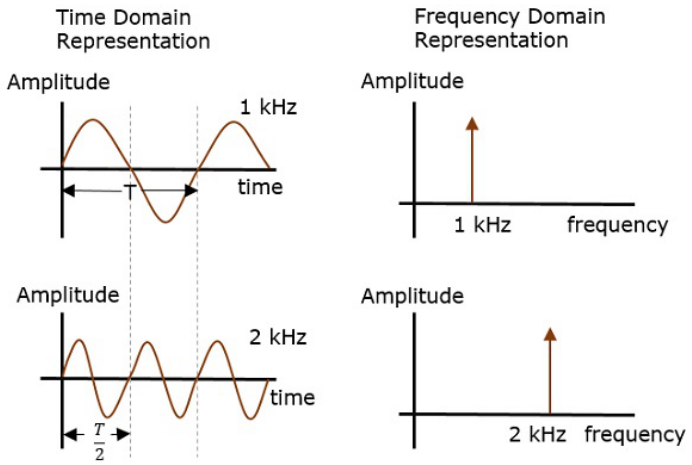

Figure A.2: Visual Representation of the Time Domain and Frequency Domain [83]

A.1.2. Noise Metrics in Aviation

While the sound pressure level (SPL) is useful for short-duration assessment, it does not capture the duration, frequency content, repetition, or human perception of annoyance over time. To evaluate aircraft noise in real-world contexts, several other noise metrics are used.

Overall A-Weighted Sounds Pressure Level - OASPL or L_A

The overall A-weighted sound pressure level, L_A, is a measure of sound that aligns more closely with how humans perceive loudness. Since the human ear is most sensitive to frequencies ranging from roughly 1 [kHz] and 5 [kHz], and is less sensitive at very low and very high frequencies [84], SPL measurements do not directly correspond to perceived loudness. A-weighting corrects for this by applying a frequency-dependent filter that attenuates SPL at frequencies beyond human hearing.

This correction is based on the so-called A-weighting curve. It approximates the human hearing sensitivity at a moderate loudness level of 40 phon. The phon is a unit of perceived loudness level. A sound is considered to have a loudness level of X phons if a group of listeners considers it to be equally loud as a tone that has a sound pressure level of X [dB] at a reference frequency of 1 [kHz] [84]. In other words, at 1 [kHz], the phon and the dB SPL values are identical. However, at frequencies other than 1 [kHz], the SPL must be adjusted to compensate for the ear's non-uniform sensitivity across the frequency spectrum. For example, as shown in Figure A.3, a sound at 100 [Hz] must have an SPL of 60 [dB] to be perceived as equally loud as a 40 [dB] SPL sound at 1000 [Hz], which corresponds to 40 phons. This demonstrates that lower-frequency sounds must be more intense to be perceived at the same loudness level as mid-frequency sounds.

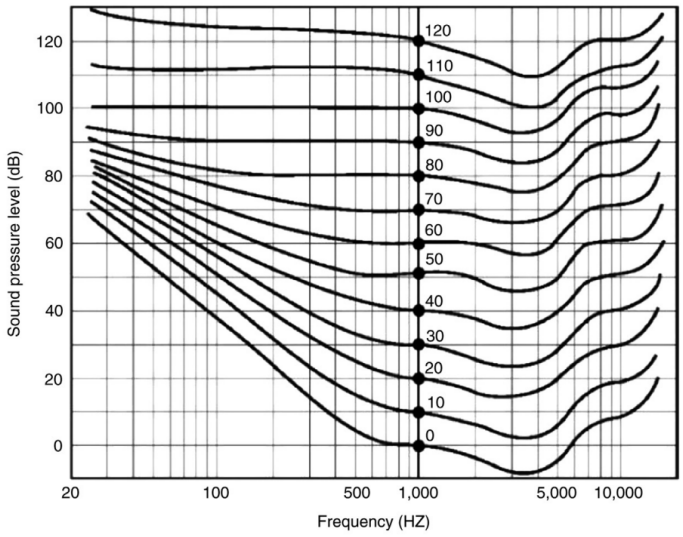

Figure A.3: Equal Loudness Contours in terms of Frequency and Sound Pressure Level where the Phon Level is indicated by a Dot at 1000 [Hz] [84]

The overall A-weighted sound pressure level can be computed by analysing the noise spectrum in frequency bands, typically 1/3-octave bands. Each band's SPL is adjusted by an A-weighting correction factor, ΔL_A. The A-weighted function is provided in Equation A.8.

$$\Delta L_{\mathrm{A}} = -145.528 + 98.262 \log f - 19.509 (\log f)^2 + 0.975 (\log f)^3 \tag{A.8}$$

The corrected values are summed logarithmically to obtain the overall A-weighted sound pressure level (in dBA, where the 'A' indicates that the value is A-weighted), Equation A.9. In Equation A.9, SPL(i) denotes the sound pressure level in the i-th frequency band. $\Delta L_A(i)$ is the A-weighting function at the corresponding centre frequency.

$$L_{\mathrm{A}} = 10 \log \sum_{i} 10^{\frac{\mathrm{SPL}(i)+\Delta L_{\mathrm{A}}(i)}{10}} \tag{A.9}$$

What Is A Frequency Band?

In acoustics, the frequency spectrum can be divided into so-called bands. A frequency band is a range of frequencies bounded by a lower and upper frequency limit, f_L and f_U, respectively. An octave band is a frequency range where the upper frequency is double the lower frequency [80]. For example, an octave band might range from 100 [Hz] to 200 [Hz]. The centre frequency, f_n is equal to the geometric mean of f_L and f_U (i.e. $f_n = \sqrt{f_U \cdot f_L}$). In this case, the centre frequency would be equal to $f_N = \sqrt{100 \cdot 200} \approx 141$ [Hz].

A more refined way to analyse sound frequencies than the octave band is to use 1/3-octave bands. This is a division of the frequency spectrum into bands where each band's upper frequency limit is $2^{1/3}$ times its lower frequency limit ($f_U = 2^{1/3} \cdot f_L$). Therefore, the centre frequency (being the geometric mean of f_L and f_U) can be calculated using Equation A.10.

$$f_N = \sqrt{f_U \cdot f_L} = \sqrt{2^{1/3} \cdot f_L \cdot f_L} = 2^{1/6} \cdot f_L \tag{A.10}$$

Equivalent A-Weighted Sound Pressure Level - $L_{Aeq,T}$

Although the A-weighted sound pressure level accounts for differences in frequency perception, it remains a noise metric for stationary noise signals only. However, the human ear is also sensitive to the duration of a noise event. One event can be more annoying than another, even though they have the same overall A-weighted sound pressure level, due to the different durations of the events. The equivalent A-weighted sound level (EAL) integrates the instantaneous overall A-weighted sound pressure level, $L_A(t)$, over time [80]. The equivalent A-weighted sound level can be calculated with Equation A.11.

$$L_{\mathrm{A\,eq\,,T}} = 10 \log \left[\frac{1}{T} \int_0^T 10^{\frac{L_{\mathrm{A}}(t)}{10}} dt \right] \tag{A.11}$$

In Equation A.11, the integration time, T, is selected to encompass the period where $L_A(t)$ is at least 10 [dBA] lower than the peak overall A-weighted sound pressure level, $L_{A,max}$. This integration time, T, is often called the '10 [dBA] down time'.

Sound Exposure Level - SEL or L_{AE}

Another important metric is the Sound Exposure Level (SEL), given in Equation A.12. Similarly to the equivalent A-weighted sound pressure level, $L_A(t)$ is integrated over the event duration, T. This time, however, it is normalised to one second, T_1 [82]. This allows for comparing events with different durations.

$$L_{\mathrm{AE}} = 10 \log \left[\frac{1}{T_1} \int_0^T 10^{\frac{L_{\mathrm{A}}(t)}{10}} dt \right] \tag{A.12}$$

In Figure A.4, the previously discussed instantaneous overall A-weighted sound pressure level $L_A(t)$ is plotted as a function of time. Furthermore, the maximum overall A-weighted sound pressure level, $L_{A,max}$, and the equivalent A-weighted sound level, $L_{Aeq,T}$ (dashed line), are indicated. Finally, Figure A.4 includes the sound exposure level L_{AE} (shaded area).

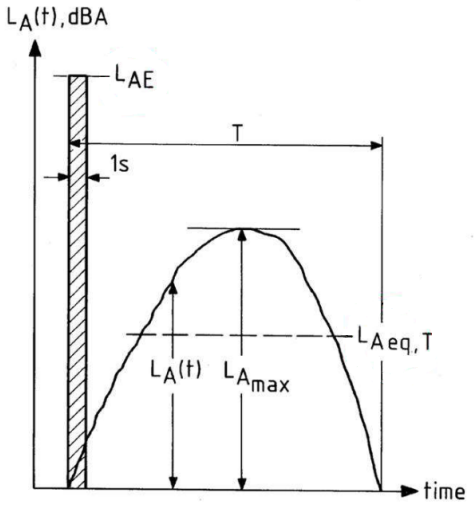

Figure A.4: Typical Noise Event from an Aircraft Flyover [80]

Day-Evening-Night Average Level - L_{DEN}

For long-term exposure assessments, the Day-Evening-Night Average Level, L_{DEN}, is used [82]. This A-weighted measure averages the sound levels over 24 hours (86400 seconds). The function applies penalties for noise occurring during evening and nighttime hours. This reflects the increased annoyance experienced during those times. The equation for the Day-Evening-Night Average Level is provided in Equation A.13. In this equation, SEL_i is the SEL value of the i^{th} noise event. W_i is the corresponding penalty in decibels. Usually, this penalty is 0 [dB], 5 [dB], or 10 [dB] for events during the day, in the evening, and at night, respectively. Finally, N is the amount of noise events in the 24-hour period.

$$L_{\text{DEN}} = -49.4 + 10\log\left[\sum_{i=1}^{N} 10^{(\text{SEL}_i + W_i)/10}\right] \tag{A.13}$$

A.1.3. Propagation Effects

The noise metrics described above provide estimates of noise generated at a source, independent of propagation effects. However, after being generated, sound undergoes several effects that modify its characteristics before reaching the receiver. Below, a short discussion of some propagation effects will be provided.

Spherical Spreading

First, let us assume that the atmosphere is homogeneous. This means the temperature is constant, there is no wind, and there are no boundaries. In such an environment, a point source does not radiate sound in a single direction. Instead, it emits the sound waves equally in all directions. This results in a spherical wavefront. Each point at a distance r from the source lies on an expanding sphere. The larger the distance, the bigger the area over which the sound is spread [85]. The result is a decrease in sound intensity (and therefore in sound pressure level) with increasing distance from the source. The concept of spherical spreading is visualised in Figure A.5.

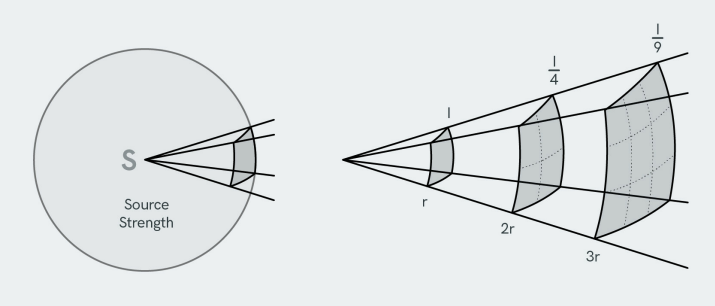

Figure A.5: Visualisation of Spherical Spreading [86]

The sound pressure level (SPL) can be calculated using Equation A.14. In this equation, PWL is the Power Watt Level in decibels. For a directional sound source, the SPL can be calculated using Equation A.15. In this equation, DI is the directivity index.

$$\text{SPL(r)} = \text{PWL} - 10.8 - 20\log(r) \tag{A.14}$$

$$\text{SPL(r}, \theta) = \text{PWL} - 10.8 - 20\log(r) + \text{DI}(\theta) \tag{A.15}$$

Atmospheric Sound Absorption

Sound waves travelling through the atmosphere are attenuated by absorption. Sound absorption occurs due to viscous friction in the air and molecular relaxation. This reduces the sound level received at a distance. Absorption is quantified by the absorption coefficient, α, expressed in decibels per meter [dB/m] or decibels per kilometre [dB/km]. This coefficient depends on the sound frequency, as well as on the relative humidity and the temperature. The absorption coefficient for several temperatures and relative humidities can be found in Table A.2. Note that the coefficient is given in [dB/km]. As can be concluded from Table A.2, higher frequencies are much more susceptible to absorption than low frequencies. The reduction in sound pressure level due to absorption increases linearly with distance [6]. Therefore, the sound pressure level can now be calculated using Equation A.16. At long distances or at high altitudes, losses due to atmospheric absorption can become significant. For example, in cruise conditions, even moderate-frequency noise can be attenuated by a noticeable amount before reaching the ground.

Table A.2: Absorption Coefficients, α, in [dB/km] at different Atmospheric Conditions (at the Octave Band Centre Frequencies) [80]

Temperature (°C)	Relative humidity (%)	63 Hz	125 Hz	250 Hz	500 Hz	1000 Hz	2000 Hz	4000 Hz	8000 Hz
30	20	0.212	0.717	1.86	3.40	6.00	14.6	47.6	167
	50	0.0904	0.346	1.24	3.56	7.03	11.7	24.7	74.2
	80	0.0573	0.223	0.852	2.59	7.41	13.3	56.4	219
20	20	0.259	0.706	1.39	2.59	6.55	21.6	74.9	218
	50	0.122	0.440	1.31	2.73	4.67	9.90	27.0	96.2
	80	0.0788	0.298	1.04	2.76	5.15	9.21	18.1	69.6
10	20	0.271	0.576	1.19	1.91	4.43	11.3	52.3	201
	50	0.160	0.481	1.05	1.89	4.27	13.3	47.2	157
	80	0.103	0.373	1.13	1.89	3.57	8.32	39.1	100
0	20	0.256	0.609	1.84	6.18	25.7	34.8	47.2	58.4
	50	0.180	0.408	0.818	2.61	8.68	24.9	41.8	74.0
	80	0.138	0.376	0.756	1.51	4.07	13.9	49.3	148

$$\text{SPL}(r, \theta) = \text{PWL} - 10.8 - 20\log(r) + \text{DI}(\theta) - \alpha r \tag{A.16}$$

Doppler Effect
Finally, when a sound source moves relative to an observer, the observer's perceived frequency differs from the source's actual frequency. This phenomenon is commonly referred to as the Doppler effect. For a moving source with a stationary observer, the Doppler frequency shift can be calculated using Equation A.17 [6].

$$f_o = \frac{f_s}{1 - M_x \cos\theta} \tag{A.17}$$

In Equation A.17, f_o and f_s denote the observed frequency and source frequency, respectively. The Doppler shift depends on the aircraft's speed (expressed as a Mach number, $M = \frac{V}{c}$, with V being the velocity of the aircraft in [m/s] and c being the speed of sound in [m/s]) and the angle between the flight path and the observer's line of sight, θ. From Equation A.17, it can be concluded that as the aircraft approaches ($\theta < 90°$), the sound waves are compressed. This leads to a higher perceived frequency. On the other hand, as the aircraft moves away ($\theta > 90°$), the sound waves are stretched out. This results in a lower perceived frequency. The Doppler effect is visualised in Figure A.6. In practical terms, the Doppler effect results in the same propeller tone sounding higher-pitched during the approach phase and lower-pitched during departure.

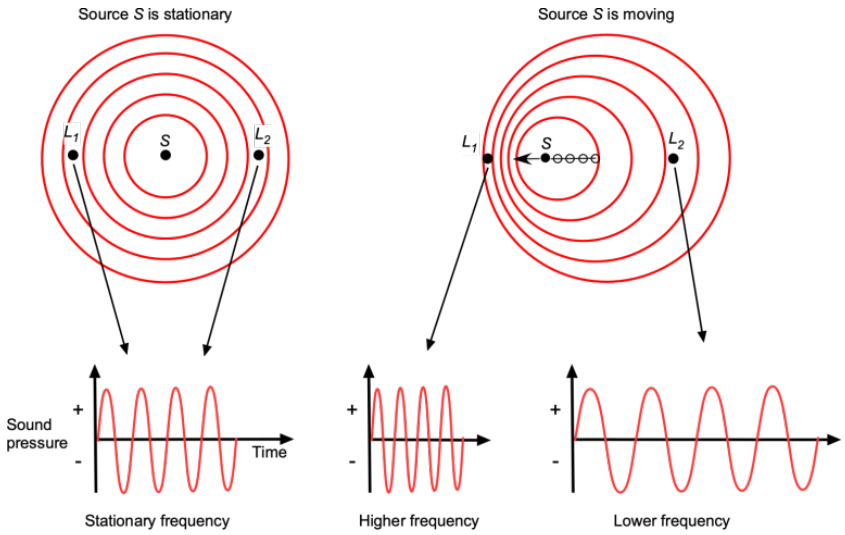

Figure A.6: The Change in Perceived Frequency due to the Doppler Effect [85]

A.1.4. Types of Aerodynamic Noise

Propellers generate complex acoustic signatures consisting of both periodic and random components. These two types of aerodynamic noise are often referred to as tonal and broadband noise. As this thesis focuses on (modelling) the broadband component of noise, more information on this type of aerodynamic noise is provided in chapter 2. A brief description of tonal noise is provided below.

Tonal Noise
Tonal noise, also referred to as harmonic or periodic noise, arises from sources that repeat at a constant rate. This repetition is typically synchronised with the rotation of the propeller blades. The propeller blades generate acoustic pressure fluctuations that produce peaks in the frequency domain spectrum at harmonics of the blade passage frequency (BPF). The BPF itself is defined by Equation A.18. In Equation A.18, N is the number of blades and RPM is the rotational speed of the propeller. Because the pressure pulse generated by each passing blade is typically not a pure sinusoid, the resulting signal contains not only the fundamental frequency but also multiple harmonics [6]. These harmonics appear at integer multiples of the BPF and are visible as discrete spectral peaks in the frequency domain.

$$\text{BPF} = N \cdot \frac{\text{RPM}}{60} \tag{A.18}$$

The generation of tonal noise can be grouped into three categories: thickness noise, steady-loading noise, and unsteady-loading noise [87]. First, thickness noise arises from the periodic displacement of air by the rotating blade sections. Therefore, thickness noise depends primarily on blade geometry and rotational speed. This type of noise becomes increasingly significant at high speeds [6].

Steady-loading noise originates from the aerodynamic lift and drag forces acting on the blade as the propeller generates thrust and torque. These forces produce fluctuating pressure fields that generate sound as they rotate with the blade [14]. Steady-loading noise is typically dominant at low and up to moderate speeds.

In addition to steady-loading noise, tonal noise also includes periodic unsteady-loading effects. These effects arise when the flow approaching the propeller is non-uniform [18]. The disturbances in the inflow remain fixed in space while the blades rotate through them. As a result, each blade encounters these flow disturbances at the same point during every revolution. An example of this is a propeller that operates at an angle of attack. In this scenario, the blade's angle changes cyclically with respect to the incoming flow. This leads to periodic pressure fluctuations that generate sound at the blade-passage frequency and its harmonics [14]. The combined effect of thickness noise, steady-loading noise, and unsteady-loading noise results in a sound field characterised by a harmonic structure as can be seen in Figure A.7.

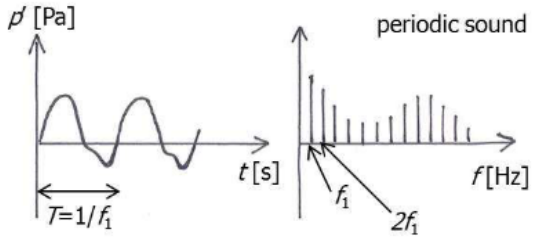

Figure A.7: Tonal Noise at the Blade Passing Frequency (BPF) and its Multiples in Time Domain (Left) and Frequency Domain (Right) [80]

A.2. Digital Signal Processing

In most physical observations, signals act as continuous functions. This means that they vary smoothly over time or space. However, digital signal processing (DSP) operates on discrete signals. Discrete signals are derived by sampling the continuous signals at regular intervals, Δt. The continuous signal is denoted $x(t)$, and the discrete systems are often denoted as x_k [88].

The process of signal processing involves transforming these signal sequences through a system. The system can be thought of as a mathematical operator that converts input signals, $x(t)$ or x_k, into output signals, $y(t)$ or y_k (see Figure A.8). The systems that process these signals can be classified according to properties such as linearity, time invariance, and causality. A system is considered linear if the superposition principle holds. This means that the output generated from a weighted sum of inputs corresponds directly to a weighted sum of the outputs. A system is considered invariant if applying a time shift to the input produces a matching shift in the output. Causal systems only respond to present and past input values, $x(t)$ for $t \leq t_0$.

Figure A.8: System with Input Signals, $x(t)$ or x_k, and Output Signals, $y(t)$ or y_k [88]

A.2.1. Impulse Response Method

For a linear time-invariant one-dimensional system, the system's output when the input is a Dirac delta function (in continuous time) or a Kronecker delta (in discrete time) (see Figure A.9) is named the impulse response. The impulse response of a system is denoted as h_k or $g(t)$ for the discrete and continuous situations, respectively. By knowing the impulse response of a system, one can determine the output for any other arbitrary input through convolution with this impulse response [88]. This makes the impulse response method a valuable tool in digital signal processing, as it provides a complete characterisation of linear time-invariant systems.

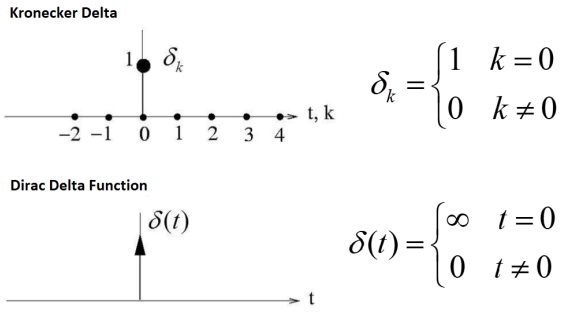

Figure A.9: Input Signal for a Discrete System (Kronecker Delta) and for a Continuous System (Dirac Delta) (adapted from [88])

A.2.2. Fourier Transform – Continuous and Discrete

Up until this point, signal processing has been described in the time domain. However, as described in subsection A.1.2, important insights can be found when the same signal is represented in the frequency domain. The Fourier transform enables the transition between the time and frequency domains [6].

Consider a continuous-time signal, $x(t)$, e.g. the acoustic pressure $p'(t)$ as recorded by a microphone. The continuous Fourier Transform (FT) of this signal is given by Equation A.19. On the other hand, the continuous Inverse Fourier Transform (IFT), Equation A.20, reconstructs the time-domain signal from its frequency components [88].

$$X(f) = \int_{-\infty}^{\infty} x(t) e^{-2\pi i f t} dt \tag{A.19}$$

$$x(t) = \int_{-\infty}^{\infty} X(f) e^{2\pi i f t} df \tag{A.20}$$

For example, a pure tone at frequency f_0 described by $x(t) = \cos(2\pi f_0 t)$ results in a Fourier transform as provided in Equation A.21. The Fourier transform consists of two Dirac delta peaks: one at $f = f_0$ and one at $f = -f_0$. Therefore, the Fourier transform is called two-sided. A complex exponential signal, on the other hand, yields a single peak at the corresponding frequency. Therefore, the Fourier transform of a complex harmonic signal is one-sided.

$$X(f) = \frac{1}{2}\delta\left(f + f_0\right) + \frac{1}{2}\delta\left(f - f_0\right) \tag{A.21}$$

For discrete signals (i.e. a continuous signal sampled at N discrete times), the equivalent transformation is the Discrete Fourier Transform (DFT), Equation A.22. In this equation, Δt is the sample distance, $\Delta t = \frac{1}{f_s}$, with f_s the sample frequency in Hertz. The Inverse Discrete Fourier Transform (IDFT) is provided in Equation A.23.

$$X_m = \Delta t \sum_{k=0}^{N-1} x_k e^{-2\pi i k m / N} \tag{A.22}$$

$$x_k = \frac{1}{N\Delta t} \sum_{m=0}^{N-1} X_m e^{2\pi i k m/N} \tag{A.23}$$

An advantage of this approach is that it simplifies system operations such as filtering. As mentioned before, in the time domain, the output of a linear invariant system is computed via convolution with the system's impulse response. However, in the frequency domain, this convolution becomes a simple multiplication. If a signal, x_k, has a frequency representation, $X(f)$, and the system has a transmission function (filter), $H(f)$, then the output, $Y(f)$, can be determined with Equation A.24. This direct relationship makes it intuitive to design and analyse filters in the frequency domain.

$$Y(f) = H(f) \cdot X(f) \tag{A.24}$$

A.2.3. Windowing and the Hann Function

When analysing a flyover recording, often only a short part of the signal is used to examine the noise at a specific aircraft position. These short segments (often around 0.1 seconds long) form a small window of the full time signal. Because the window abruptly cuts off the signal, the values at the start and end of the segment are usually nonzero. This sudden jump at the edges introduces a discontinuity.

When the Fourier transform is applied, this discontinuity produces a sinc-shaped pattern in the frequency domain instead of clean peaks at the relevant frequencies. The sidelobes of the sinc function spread energy into neighbouring frequencies, an effect known as spectral leakage. As shown in Figure A.10, these sidelobes can be large enough to distort weaker tonal components in the spectrum.

To reduce this problem, the time segment may be multiplied by a window function that gradually brings the signal to zero at both edges. This suppresses the sidelobes in the frequency domain. The Hann function, shown in Figure A.10, is a commonly used window function.

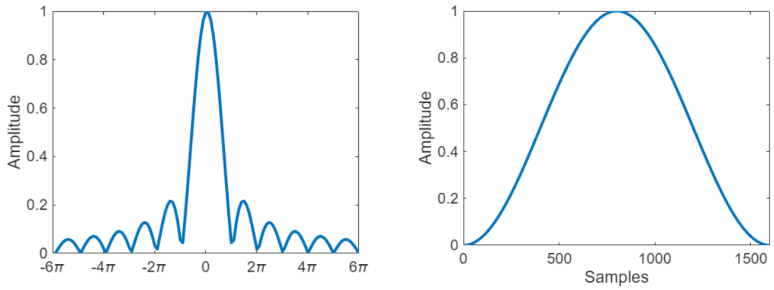

Figure A.10: Sinc Function (Left) and the Hann Function (Right)

A.2.4. Sampling

Finally, it should be noted that the highest frequency that can be accurately captured after sampling is known as the Nyquist frequency [88]. The Nyquist frequency equals half the sampling frequency, $f_s/2$. The sampling theorem states that to accurately reconstruct a signal, the sampling frequency, f_s, must be at least $f_s = 2B$, where B is the bandwidth of the continuous signal. This condition ensures that distinct frequency components are not aliased. Aliasing is the term for the misrepresentation of lower frequencies caused by undersampling.

However, real-world signals are rarely perfectly bandlimited. Most physical signals have spectra that decay gradually toward zero, rather than a sharp frequency cutoff at B. As a result, even if the sampling rate satisfies the Nyquist criterion, some spectral energy may still lie above $f_s/2$. This can cause unavoidable aliasing. To mitigate this, an anti-aliasing filter (AAF) can be applied to the analogue signal before sampling. The analogue low-pass filter suppresses frequency components above the Nyquist limit.

B

Noise Spectra for Take-Off Cases

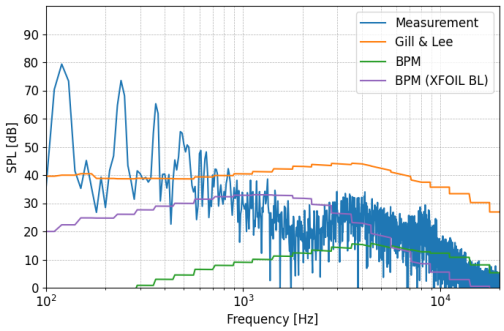

(a) TO1

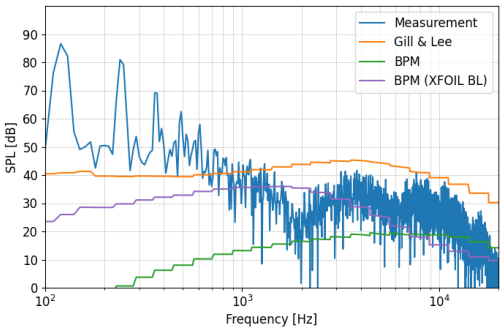

(b) TO2

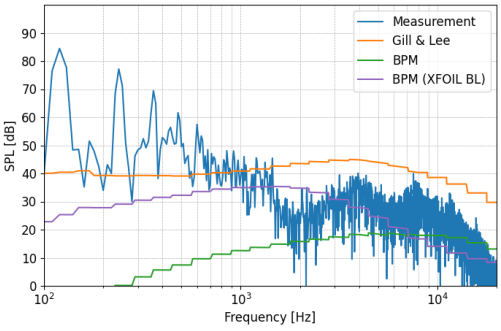

(c) TO3

Figure B.1: Comparison of Measured and Predicted Broadband Noise Spectra for the Three Take-Off Cases at the Overhead Position

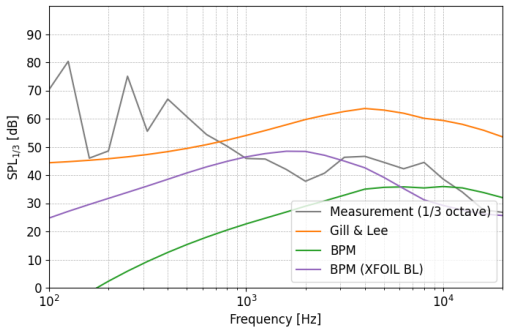

(a) TO1

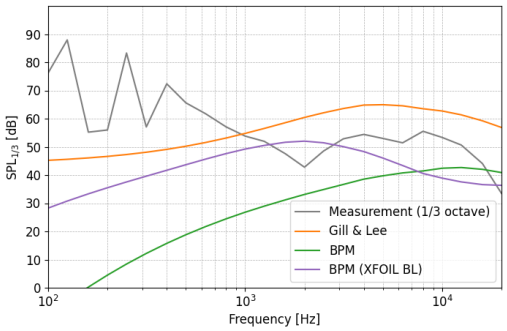

(b) TO2

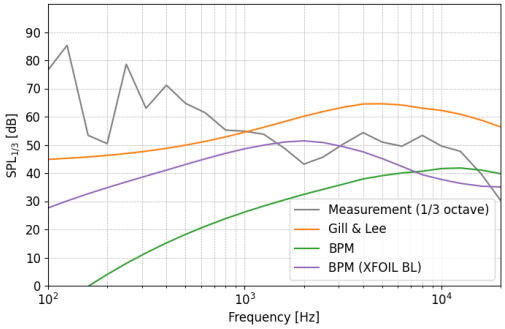

(c) TO3

Figure B.2: Comparison of Measured and Predicted Broadband Noise Spectra for the Three Take-Off Cases at the Overhead Position in the One-Third Octave Domain